Report on Modeling Coupled Processes in the Near Field of a Clay Repository

Fuel Cycle Research & Development

Prepared for

U.S. Department of Energy
Used Fuel Disposition

Hui-Hai Liu, Jim Houseworth,
Jonny Rutqvist, Lianchong Li,
Daisuke Asahina, Fei Chen,
Jens Birkholzer

Lawrence Berkeley National Laboratory

August 2012

FCRD-UFD-2012-000223

DISCLAIMER

This document was prepared as an account of work sponsored by the United States Government. While this document is believed to contain correct information, neither the United States Government nor any agency thereof, nor The Regents of the University of California, nor any of their employees, makes any warranty, express or implied, or assumes any legal responsibility for the accuracy, completeness, or usefulness of any information, apparatus, product, or process disclosed, or represents that its use would not infringe privately owned rights. Reference herein to any specific commercial product, process, or service by its trade name, trademark, manufacturer, or otherwise, does not necessarily constitute or imply its endorsement, recommendation, or favoring by the United States Government or any agency thereof, or The Regents of the University of California. The views and opinions of authors expressed herein do not necessarily state or reflect those of the United States Government or any agency thereof or The Regents of the University of California.

Ernest Orlando Lawrence Berkeley National Laboratory is an equal opportunity employer.

FCT Quality Assurance Program Document **Revision 1 08/19/2011**

Appendix E
FCT Document Cover Sheet

Name/Title of Deliverable/Milestone	Report on Modeling Coupled Processes in the Near Field of a Clay Repository
Work Package Title and Number	FT-12LB080706 Natural Systems Evaluations - LBNL
Work Package WBS Number	1.02.08.07
Responsible Work Package Manager	Hui-Hai Liu (Name/Signature)

Date Submitted 8-14-2012

Quality Rigor Level for Deliverable/Milestone ☒ QRL-3 ☐ QRL-2 ☐ QRL-1 ☐ N/A* ☐ Nuclear Data

This deliverable was prepared in accordance with Lawrence Berkeley National Laboratory
(Participant/National Laboratory Name)

QA program which meets the requirements of

☒ DOE Order 414.1 ☐ NQA-1-2000 ☐ Other

This Deliverable was subjected to:

☒ Technical Review ☐ Peer Review

Technical Review (TR)

Review Documentation Provided

☐ Signed TR Report or,

☐ Signed TR Concurrence Sheet or,

☒ Signature of TR Reviewer(s) below

Peer Review (PR)

Review Documentation Provided

☐ Signed PR Report or,

☐ Signed PR Concurrence Sheet or,

☐ Signature of PR Reviewer(s) below

Name and Signature of Reviewers

Liange Zheng

***NOTE** *In some cases there may be a milestone where an item is being fabricated, maintenance is being performed on a facility, or a document is being issued through a formal document control process where it specifically calls out a formal review of the document. In these cases, documentation (e.g., inspection report, maintenance request, work planning package documentation or the documented review of the issued document through the document control process) of the completion of the activity along with the Document Cover Sheet is sufficient to demonstrate achieving the milestone. QRL for such milestones may be also be marked N/A in the work package provided the work package clearly specifies the requirement to use the Document Cover Sheet and provide supporting documentation.*

This page is intentionally blank.

TABLE OF CONTENTS

Executive Summary x

1. Introduction 1

2. Implementation and Validation of the Constitutive Relationships 3
   - 2.1 A Brief Review of Previous Studies 3
   - 2.2 Implementation of Constitutive Relationships 5
   - 2.3 Comparison between Modeling Results and Field Data 19
   - 2.4 Investigation into EDZ Evolution with the Fine-Grid Model 30
   - 2.5 Discussion of Uncertainties 40
   - 2.6 Concluding Remarks 41

3. Development of a Discrete Fracture Network (DFN) Approach for Fractures in Argillaceous Rock 43
   - 3.1 Overview of Thermal-Hydrological-Mechanical (THM) Coupling and Fractures in Argillaceous Rock 43
   - 3.2 Discrete Fracture and Dual-Permeability Models for Hydrogeologic Processes 45
   - 3.3 Representing Discrete Fractures and Rock Matrix- Numerical Gridding Strategy 47
   - 3.4 Hydrogeologic Processes in Discrete Fractures 52
   - 3.5 Mechanical Damage Model using RBSN 70
   - 3.6 Hydro-Mechanical Model using TOUGH2 and RBSN 76
   - 3.7 Conclusions 83

4. THM Modeling of the FE Experiment at the Mont Terri Site 85
   - 4.1 FE Experiment at the Mont Terri Site 85
   - 4.2 Modeling approach 87
   - 4.3 FE Model Setup 89
   - 4.4 Base-Case TH Simulation 92
   - 4.5 Sensitivity Analysis 94
   - 4.6 THM Simulation 103
   - 4.7 Conclusions 106

5. Summary and Future Work 107

6. References 110

LIST OF FIGURES

Figure 1-1. Clay/shale-formation distribution in the USA (Gonzales and Johnson, 1984). 1

Figure 2-1. Sketch of the Mohr-Coulomb failure criterion employed in FLAC3D. 8

Figure 2-2. Computational scheme for the numerical implementation of the TPHM into FLAC3D. 13

Figure 2-3. Sketch of the definition of the degradation indices (Yuan and Harrison, 2005). 15

Figure 2-4. Schematic illustration of fracture aperture and permeability of a rock element due to brittle failure. 18

Figure 2-5. Vertical cross section of the Mont Terri anticline along the motorway tunnel (Bossart and Thury, 2008) 20

Figure 2-6. Layout of ED-B mine-by experiment instrumentation and tunnel system. 21

Figure 2-7. Layout of MB experiment Niche and the *in situ* excavating process (Vietor, 2011). 21

Figure 2-8. Stress–strain plots for a range of σ_3 values (0–20 MPa) (Olalla et al. 1999). 24

Figure 2-9. Variation in the degradation index for Opalinus Clay with confining stress. 25

Figure 2-10. Simulated stress–strain curve corresponding to the fracture process displayed in the following Figures 2-11 and 2-12. 27

Figure 2-11. Simulated fracture process of a rock specimen under uniaxial compression. 27

Figure 2-12. Simulated fracture process of a rock specimen subjected to a confining pressure of 10 MPa. 28

Figure 2-13. Location of key points for monitoring displacement variations around the tunnel. 29

Figure 2-14. Numerically obtained displacement mode based on TPHM. 29

Figure 2-15. Displacement variation (magnitude) at points around the tunnel. 30

Figure 2-16. Numerically obtained EDZ (plastic zone) evolution: (a) EDZ (left), and (b) minimum principal stress (right). 33

Figure 2-17 (continued). Numerically obtained EDZ (plastic zone) evolution: (a) EDZ (left), and (b) minimum principal stress (right). 34

Figure 2-18. Failure type in the EDZ (tension failure marked by RED color and shear failure marked by BLUE color). 35

Figure 2-19. Variation in hydraulic conductivity of the surrounding rock mass. 36

Figure 2-20. Distribution of hydraulic conductivity along the line A-A. 37

Figure 2-21. Conceptual model of the EDZ and EDZ fractures in the tunnel walls induced by stress redistributions; around New Gallery after excavation (Bossart et al., 2004). 38

Figure 2-22. Numerically obtained EDZ (plastic zone) evolution based on SPHM. 38

Figure 2-23(continued). Numerically obtained EDZ (plastic zone) evolution based on SPHM. 39

Figure 2-24(continued). Numerically obtained EDZ (plastic zone) evolution based on SPHM. 40

Figure 2-25. The final EDZ mode based on (a) TPHM and (b) SPHM, respectively. 40

Figure 3-1. Model representations of a two-dimensional fracture-matrix system. (a) discrete fracture model; (b) dual continuum model. 46

Figure 3-2. Solute mass arrival rates from discrete-fracture and dual-permeability models. 47

Figure 3-3. Selection of Delaunay tessellation: (a) a node within a triangle circumcircle (not accepted); and (b) no node within a triangle circumphere (accepted). 48

Figure 3-4. Mesh construction sequence: (a) nodal point set; (b) Delaunay tessellation; and (c) Voronoi diagram. 48

Figure 3-5. Mapping of a fracture geometry on top an irregular Voronoi grid. 50

Figure 3-6. Fracture interface with the representation of DFN in 3D Voronoi grid: (a) irregular fractures, and (b) straight fractures. 50

Figure 3-7. Bedding planes and fractures of EDZ in 2D representations: (a) conceptual model after Bossart et al., (2004); (b) DFN in Voronoi grid; and (c) enlarged view. 51

Figure 3-8. Node and connection in the TOUGH2 simulator: (a) ordinary matrix nodes and connections; (b) new fracture nodes and connections; and (c) effect of vertex node on flow pattern. 52

Figure 3-9. Transport results from single-fracture analytical model for flow parallel to the fracture. Contour plot of concentrations at 357 days. 59

Figure 3-10. Transport results from single-fracture analytical model for flow parallel to fracture; arrivals 10 m downstream of the source release point, normalized by mass released. (a) cumulative mass arrivals in fracture and matrix; (b) mass-arrival rates in fracture and matrix. 59

Figure 3-11. Transport results from single-fracture analytical model for matrix flow at an oblique angle to the fracture. Contour plot of concentrations at 357 days. 60

Figure 3-12. Transport results from single-fracture analytical model for matrix flow at an oblique angle to the fracture; arrivals 10 m downstream of the source release point, normalized by mass released (a) cumulative mass arrivals in fracture and matrix; (b) mass-arrival rates in fracture and matrix. 60

Figure 3-13. Transport results from single-fracture analytical model for matrix flow at an 45 degree angle to the fracture. Contour plot of concentrations at 357 days. 61

Figure 3-14. Transport results from single-fracture analytical model for matrix flow at a 45-degree angle to the fracture; arrivals 10 m downstream of the source release point, normalized by mass released (a) cumulative mass arrivals in fracture and matrix; (b) mass-arrival rates in fracture and matrix. 62

Figure 3-15. Solute concentration profiles at 1042 days for parallel flow case: (a) fracture concentration profile; (b) matrix concentration profile about 2 cm from fracture. 65

Figure 3-16. Solute concentration profiles at 1042 days for cross-flow case: (a) fracture concentration profile; (b) matrix concentration profile about 2 cm from fracture. 65

Figure 3-17. Cumulative mass arrival 4 m from release point: (a) parallel flow base case; (b) cross-flow base case. 66

Figure 3-18. Voronoi grid with irregular fracture. 66

Figure 3-19. Comparison of mass cumulative mass arrivals at a fracture-path distance of 4 m from the source for a straight fracture (analytical) and for four irregular fracture cases (1065, 2127, 4567, and 8081 nodes). 67

Figure 3-20. Conceptual diagrams for transport in a fracture-matrix system for a straight fracture and an irregular fracture. 68

Figure 3-21. Comparison of cumulative mass arrival scaling for different fracture lengths: (a) matrix flow parallel to fracture; (b) matrix flow at an oblique angle to fracture. 69

Figure 3-22. Typical lattice element *ij*: (a) within a Voronoi grid; (b) isolated from the network; and (c) a zero-size spring set (referenced to local coordinate axes *n*-*s*-*t*) located at centroid *C* of Voronoi cell boundary area A_{ij}. 72

Figure 3-23. Stress tensor at Voronoi cell node: (a) components of spring force local coordinates; (b) a set of forces obtained by equilibrium; and (c) complete stress tensor at Voronoi cell node. Adapted from Yip et al. (2005). 72

Figure 3-24. Tensoral stress calculation under uniaxial compressive loading: (a) Voronoi discretization of a cubic domain; (b) Mohr's circle representation of stress state at Voronoi cell nodes. 74

Figure 3-25. Mohr-Coulomb surface with tension cut-off. 76

Figure 3-26. Time evolution of compressive stress and saturation at point P1 for simple swelling model. 77

Figure 3-27. (a) Computational grid used for the TOUGH-RBSN simulator; and (b) simulation results of radial and tangential stresses for $\theta = 0$ and 2π, respectively, versus the distance from the center of the domain. 79

Figure 3-28. 2D Voronoi grid of slab structure (297 nodes) drying from top surface: (a) undeformed configuration; (b) deformed shape with the first boundary conditions; and (c) fracture pattern with the second boundary conditions. 80

Figure 3-29. Fracture pattern with fine mesh (2680 nodes). 80

Figure 3-30. Fracture pattern with various thicknesses: (a) 20mm; (b) 40mm; and (c) 80mm. 81

Figure 3-31. Evolution of shrinkage cracking in plan view (4802 nodes): (a) initial configuration; (b) early stage; (c) intermediate stage; and (d) late stage. 82

Figure 3-32. Drying surface of clay-rich geomaterial during dry seasons. 83

Figure 3-33. 3D view of fracture pattern with various thicknesses: (a) 20mm; and (b) 40mm. 83

Figure 4-1. Summary schematic of the Mont Terri URL with side galleries and drifts for testing. Three specific experiments of relevance to UFDC are highlighted (based on Garitte, 2010). 85

Figure 4-2. Plan view of experiment setup and borehole layout (from Garitte, 2010). 86

Figure 4-3. Side view of experiment setup and borehole layout (from Garitte, 2010). 86

Figure 4-4. FE experiment time frame. Phases 16 to 20 refer to Mont Terri project phases (Vietor, 2012). 87

Figure 4-5. View of FE tunnel face from the FE niche showing beddings dipping 45° (Vietor, 2012). 89

Figure 4-6. TOUGH-FLAC numerical grids for model inception. 90

Figure 4-7. Capillary curves for bentonite and Opalinus clays. 92

Figure 4-8. Simulated evolution of TH processes in the buffer and host rock: (a) temperature, (b) liquid saturation, (c) fluid pressure. 93

Figure 4-9. Capillary curves for bentonite in sensitivity analysis. 94

Figure 4-10. Simulated effect of capillary pressure curves on pore pressure evolution in: (a) 0.55, (b)1.18, (c)1.64, and (d) 21.9 m. 95

Figure 4-11. Simulated effect of capillary pressure curves on water saturation evolution in: (a) 0.55, (b)1.18, (c)1.64, and (d)21.9m. 96

Figure 4-12. Simulated effects of capillary pressure curves on temperature evolution in: (a) 0.55, (b) 1.18, (c) 1.64, and (d) 21.9 m. 97

Figure 4-13. Simulated effects of concrete permeability on the pore pressure evolution in: (a) 0.55, (b) 1.18, (c) 1.64, and (d) 21.9 m. 98

Figure 4-14. Simulated effects of concrete permeability on the water saturation evolution in: (a) 0.55, (b) 1.18, (c) 1.64, and (d) 21.9 m. 99

Figure 4-15. Simulated effects of concrete permeability on the temperature evolution in: (a) 0.55, (b) 1.18, (c) 1.64, and (d) 21.9 m. 100

Figure 4-16. Simulated effects of EDZ on the pressure evolution in: (a) 0.55, (b) 1.18, (c) 1.64, and (d) 21.9 m. 101

Figure 4-17. Simulated effects of EDZ on the water saturation evolution in: (a) 0.55, (b) 1.18, (c) 1.64, and (d) 21.9 m. 102

Figure 4-18. Simulated effects of EDZ on the temperature evolution in: (a) 0.55, (b) 1.18, (c) 1.64, and (d) 21.9 m. 103

Figure 4-19. Simulated stress evolution within the bentonite buffer. 105

Figure 4-20. Simulated stress evolution within the Opalinus clay. 105

LIST OF TABLES

Table 2-1. Physico-mechanical parameters employed in simulations. 23

Table 3-1. Linear Fracture Simulation Cases – Parameters. 63

Table 3-2. Linear Fracture Simulation Cases – Grid and Domain. 63

Table 3-3. Flow velocities. 64

Table 4-1. Parameters for the Opalinus and Bentonite clay. 91

LIST OF ACRONYMS

DFN	discrete fracture network
DRZ	disturbed rock zone
EDZ	excavation damaged zone
FE	Full-Scale Emplacement Experiment
FEPs	Features, Events and Processes
MB	mine-by
NBS	Natural Barrier System
THMC	thermal, hydrological, mechanical, and chemical
TPHM	two-part Hooke's model
R&D	Research & Development
RBSN	Rigid-Body-Spring-Network
SPHM	Single-part Hooke's model
UFDC	Used Fuel Disposition Campaign

Executive Summary

Objective

Clay/shale has been considered as potential host rock for geological disposal of high-level radioactive waste throughout the world. Coupled thermal, hydrological, mechanical, and chemical (THMC) processes have a significant impact on the long-term safety of a clay repository. For example, the excavation damaged zone (EDZ) near repository tunnels can modify local permeability (resulting from induced fractures), potentially leading to less confinement capability. This report documents results from three R&D activities: (1) implementation and validation of constitutive relationships, (2) development of a discrete fracture network (DFN) model for investigating coupled processes in the EDZ, and (3) development of a THM model for the FE tests at Mont Terri, Switzerland, for the purpose of model validation. The overall objective of these activities is to provide an improved understanding of EDZ evolution in clay repositories and the associated coupled processes, and to develop advanced relevant modeling capabilities.

The R&D activities documented in this report are part of the work package of natural system evaluation and tool development that directly supports the following Used Fuel Disposition Campaign (UFDC) objectives:

- Develop a fundamental understanding of disposal-system performance in a range of environments for potential wastes that could arise from future nuclear-fuel-cycle alternatives through theory, simulation, testing, and experimentation.
- Develop a computational modeling capability for the performance of storage and disposal options for a range of fuel-cycle alternatives, evolving from generic models to more robust models of performance assessment.

These activities address key Features, Events and Processes (FEPs), which have been ranked in importance from medium to high in the *Used Fuel Disposition Campaign Disposal Research and Development Roadmap* (FCR&D-USED-2011-000065 REV0) (Nutt, 2011). They also address a number of research topics identified in *Research & Development (R&D) Plan for Used Fuel Disposition Campaign (UFDC) Natural System Evaluation and Tool Development* (Wang, 2011), including Topics S3, Disposal system modeling – Natural system; P1, Development of discrete fracture network (DFN) model; and P15 Modeling of disturbed rock zone (DRZ) evolution (clay repository).

Major FY12 Accomplishments:

- Constitutive relationships are key elements for modeling coupled THMC processes. The two-part Hooke's model (TPHM), a new constitutive relationship, and associated formulations regarding rock hydraulic/mechanical properties were implemented into the

TOUGH-FLAC3D code. The usefulness and validity of the TPHM are demonstrated by the consistence between simulation results and field observations. A fine-grid numerical approach, based on an explicit incorporation of small-scale heterogeneity of mechanical properties and the TPHM, is used for investigating the EDZ formation and evolution.

- To more accurately characterize and model EDZ evolution and its impact on flow and transport, we developed a new three-dimensional DFN capability capable of addressing fracture initiation and propagation. The geomechanical and fracture-damage processes are simulated using the Rigid-Body-Spring-Network (RBSN) numerical method. The RBSN is further linked with TOUGH2 to compute coupled THM processes. Numerical grid generation for both the RBSN method and TOUGH2 is based on a Voronoi gridding method. The model results are found to be in good agreement with relevant observations and results obtained from independent numerical and analytical solution methods.

- The Full-Scale Emplacement Experiment (FE) at the Mont Terri URL, Switzerland will be one of the largest and longest-duration heater tests worldwide. It will provide data useful for the validation of THM coupling effects regarding the processes in the host rock while correctly accounting for (and examining) the conditions in the emplacement tunnel (temperature, saturation, and swelling pressure). For the purpose of validating modeling capabilities for THM processes, we performed preliminary TH and THM model simulations of the FE test. The parameters used in the model are primarily adopted from the previous laboratory and in-situ tests.

Suggested Future Work

In FY13, we will continue the current R&D activities. Constitutive relationships will be further refined to include impact of fracture formation on hydraulic properties within the context of continuum mechanics and validated with more data from the mining-by test at the Mont Terri URL. The DFN capability will be improved by including the effects of geomechanical strain on hydrogeologic properties. It will also be used to investigate fracture initiation and propagation induced by excavation as well as natural processes such as fluid overpressure and to determine conditions under which fractures can self-seal. The FE test model will be extended to three-dimensions and improved by considering anisotropic thermal and hydraulic properties for the Opalinus clay. Values for model input parameters will be refined by calibrating against relevant laboratory observations.

This page is intentionally blank.

1. Introduction

Clay/shale has been considered as potential host rock for geological disposal of high-level radioactive waste throughout the world, because of its low permeability, low diffusion coefficient, high retention capacity for radionuclides, and capability to self-seal fractures. For example, Callovo-Oxfordian argillites at the Bure site, France (Fouche et al., 2004), Toarcian argillites at the Tournemire site, France (Patriarche et al., 2004), Opalinus clay at the Mont Terri site, Switzerland (Meier et al., 2000), and Boom clay at the Mol site, Belgium (Barnichon and Volckaert, 2003) have all been under intensive scientific investigation (at both field and laboratory scales) for understanding a variety of rock properties and their relationships to flow and transport processes associated with geological disposal of radioactive waste. Figure 1-1 presents the distribution of clay/shale formations within the USA.

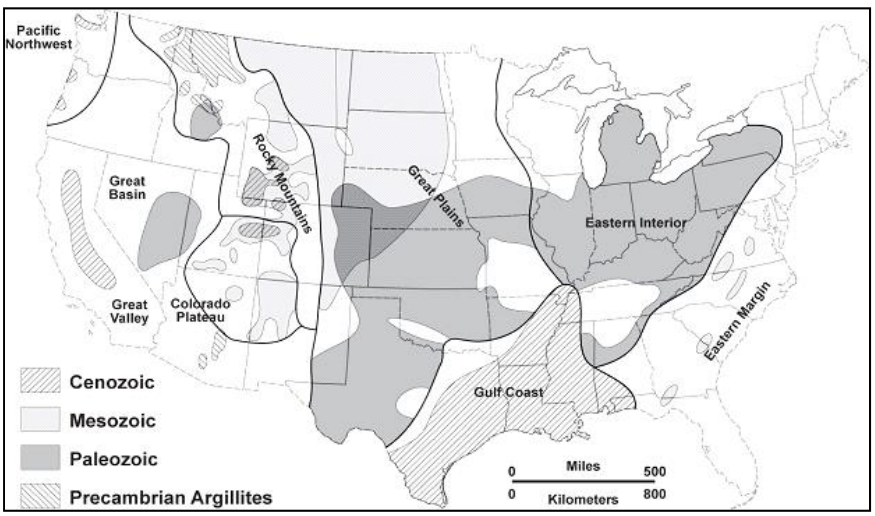

Figure 1-1. Clay/shale-formation distribution in the USA (Gonzales and Johnson, 1984).

Clay/shale rocks may be generally classified as indurated or plastic clays (Tsang et al., 2005). The latter (including Boom clay) is a softer material without high cohesion; its deformation is predominantly plastic. For both clay and shale, coupled thermal, hydrological, mechanical, and chemical (THMC) processes are expected to have a significant impact on the long-term safety of a clay repository. For example, the excavation damaged zone (EDZ) near repository tunnels can modify local permeability (resulting from induced fractures), potentially leading to less confinement capability (Tsang et al., 2005). Because of clay's tendency to swell or shrink (depending on whether the clay is in imbibition or drainage processes), fracture properties in the EDZ are quite dynamic and evolve over time as hydromechanical conditions change. Understanding and modeling the coupled processes and their impact on repository performance

are critical for any defensible performance assessment of a radioactive waste repository in clay/shale host rock.

Within the Natural Barrier System (NBS) group of the Used Fuel Disposition (UFD) Campaign at DOE's Office of Nuclear Energy, LBNL's research activities have focused on understanding and modeling EDZ evolution and the associated coupled processes. This report documents results from some of these activities. These activities address key Features, Events and Processes (FEPs), which have been ranked in importance from medium to high, as listed in Table 7 of the *Used Fuel Disposition Campaign Disposal Research and Development Roadmap* (FCR&D-USED-2011-000065 REV0) (Nutt, 2011). Specifically, they address FEP 2.2.01, Excavation Disturbed Zone, for shale, by investigating how coupled processes affect EDZ evolution; FEP 2.2.05, Flow and Transport Pathways; and FEP 2.2.08, Hydrologic Processes, and FEP 2.2.07, Mechanical Processes and FEP 2.2.09, Chemical Process—Transport, by studying near-field coupled THMC processes in clay/shale repositories. The activities documented in this report also address a number of research topics identified in *Research & Development (R&D) Plan for Used Fuel Disposition Campaign (UFDC) Natural System Evaluation and Tool Development* (Wang, 2011), including Topics S3, Disposal system modeling – Natural system; P1, Development of discrete fracture network (DFN) model; and P15 Modeling of disturbed rock zone (DRZ) evolution (clay repository).

This report documents progress made in LBNL's FY12 research activities, including implementation and validation of constitutive relationships (Chapter 2), development of a DFN model for investigating coupled processes in EDZ (Chapter 3), and development of a THM model for FE tests at Mont Terri, Switzerland, for the purpose of model validation (Chapter 4). A summary and discussion of future work activities are given in Chapter 5.

2. Implementation and Validation of the Constitutive Relationships

Constitutive relationships refer to relationships among hydraulic, mechanical, thermal, and mechanical properties. Accuracy in modeling coupled processes in a clay/shale repository is largely determined by the validity of these constitutive relationships and related parameter values. This chapter documents the progress made in FY12 in (1) implementation of the new constitutive relationships (that were developed in FY10 and FY11) into TOUGH-FLAC3D code (Section 2.2), (2) validation of the constitutive relationships by comparing simulation results with test observations (Section 2.3), and (3) investigation into evolution of the excavation damaged zone (EDZ) using a two-dimensional (2D) numerical model based on the new constitutive relationships (Section 2.4). The related uncertainty and its reduction are also discussed in Section 2.5.

2.1 A Brief Review of Previous Studies

2.1.1 Two-Part Hooke's Model (TPHM)

The stress–strain relationship is the most fundamental part of constitutive relationships. Hooke's law has been generally used to describe this stress–strain relationship for elastic mechanical processes. According to Hooke's law, for elastic material, the proportionality in the stress-strain relationship should be constant. However, this proportionality is in fact not always constant in many cases, but rather stress-dependent (e.g., Cazacu, 1999; Lionço and Assis, 2000; Brown et al., 1989; Johnson and Rasolofosaon, 1996; Brady, 1969). A number of efforts have been made to relate this stress-dependent behavior to the microstructures of "cracks" in porous rock (Walsh, 1965; Nur, 1971; Mavko and Nur, 1978)—an excellent review of these efforts is provided in a chapter entitled "Micromechanical Models" in Jaeger et al. (2007). Because it is generally difficult to characterize small-scale structures accurately and then relate their properties to large-scale mechanical properties that are of practical interest, it is desirable to have a macroscopic-scale theory that does not rely on the detailed description of small-scale structures, and that can physically incorporate the stress-dependent behavior of relevant mechanical properties. A theory of this kind was developed within the framework of Hooke's law by Liu et al. (2009) and is referred to as "TPHM" in this study.

Liu et al. (2009) argued that different varieties of Hooke's law should be applied within regions of the rock having significantly different stress–strain behavior, and that a rock body could be conceptualized into two distinct parts. These two parts are called a "hard part," which undergoes only small deformation, and a "soft part," which undergoes large deformation. The natural strain (volume change divided by rock volume at the current stress state), rather than the engineering strain (volume change divided by the unstressed rock volume), should be used in Hooke's law for accurate modeling of the elastic deformation of the pore volume's soft part, subject to a relatively large degree of relative deformation (i.e., cracks or fractures). This approach permits the derivation of constitutive relationships between stress and a variety of mechanical and/or

hydraulic rock properties. The theoretical predictions using this method are generally consistent with empirical expressions and also laboratory rock experimental data.

The theory of Liu et al. (2009), here called TPHM, is limited to isotropic stress conditions corresponding to the hydrostatic stress state. In reality, a clay repository is generally subject to complex, anisotropic stress conditions. In FY11, we extended the TPHM to such conditions. In FY12, we implemented the TPHM into a coupled hydro-mechanical simulator and validated it by comparing the simulation results with observations. While the THPM was developed for elastic processes, we also considered damage processes (within the context of continuum mechanics) in this study, although the consideration is very preliminary at this stage.

2.1.2 Modeling EDZ Evolution

The excavation-damaged zone (EDZ) is a zone in which hydromechanical and geochemical modifications induce significant changes in flow and transport properties (Tsang et al., 2005). The EDZ is also sometimes referred to as the "disturbed rock zone" (DRZ) (Stormont 1997; Kruschwitz and Yaramanci 2004). EDZ evolution is of great interest in the field of radioactive waste management, because the EDZ may provide pathways for groundwater flow (and potentially radionuclide transport) around an underground radioactive-waste repository.

Modeling of construction-induced effects in the far field has been shown to be feasible in clay-rich host rock using advanced THM coupled codes. In contrast, modeling of the formation and evolution of the EDZ is very challenging. Modeling of the EDZ extent depends on the constitutive law used and the choice of elastic limit and fracturing criteria. It is important to ensure that the numerical model is capable of characterizing the entire fracturing process involving the initiation, propagation, and coalescence of microcracks in the host rock, and that modeling results indeed represent the physics of the involved processes (Tsang et al., 2012).

In recent developments, micromechanical models, including fine-grid numerical approaches, have been developed to simulate the instability or loss of integrity of a tunnel or borehole. These models have improved our understanding of the mechanisms and consequences of fracture initiation and propagation. For example, the nonlinear rule-based model (Blair and Cook 1998), the lattice model (Chinaia et al., 1997) and the bonded particle model (Potyondy et al., 1996; Hazzard and Young 2000) have been found capable of simulating the fracture processes of quasi-brittle materials, such as rock, by accounting for microscopic aspects of rock fracture and the crack-propagation mechanism (Germanovich and Dyskin 2000). Based on an elastic-brittle-damage model, a numerical code called RFPA has been developed and used to model fracturing behavior in rocks around small-scale openings (Tang and Hudson 2010; Zhu et al., 2005). An elasto-plastic damage model, based on the mesh-free smoothed particle hydrodynamics (SPH) method, has been developed to simulate the failure of brittle heterogeneous materials (Ma et al., 2011). However, none of these models is capable of simulating the progressive fracturing

process in rocks around full-scale underground openings, characterized by initiation, propagation, and coalescence of cracks, resulting in strain localization and stress redistribution. In view of that, a local degradation model based on the FLAC code (Itasca, 2005) was proposed by Fang and Harrison (2002) during their fine-grid numerical simulations (in which a continuum approach is used and the small-scale heterogeneity of mechanical properties is explicitly considered). The local degradation model has been employed to simulate fracturing processes in both mine pillars and laboratory-scale rock specimens in compression, and should also be useful for modeling the mechanical response of the EDZ around underground openings.

In addition to the typical challenges of EDZ analysis in rock, there has been further concern regarding the short-term stress–strain behavior of rock, because analysis using linear-elastic or elasto-plastic methods based on the conventional Hooke's law has, as previously indicated, generally been unsatisfactory in capturing the nonlinear deformation behavior of a rock mass. It has been widely reported that in many cases, during the excavation of underground tunnel openings, unusually large deformations have been observed around these openings (Nawrocki et al., 1998; Lionco and Assis 2000; Corkum and Martin 2007a; Weng et al., 2008). The TPHM, which accounts for nonlinear behavior in the elastic deformation of rock, is used for modeling EDZ evolution in this study. Note that, prior to this study, the TPHM has not yet been used in modeling coupled hydrological-mechanical processes under field conditions. The incorporation of the TPHM in the analysis of the behavior of underground excavations is expected to more accurately capture the displacements and stress distributions and the failure mode of the EDZ.

In FY12, we have used a fine-grid numerical approach to model progressive failure related to EDZ evolution around a tunnel opening in clay rock. This approach captures the heterogeneity of rock at the meso-level, using a probabilistic variation of the mechanical properties of the materials. The stress–strain relationship is governed by the TPHM, which is implemented in TOUGH-FLAC3D. Then, we have tried to trace microscopic crack development and propagation, as well as macromechanical responses during EDZ formation.

2.2 Implementation of Constitutive Relationships

In this section, first we introduce the implementation of TPHM in TOUGH-FLAC3D, after which we discuss the hydro-mechanical local-degradation model. This degradation model uses an elemental constitutive relationship to describe degradation in both the strength and stiffness of rock. Finally, we present a practical approach for dealing with the stress-dependence of permeability for damaged rock mass.

2.2.1. Implementation of TPHM in TOUGH-FLAC3D

In this study, all numerical simulations were conducted using the coupled reservoir-geomechanical simulator, TOUGH-FLAC3D code. TOUGH-FLAC3D, which links the two

established codes TOUGH2 and FLAC3D, was presented as a pragmatic approach for modeling coupled multiphase flow, heat transport, and geomechanics (Rutqvist et al., 2002). In this approach, TOUGH2 (Pruess et al., 1999) is used for solving multiphase flow and heat transport equations, whereas FLAC3D (Itasca, 2005) is used for solving geomechanical stress–strain equations. The two codes are sequentially coupled, and a TOUGH-FLAC3D simulation runs seamlessly on a PC. One great advantage of this approach is that both codes are being continuously developed and are widely used in both academia and industry.

FLAC3D (Itasca, 2005), a powerful numerical analysis tool for modeling soil, rock, and structural behavior, has been widely used in the fields of geotechnical, geomechanical, civil and mining engineering. FLAC3D uses dynamic equations of motion in its explicit, time-marching scheme. The solution of solid body problems in FLAC3D invokes the equations of motion (Newton's law of motion), constitutive relationships, and boundary conditions.

When running the FLAC3D code in its mechanical or thermomechanical configuration mode, it solves the equation of motion,

$$\nabla \cdot \boldsymbol{\sigma} + \rho_m \mathbf{g} = \rho_m \frac{d\mathbf{v}}{dt} \tag{2-1}$$

in an iterative manner with the stress–strain relationship, where ρ_m is average density of the rock mass and $\mathbf{v}$ is solid velocity with respect to a fixed system. The incremental stress and strain during a time step is governed by various elastic or elasto-plastic constitutive laws, which can be written in a general form as

$$\Delta\sigma' = \mathbf{H}(\sigma', \dot{\varepsilon}\Delta t) \tag{2-2}$$

in which $\mathbf{H}$ contains given material functions, $\dot{\varepsilon}$ is the infinitesimal strain-rate tensor, and Δt is a time increment. Equation (2-2) is valid for a small strain, but in the FLAC3D code, a large strain formulation can be invoked, in which the stress tensor is corrected for rotational strains.

In TOUGH-FLAC3D, FLAC3D is invoked from TOUGH2 using a system call. By using the coupling module, in which FLAC3D FISH routines that handle the links between FLAC3D and TOUGH2 are included, the effective stress σ' and strain ε (computed in FLAC3D) are passed to TOUGH2 for calculation of the updated porosity ϕ and permeability. The multiphase flow simulation data obtained from TOUGH2 (namely pressure P, temperature T) are passed to FLAC3D for processing and estimating their impact on the effective stress $\alpha\Delta P$ (α being Biot's effective stress parameter), as well as on thermal strain (ε^{T}).

The infinitesimal strain rate, $\dot{\varepsilon}$, and infinitesimal strain, ε is governed by the restrictions

$$\dot{\varepsilon} = \frac{1}{2}(\nabla\mathbf{v} + (\nabla\mathbf{v})^{tr}) \qquad \varepsilon = \frac{1}{2}(\nabla\mathbf{u} + (\nabla\mathbf{u})^{tr}), \tag{2-3}$$

where *tr* denotes the transpose of a tensor and $\mathbf{u}$ is the displacement (vector). As usual, the total strain increment can be decomposed into elastic, plastic, and thermal expansion parts, according to:

$$\Delta\varepsilon = \Delta\varepsilon^{\mathbf{e}} + \Delta\varepsilon^{\mathbf{P}} + \Delta\varepsilon^{\mathbf{T}}, \tag{2-4}$$

where the thermal strain is given by

$$\Delta\varepsilon^{\mathbf{T}} = \mathbf{I}\beta_{\mathbf{T}}\Delta T \tag{2-5}$$

and where $\beta_{\mathbf{T}}$ is the linear thermal expansion coefficient.

The constitutive laws in Equation (2-2) work on the effective stress, which can be calculated (by invoking the FLAC3D groundwater configuration) as:

$$\boldsymbol{\sigma}' = \boldsymbol{\sigma} + \mathbf{I}\alpha P, \tag{2-6}$$

where α is Biot's effective stress parameter (Biot, 1941) and P is pore pressure.

FLAC3D provides material models such as Mohr–Coulomb and Hoek–Brown failure criteria that are suitable for geotechnical materials. All of these models are provided as dynamic-linked libraries (DLLs) that are loaded when FLAC3D is first executed (Itasca, 2005). Users can modify these models or create their own constitutive models as DLLs.

All constitutive models in FLAC3D share the same incremental numerical algorithm. Given the stress state at time *t*, and the strain increment for a time step Δt, the purpose of the constitutive models is to determine the corresponding stress increment and the new stress state at time $t + \Delta t$. When plastic deformations are involved, only the elastic part of the strain increment will contribute to the stress increment. In this case, a correction must be made to the elastic stress increment (as computed from the total strain increment) in order to obtain the actual stress state for the new time step.

As a stress-strain relationship, the TPHM can be implemented into any models provided by FLAC3D. There are thirteen basic constitutive models provided in FLAC3D, arranged into null, elastic, and plastic model groups. The most commonly used criteria plastic-model groups are those of Mohr-Coulomb, Hoek and Brown, and the Cam-Clay model, in which the Mohr-Coulomb model is often used to represent failure in soils and rocks because of its simple form (Vermeer and deBorst, 1984; Sheldon, 2009; Itasca Consulting Group, 2005). In this study, as a demonstration, the TPHM was implemented into the Mohr–Coulomb model.

In FLAC3D, the failure envelope for the Mohr–Coulomb model corresponds to a Mohr-Coulomb criterion (shear yield function) with tension cutoff (tension yield function). The position of a stress point on this envelope is controlled by a non-associated flow rule for shear failure, and an associated rule for tension failure. Note that all models in FLAC3D operate on effective stresses only.

The Mohr-Coulomb criterion in FLAC3D is expressed in terms of the principal stresses σ_1, σ_2 and σ_3, which are the three components of the generalized stress vector for this model. This criterion may be represented in the plane (σ_1, σ_3) as illustrated in Figure 2-1. The failure envelope $f(\sigma_1, \sigma_3) = 0$ is defined from point *A* to *B* by the Mohr-Coulomb failure criterion $f^S = 0$, with

$$f^S = \sigma_1 - \sigma_3 N_\varphi + 2c\sqrt{N_\varphi} \tag{2-7}$$

and from *B* to *C* by a tension failure criterion of the form $f^t = 0$, with

$$f^t = \sigma_3 - \sigma^t \tag{2-8}$$

where φ is the friction angle, *c*, the cohesion, σ^t , the tensile strength, and

$$N_\varphi = \frac{1 + \sin\varphi}{1 - \sin\varphi} \tag{2-9}$$

Note that the tensile strength of the material cannot exceed the value of σ_3 corresponding to the intersection point of the straight lines $f^t = 0$ and $\sigma_1 = \sigma_3$ in the $f(\sigma_1, \sigma_3)$ plane. This maximum value is given by

$$\sigma^t_{\max} = \frac{c}{\tan\varphi} \tag{2-10}$$

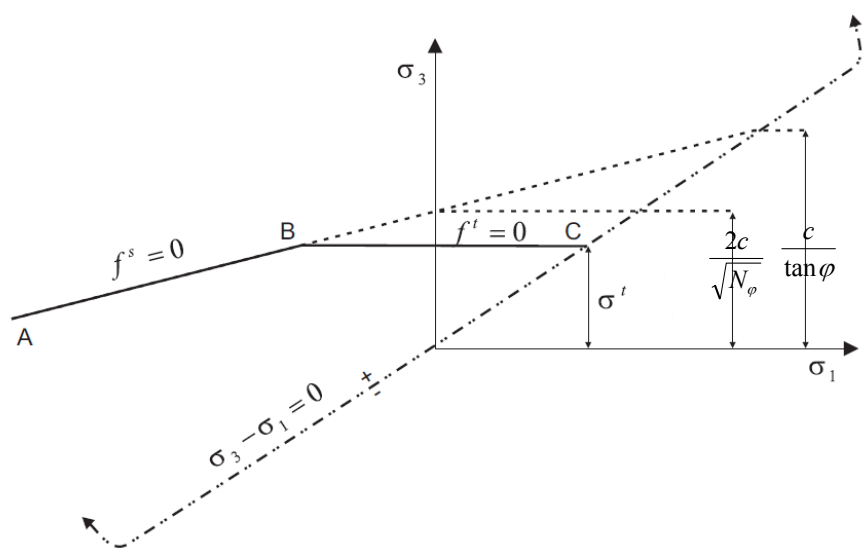

Figure 2-1. Sketch of the Mohr-Coulomb failure criterion employed in FLAC3D.

In the implementation of the Mohr-Coulomb model in FLAC3D, an elastic guess (σ^I_{ij}) is first computed by application of Hooke's law to the strain increments $\Delta\varepsilon_{ij}$. In the elastic, isotropic model, strain increments generate stress increments according to the conventional Hooke's law (Single-part Hooke's model, abbreviated as SPHM):

$$\Delta\sigma_{ij}^{SPHM} = 2G\Delta\varepsilon_{ij} + \alpha_2 \Delta\varepsilon_{kk}\delta_{ij}, \tag{2-11}$$

where the Einstein summation convention applies, δ_{ij} is the Kronecker delta symbol $\delta_{ij} = \begin{cases} 1, & (i = j) \\ 0, & (i \neq j) \end{cases}$, and α_2 is a material constant related to the bulk modulus, *K*, and shear modulus, *G*, as

$$\alpha_2 = K - \frac{2}{3}G \tag{2-12}$$

New stress values, elastic guess (σ_{ij}^I), are then obtained from the relationship

$$\sigma_{ij}^I = \sigma_{ij}^O + \Delta\sigma_{ij}^{SPHM} \tag{2-13}$$

where σ_{ij}^O are the initial stresses at time *t*. The principal stresses σ_1^I , σ_2^I , σ_3^I and corresponding directions are then calculated. If the stresses σ_1^I , σ_2^I , σ_3^I violate the composite yield criterions, Equation (2-7) or (2-8), plastic deformation takes place. The new principal stress components are corrected by using the plastic flow rule to ensure that they lie on the yield surface. If point (σ_1^I, σ_3^I) is located below the representation of the composite failure envelope in the plane (σ_1, σ_3), no plastic flow takes place for this step, and the new principal stresses are given by σ_i^I, (i = 1,3).

Most recently, Zhao and Liu (2011) extended the TPHM to anisotropic stress conditions. Based on the assumption that the principal strain resulting from the soft part is a function of the principal stress along the same direction only (and has nothing to do with any other principal stresses), and the soft part in each principal orientation occupies the same portion of the whole soft part, the stress-strain relations are given by

$$\left.\begin{aligned} \varepsilon_1 &= \frac{(3-\gamma_t)}{3E_e}\left[\sigma_1 - \nu(\sigma_2+\sigma_3)\right] + \frac{\gamma_t}{3}\left[1-\exp\left(-\frac{\sigma_1}{E_t}\right)\right] \\ \varepsilon_2 &= \frac{(3-\gamma_t)}{3E_e}\left[\sigma_2 - \nu(\sigma_1+\sigma_3)\right] + \frac{\gamma_t}{3}\left[1-\exp\left(-\frac{\sigma_2}{E_t}\right)\right] \\ \varepsilon_3 &= \frac{(3-\gamma_t)}{3E_e}\left[\sigma_3 - \nu(\sigma_2+\sigma_1)\right] + \frac{\gamma_t}{3}\left[1-\exp\left(-\frac{\sigma_3}{E_t}\right)\right] \end{aligned}\right\} \tag{2-14}$$

where $\sigma_1, \sigma_2, \sigma_3$ are effective principal stresses, $\varepsilon_1, \varepsilon_2, \varepsilon_3$ are principal engineering strains, ν is Poisson ratio for the hard part, γ_t is the ratio of the soft part to the entire rock body in one principal orientation and has a value, obtained through experimental tests, on order 10^{-1}~10^{-2}, and E_e and E_t refer to Young's (elastic) modulus for the hard and soft part, respectively. Note that for $\gamma_t = 0$, Equation (2-14) is reduced to the conventional stress-strain relationship (Hooke's law).

To implement the numerical routine in simulators, we transform the principal stress/strain coordinate system into a global coordinate system (x, y, z). Based on Equation (2-14), the general stress-strain relationship in a global coordinate system (x, y, z) can be calculated as (Zhao and Liu, 2011)

$$\left.\begin{aligned}
\varepsilon_x &= \frac{(3-\gamma_t)}{3E_e}\left[\sigma_x - \nu(\sigma_y+\sigma_z)\right] + \frac{\gamma_t}{3}\left[1-\exp\left(-\frac{\sigma_1}{E_t}\right)l_1^2 - \exp\left(-\frac{\sigma_2}{E_t}\right)l_2^2 - \exp\left(-\frac{\sigma_3}{E_t}\right)l_3^2\right] \\
\varepsilon_y &= \frac{(3-\gamma_t)}{3E_e}\left[\sigma_y - \nu(\sigma_x+\sigma_z)\right] + \frac{\gamma_t}{3}\left[1-\exp\left(-\frac{\sigma_1}{E_t}\right)m_1^2 - \exp\left(-\frac{\sigma_2}{E_t}\right)m_2^2 - \exp\left(-\frac{\sigma_3}{E_t}\right)m_3^2\right] \\
\varepsilon_z &= \frac{(3-\gamma_t)}{3E_e}\left[\sigma_z - \nu(\sigma_x+\sigma_y)\right] + \frac{\gamma_t}{3}\left[1-\exp\left(-\frac{\sigma_1}{E_t}\right)n_1^2 - \exp\left(-\frac{\sigma_2}{E_t}\right)n_2^2 - \exp\left(-\frac{\sigma_3}{E_t}\right)n_3^2\right] \\
\gamma_{xy} &= \frac{2(3-\gamma_t)(1+\nu)}{3E_e}\tau_{xy} + \frac{2\gamma_t}{3}\left[\exp\left(-\frac{\sigma_1}{E_t}\right) - \exp\left(-\frac{\sigma_2}{E_t}\right)\right]l_2m_2 + \frac{2\gamma_t}{3}\left[\exp\left(-\frac{\sigma_1}{E_t}\right) - \exp\left(-\frac{\sigma_3}{E_t}\right)\right]l_3m_3 \\
\gamma_{xz} &= \frac{2(3-\gamma_t)(1+\nu)}{3E_e}\tau_{xz} + \frac{2\gamma_t}{3}\left[\exp\left(-\frac{\sigma_1}{E_t}\right) - \exp\left(-\frac{\sigma_2}{E_t}\right)\right]l_2n_2 + \frac{2\gamma_t}{3}\left[\exp\left(-\frac{\sigma_1}{E_t}\right) - \exp\left(-\frac{\sigma_3}{E_t}\right)\right]l_3n_3 \\
\gamma_{yz} &= \frac{2(3-\gamma_t)(1+\nu)}{3E_e}\tau_{yz} + \frac{2\gamma_t}{3}\left[\exp\left(-\frac{\sigma_1}{E_t}\right) - \exp\left(-\frac{\sigma_2}{E_t}\right)\right]m_2n_2 + \frac{2\gamma_t}{3}\left[\exp\left(-\frac{\sigma_1}{E_t}\right) - \exp\left(-\frac{\sigma_3}{E_t}\right)\right]m_3n_3
\end{aligned}\right\} \quad (2\text{-}15)$$

where x, y, z denote the directions of coordinate axes in a global coordinate system (x, y, z), $l_i = \cos(i,x)$, $m_i = \cos(i,y)$, $n_i = \cos(i,z)$, and $i = 1,2,3$ is the index for the direction of the ith principal stress. The functions $\cos(i,x)$, $\cos(i,y)$ and $\cos(i,z)$ are the cosine of the angles between i and the x, y, and z directions, respectively, and are given as:

$$\left.\begin{aligned}
\cos(i,x) &= \frac{(\sigma_y-\sigma_i)(\sigma_z-\sigma_i)-\tau_{zy}\tau_{yz}}{\sqrt{[(\sigma_y-\sigma_i)(\sigma_z-\sigma_i)-\tau_{zy}\tau_{yz}]^2+[\tau_{zy}\tau_{xz}-\tau_{xy}(\sigma_z-\sigma_i)]^2+[\tau_{xy}\tau_{yz}-\tau_{xz}(\sigma_y-\sigma_i)]^2}} \\
\cos(i,y) &= \frac{\tau_{zy}\tau_{xz}-\tau_{xy}(\sigma_z-\sigma_i)}{\sqrt{[(\sigma_y-\sigma_i)(\sigma_z-\sigma_i)-\tau_{zy}\tau_{yz}]^2+[\tau_{zy}\tau_{xz}-\tau_{xy}(\sigma_z-\sigma_i)]^2+[\tau_{xy}\tau_{yz}-\tau_{xz}(\sigma_y-\sigma_i)]^2}} \\
\cos(i,z) &= \frac{\tau_{xy}\tau_{yz}-\tau_{xz}(\sigma_y-\sigma_i)}{\sqrt{[(\sigma_y-\sigma_i)(\sigma_z-\sigma_i)-\tau_{zy}\tau_{yz}]^2+[\tau_{zy}\tau_{xz}-\tau_{xy}(\sigma_z-\sigma_i)]^2+[\tau_{xy}\tau_{yz}-\tau_{xz}(\sigma_y-\sigma_i)]^2}}
\end{aligned}\right\} \quad (2\text{-}16)$$

Details on the derivations of Equation (2-14), (2-15) and (2-16) can be found in previous studies (Liu et al., 2009; Zhao and Liu, 2011). To incorporate the TPHM into the Mohr-Coulomb model within FLAC3D, the stress increments, $\Delta\sigma_{ij}^{SPHM}$, in Equation (2-11) and (2-13) is replaced by $\Delta\sigma_{ij}^{TPHM}$. The $\Delta\sigma_{ij}^{TPHM}$ can be directly obtained by calculating the following equation:

$$\left.\begin{aligned}
d\varepsilon_x &= \frac{(3-\gamma_t)}{3E_e}\left[d\sigma_x - \nu\left(d\sigma_y + d\sigma_z\right)\right] + d\varepsilon_{xt} \\
d\varepsilon_y &= \frac{(3-\gamma_t)}{3E_e}\left[d\sigma_y - \nu\left(d\sigma_x + d\sigma_z\right)\right] + d\varepsilon_{yt} \\
d\varepsilon_z &= \frac{(3-\gamma_t)}{3E_e}\left[d\sigma_z - \nu\left(d\sigma_x + d\sigma_y\right)\right] + d\varepsilon_{zt} \\
d\gamma_{xy} &= \frac{2(3-\gamma_t)(1+\nu)}{3E_e} d\tau_{xy} + d\gamma_{xyt} \\
d\gamma_{xz} &= \frac{2(3-\gamma_t)(1+\nu)}{3E_e} d\tau_{xz} + d\gamma_{xzt} \\
d\gamma_{yz} &= \frac{2(3-\gamma_t)(1+\nu)}{3E_e} d\tau_{yz} + d\gamma_{yzt}
\end{aligned}\right\} \tag{2-17}$$

Equation (2-17) is an incremental formulation of Equation (2-15). In Equation (2-17), the strain increments $d\varepsilon_x$, $d\varepsilon_y$, $d\varepsilon_z$, $d\gamma_{xy}$, $d\gamma_{xz}$, $d\gamma_{yz}$ are known values, i.e., $\Delta\varepsilon_{ij}$; while the right items $d\varepsilon_{xt}$, $d\varepsilon_{yt}$, $d\varepsilon_{zt}$, $d\gamma_{xyt}$, $d\gamma_{xzt}$, $d\gamma_{yzt}$ are the strain increments for the soft part and can be expressed as

$$\left.\begin{aligned}
d\varepsilon_{xt} &= \frac{\gamma_t}{3E_t}\left[\exp\left(-\frac{\sigma_1}{E_t}\right)l_1^2 d\sigma_1 + \exp\left(-\frac{\sigma_2}{E_t}\right)l_2^2 d\sigma_2 + \exp\left(-\frac{\sigma_3}{E_t}\right)l_3^2 d\sigma_3\right] \\
d\varepsilon_{yt} &= \frac{\gamma_t}{3E_t}\left[\exp\left(-\frac{\sigma_1}{E_t}\right)m_1^2 d\sigma_1 + \exp\left(-\frac{\sigma_2}{E_t}\right)m_2^2 d\sigma_2 + \exp\left(-\frac{\sigma_3}{E_t}\right)m_3^2 d\sigma_3\right] \\
d\varepsilon_{zt} &= \frac{\gamma_t}{3}\left[\exp\left(-\frac{\sigma_1}{E_t}\right)n_1^2 d\sigma_1 + \exp\left(-\frac{\sigma_2}{E_t}\right)n_2^2 d\sigma_2 + \exp\left(-\frac{\sigma_3}{E_t}\right)n_3^2 d\sigma_3\right] \\
d\gamma_{xyt} &= \frac{2\gamma_t}{3E_t}\left[\exp\left(-\frac{\sigma_2}{E_t}\right)d\sigma_2 - \exp\left(-\frac{\sigma_1}{E_t}\right)d\sigma_1\right]l_2 m_2 + \frac{2\gamma_t}{3}\left[\exp\left(-\frac{\sigma_3}{E_t}\right)d\sigma_3 - \exp\left(-\frac{\sigma_1}{E_t}\right)d\sigma_1\right]l_3 m_3 \\
d\gamma_{xzt} &= \frac{2\gamma_t}{3E_t}\left[\exp\left(-\frac{\sigma_2}{E_t}\right)d\sigma_2 - \exp\left(-\frac{\sigma_1}{E_t}\right)d\sigma_1\right]l_2 n_2 + \frac{2\gamma_t}{3}\left[\exp\left(-\frac{\sigma_3}{E_t}\right)d\sigma_3 - \exp\left(-\frac{\sigma_1}{E_t}\right)d\sigma_1\right]l_3 n_3 \\
d\gamma_{yzt} &= \frac{2\gamma_t}{3E_t}\left[\exp\left(-\frac{\sigma_2}{E_t}\right)d\sigma_2 - \exp\left(-\frac{\sigma_1}{E_t}\right)d\sigma_1\right]m_2 n_2 + \frac{2\gamma_t}{3}\left[\exp\left(-\frac{\sigma_3}{E_t}\right)d\sigma_3 - \exp\left(-\frac{\sigma_1}{E_t}\right)d\sigma_1\right]m_3 n_3
\end{aligned}\right\} \tag{2-18}$$

In Equation (2-18), the principal stresses σ_1, σ_2, and σ_3 are the known values. Based on the stress transformations in three dimensions (Poulos and Davis, 1974; Jaeger et al., 2007), one can obtain σ_1, σ_2, and σ_3 using the stresses σ_{ij}^O at time *t*. An algorithm function for calculating σ_1, σ_2, and σ_3 has been provided by the module of the C++ source code for the Mohr–Coulomb model in FLAC3D. While the principal stress increments $d\sigma_1$, $d\sigma_2$, and $d\sigma_3$ in Equation (2-18) can be expressed as

$$\left.\begin{aligned} d\sigma_1 &= d\sigma_x l_1^2 + d\sigma_y m_1^2 + d\sigma_z n_1^2 + 2d\tau_{xy} l_1 m_1 + 2d\tau_{xz} l_1 n_1 + 2d\tau_{yz} m_1 n_1 \\ d\sigma_2 &= d\sigma_x l_2^2 + d\sigma_y m_2^2 + d\sigma_z n_2^2 + 2d\tau_{xy} l_2 m_2 + 2d\tau_{xz} l_2 n_2 + 2d\tau_{yz} m_2 n_2 \\ d\sigma_3 &= d\sigma_x l_3^2 + d\sigma_y m_3^2 + d\sigma_z n_3^2 + 2d\tau_{xy} l_3 m_3 + 2d\tau_{xz} l_3 n_3 + 2d\tau_{yz} m_3 n_3 \end{aligned}\right\} \quad (2\text{-}19)$$

where l_i, m_i, and n_i ($i = 1,2,3$) can be calculated by Equation (2-16). Based on Equations (2-17), (2-18) and (2-19), we can get $d\sigma_x$, $d\sigma_y$, $d\sigma_z$, $d\tau_{xy}$, $d\tau_{xz}$, and $d\tau_{yz}$, that correspond to $\Delta\sigma_{ij}^{TPHM}$ in Equation (2-13).

Here, we need to indicate that the TPHM is only applicable to compression conditions. Under a tension condition, the strain for the soft part would become unrealistically large because of the exponential dependence of strain on stress. However, it is reasonable to consider that the soft part, just like a fracture, cannot sustain tensions, and thus the SPHM is used in this case. In other words, if one of the principal stresses is in tension, the strain for the soft part *in the same direction* as principal stress will be omitted. Then SPHM is used in this principal orientation (Equation (2-11)), and TPHM is used in the other principal orientations. If all of the three principal stresses are in tension, the stress increments are still given by Equation (2-11).

Using the programming language C++, the TPHM was incorporated into FLAC3D. The computational scheme implemented in FLAC3D is shown in Figure 2-2. The modified Mohr–Coulomb model written in C++ was compiled as a DLL file that can be loaded whenever it is needed.

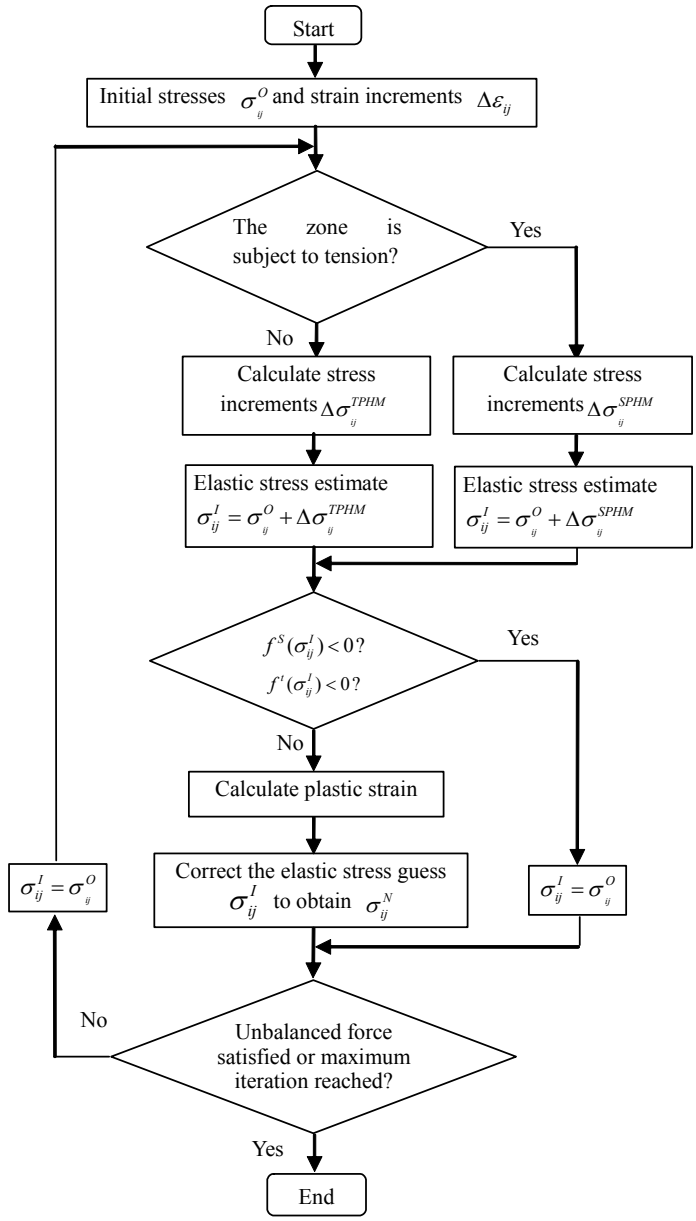

Figure 2-2. Computational scheme for the numerical implementation of the TPHM into FLAC3D.

2.2.2. The degradation of rock properties after failure

Rock consists of crystals, grains, voids, pores, cracks, and the like. Under applied load, these microstructures interact with each other to give rise to a corresponding macroscopic mechanical response. Regardless of rock type, the microscopic processes occurring within compressively stressed rock materials are similar. These processes follow the sequence of initiation, propagation, and coalescence of microcracks, leading to the eventual formation of macroscopic fractures. As a consequence, in order to trace isolated fracture processes, heterogeneity must be represented and introduced appropriately.

Here, the failure-process simulation is performed using FLAC3D as the basic stress-analysis tool, where the eight-node isoparametric element (zone) is used as the basic element in the finite difference method (FDM) analysis, and the elastic damage-based constitutive relationship of meso-level elements is incorporated. The mechanical parameters of the element, such as Young's modulus, strength, and Poisson's ratio, are heterogeneous and assumed to conform to the Weibull distribution (Weibull 1951). In a general study on rock fracture, we therefore consider as the basis for heterogeneity the adaptable Weibull distribution function, which is given by

$$f(u) = \frac{m}{u_0}\left(\frac{u}{u_0}\right)^{m-1} \exp\left(-\frac{u}{u_0}\right)^{m} \tag{2-20}$$

where u is the parameter of the element (such as the Young's modulus, Poisson's ratio, strength properties, permeability, and heat conductivity), the scale parameter u_0 is related to the average of the element parameter, and the homogeneity index m defines the shape of the distribution function and represents the degree of material homogeneity. A heterogeneous material can be produced numerically in a computer simulation for a material composed of many elements. Each element is assumed to be isotropic and homogeneous. Higher homogeneity indices lead to more homogeneous numerical samples (Tang et al., 2000; Wong et al., 2006).

It is generally known that the progressive degradation of material properties results from the initiation, growth, and coalescence of microcracks, which eventually induce the macroscopic failure. The deformation and macroscopic response of rocks is usually expressed through the use of a stress–strain curve obtained from laboratory experiments. In terms of degradation, it is seen from stress–strain curves that, in uniaxial compression, the rock displays sudden degradation in both strength and stiffness (i.e., very brittle behavior) after attainment of the peak stress. The mechanical behavior of rock evolves from elastic–brittle to elastic–brittle–ductile with increasing confining pressure. Using this observation in conjunction with idealized piece-wise linear differential stress–strain curves, studies have shown that degradation in both strength and stiffness can be unified through a degradation index $\mathrm{r_d}$ (Fang and Harrison 2002), which may be formulated as

$$\mathrm{r_d} = \frac{\delta\sigma_{\mathrm{p}}}{\delta\sigma_0} = \frac{\delta \mathrm{S_p}}{\delta \mathrm{S_0}} \tag{2-21}$$

As shown in the diagram of Figure 2-3, σ_c and σ_{cd} are the peak strength and residual strength under uniaxial stress state, and σ_p and σ_{pd} are the hypothetical peak strength and residual strength with confining pressure. The terms $\delta\sigma_0$ and $\delta\sigma_{\mathrm{p}}$ are the strength differences for uniaxial and general triaxial conditions, respectively. Terms $\delta \mathrm{S_0}(= \mathrm{S_0} - \mathrm{S_{0d}})$ and $\delta \mathrm{S_p}(= \mathrm{S_0} - \mathrm{S_{pd}})$ are the corresponding stiffness differences. The definition of the degradation index implies that the value of $\mathrm{r_d}$ ranges from zero (no degradation, ductile failure) to unity (complete degradation,

brittle failure). It has been suggested (Fang and Harrison 2002) that the relationship between the degradation index and confining pressure can conveniently be expressed as

$$r_d = \exp(-n_d \sigma_3) \tag{2-22}$$

where n_d is a degradation parameter and σ_3 is the confining pressure. This index has been shown to be capable of describing the degrading behavior of rock under laboratory tests, as well as serving as a functional relationship for modeling the process of rock fracturing.

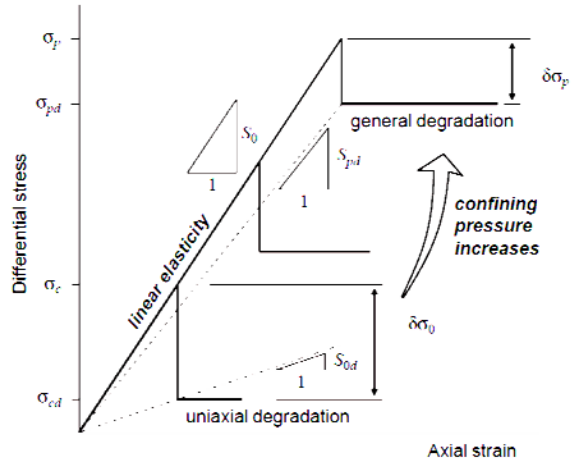

Figure 2-3. Sketch of the definition of the degradation indices (Yuan and Harrison, 2005).

The degradation of strength and stiffness is an essential component of the local degradation approach. This degradation means that intact rock alters into a more deformable and weaker material. This altered material can conceptually be regarded as being fractured, with the result that other material properties should take on values that are appropriate for a fractured material. Once an element (zone) becomes the conceptual fracture, the residual elemental stiffness, S_r, and the normalized residual strength, σ_r, are thus given by

$$\left.\begin{aligned} S_r &= S_p(1-r_d) \\ \sigma_r &= \sigma_p(1-r_d) \end{aligned}\right\} \tag{2-23}$$

On the basis of the above equations that quantify the post-peak degradation, a material suffers from elasticity (no degradation, $r_d = 0$) to complete damage (complete degradation, $r_d = 1$). The resulting idealized stress–strain constitutive relationships, together with the elemental heterogeneity in mechanical properties, are then used to model the initiation and coalescence of rock fractures in rock that is subjected to various compressive stress states.

FLAC3D has been adopted for the implementation of the degradation model above. After the geometry of the problem under investigation has been defined, heterogeneity in both the uniaxial compressive strength and the tensile strength is generated using the Weibull distribution function. Then, other material property parameters and the initial boundary conditions are

specified. Following this procedure, the model is brought to equilibrium under the initial boundary conditions. At this stage, a perturbation that produces strain increments may be applied, as well as an elastic solution of stress computed by application of a constitutive relationship to the total strain increment. Then, the magnitudes and directions of the principal stresses are calculated and ordered, and if these stresses violate the elemental failure criterion (Equations (2-7) and (2-8)), the appropriate plastic flow or degradations in strength and stiffness are applied to the element. FLAC3D allows degradation to be modeled easily: stiffness degradation is implemented by simply updating the degraded value in stress–strain calculations; strength degradation is implemented by reducing the material cohesive strength, or the internal friction angle, or both. The degradation in effect causes stress and strain changes in the element's surroundings, and these are used in the succeeding cycle of calculations, together with any further stress disturbances that may have been generated.

In modeling studies with FLAC3D, elements whose ultimate tensile or shear strength has been attained are displayed as cracks with grey or black color in post-processing figures. One of the main features of this type of model is that there is no need for a pre-existing crack to simulate the crack initiation and propagation. This approach to simulating cracks is similar to a smeared crack model, i.e., no special singular element is used—which has the advantage of leaving the mesh topology untouched. Brittle fractures yielded from the initiation and propagation of cracks in arbitrary and complex paths could be properly simulated without additional processes. Microstructure and defects can be represented by different sets of zones with their own material properties. Hence, it is efficient to simulate the heterogeneous materials. A similar principle has been addressed and applied to modeling concrete damage (Pietruszczak and Xu, 1995; Pearce et al., 2000). With the recent advances in computer performance, an increasing number of researchers have attempted to use a similar principle to solve discontinuous problems through continuum mechanics (Fang and Harrison, 2002; Zhu and Tang, 2004; Ma et al., 2011).

2.2.3. Permeability variation for damaged rockmass

When an element of rock undergoes dilatancy due to the degradation of strength and stiffness, its hydraulic properties will change. Experimental results indicate that dilatancy leads to an increase in permeability. These changes in hydraulic properties can be directly related to either stress or strain (Louis 1974; Stormont and Daemen 1992; Zhu and Wong 1997; Otto Schulze et al., 2001; Tang et al 2002).

Most of the theories regarding stress-induced variations in permeability correspond to the pre-failure phase. During elastic deformation, rock permeability decreases when the rock is compacted and increases when the rock is extended. In order to develop a relation between elastic contraction and permeability, we first employ Equation (2-24) to represent the variation in porosity in response to stress.

$$\phi = \phi_0 - \gamma_t - (\phi_0 - \gamma_t) C_e (\sigma_1 + \sigma_2 + \sigma_3) + \frac{\gamma_t}{3}\left[\exp\left(-\frac{\sigma_1}{E_t}\right) + \exp\left(-\frac{\sigma_2}{E_t}\right) + \exp\left(-\frac{\sigma_3}{E_t}\right)\right] \tag{2-24}$$

where ϕ_0 is the porosity under unstressed conditions, and C_e is the compressibility for the hard fraction of pore volume. The above relationship was derived based on Equation (2-14) (Zhao and Liu 2012).

Once porosity is known, the permeability of a rock matrix can be estimated based on the relationship between porosity and permeability. Based on the analysis of a great number of experimental clay-rock data, Yang and Aplin (2010) pointed out that much of the permeability range observed at a given porosity could be explained by variation in lithology. Using clay content as the quantitative lithology descriptor, they proposed that permeability is a function of porosity and clay content:

$$K = \exp(-69.59 - 26.79F_c + 44.07F_c^{0.5} + (-53.61 - 80.03F_c + 132.78F_c^{0.5}) \cdot \psi + (86.61 + 81.91F_c - 163.61F_c^{0.5}) \cdot \psi^{0.5}) \tag{2-25}$$

where F_c is the clay content, $\psi = \phi/(1-\phi)$. In this study, Equation (2-25) is employed to represent the permeability variation in the rock matrix under an elastic state.

In the post-peak stage, rock elements undergo both instantaneous strength degradation and volumetric expansion. Although many experiments have shown that there is a clear correlation between volumetric dilatancy and the increase in permeability of brittle rocks at the micro-scale, it is generally difficult to characterize small-scale elements accurately and then relate their properties to macroscopic hydraulic properties that are of practical interest (Shao et al., 2005; Jaeger et al., 2007). The degradation is physically manifested as the development of fractures, and this is one of the important concepts addressed in this study. To apply appropriate post-peak hydraulic characteristics, we may find the use of a strain-based formulation for the permeability variation more suitable (Susan et al 2003, Yuan et al 2005; Chen et al., 2007). On the basis of deformation-dependent permeability proposed by Yuan et al (2005), we assume that a damaged rock element may be represented hydraulically as a volume of rock containing one fracture. This representation is shown conceptually in Figure 2-4. Assuming that the fracture is planar and has parallel sides, the aperture (b) of the fractures is given approximately by

$$b \approx \frac{\Delta V}{l^2} \approx \frac{\varepsilon_v V}{\sqrt[3]{V^2}} = \varepsilon_v \sqrt[3]{V} \tag{2-26}$$

where ε_v is the volume strain, ΔV is the volume change of the element due to dilatation, and l is the side length of the element before dilatation.

Once the fracture initiated, its aperture will vary with the stress state. Fracture permeability is largely determined by fracture aperture. A number of empirical expressions exist in the literature

for describing observed relationships between normal stress and fracture closure (that are linearly related to the average fracture aperture) (Goodman 1976; Barton et al., 1985). In this subsection, we employ such a relationship to represent variations in fracture aperture. Considering a fracture to be embedded into a rock sample subject to normal stress σ_n, we again divide fracture space into ''hard'' and ''soft'' parts along the direction normal to the fracture plane. Then, the volumetrically averaged fracture aperture (b) is given by

$$b = b_{0,e} + b_{0,t} \exp\left(-\frac{\sigma_n}{K_{F,t}}\right) \tag{2-27}$$

where $b_{0,e}$ is the fracture aperture of the "hard" part (the value is determined by Equation (2-26)), $b_{0,t}$ is the fracture aperture of "soft" part, and $K_{F,t}$ .is the stiffness of the "soft" part in the fracture. The above equation was derived from the TPHM (Liu et al., 2009). The stress-dependent behavior of the fracture aperture is controlled by the second term at low stress. The expression has been used successfully to match laboratory measurements.

The so-called cubic law gives the flow rate between smooth parallel plates as

$$q = \frac{b^3 \rho_l g}{12\mu_l} \frac{\Delta H}{l} \tag{2-28}$$

where ΔH is the fluid (water) head loss across the two ends. In Equation (2-28), the hydraulic conductivity is given by the term $b^2 \rho_l g / 12\mu_l$. Therefore, incorporating the fracture aperture governed by Equation (2-27), the hydraulic conductivity for a damaged rock element can be expressed as

$$k_d = \frac{b^2 \rho_l g}{12\mu_l} \tag{2-29}$$

In this study, Equation (2-29) is employed to represent the permeability variation for a damaged rock element.

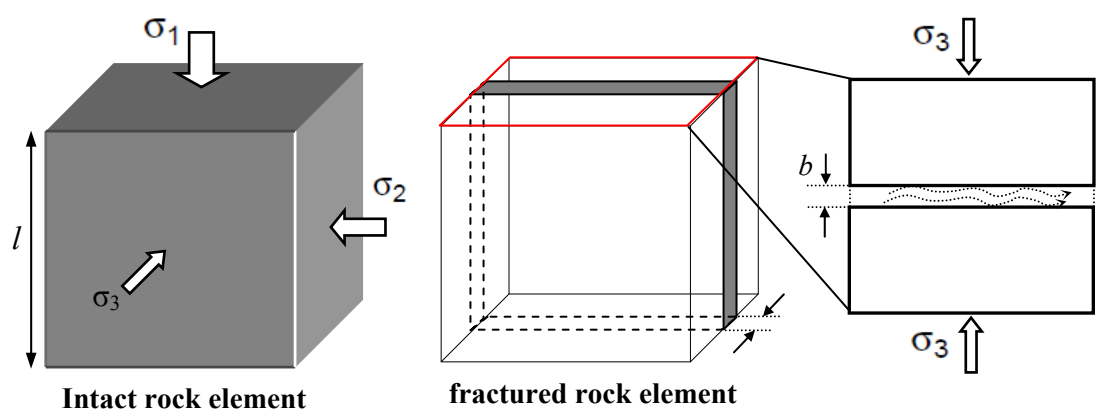

Figure 2-4. Schematic illustration of fracture aperture and permeability of a rock element due to brittle failure.

Here, we need to indicate that only the effect of normal stress on permeability change is incorporated; shear stress is not considered in this model. To facilitate the calculation of permeability variation, the element damage is abstracted to be a planar fracture perpendicular to the minimum principal stress. More studies along this line are needed to more accurately calculate permeability variations for damaged elements.

2.3 Comparison between Modeling Results and Field Data

2.3.1 Mont Terri Mine-by Tests

In many countries, argillaceous formations are being considered as potential host rocks for deep geological disposal of radioactive waste. The Mont Terri rock laboratory started operation in January 1996 as part of the international Mont Terri project. Research there is carried out in an underground facility, located adjacent to the security gallery of the Mont Terri motorway tunnel (Bossart and Thury, 2008). The aim of the project is the geological, hydrogeological, geochemical, and geotechnical characterization of clay formations, specifically Opalinus clay. The Mont Terri Rock Laboratory is located near the town of St. Ursanne, in the Jura Mountains of northwestern Switzerland. The Reconnaissance Gallery (or Security Gallery) was originally constructed as part of the motorway tunnel; the underground laboratory has been developed over the last decade, as shown in Figure 2-5.

In 1997–1998, a mine-by experiment tunnel, known as the ED-B tunnel (as shown in Figure 2-5 and 2-6), was excavated at the Mont Terri Rock Laboratory to assess the issues associated with tunnel excavation. The ED-B tunnel consisted of a 35 m long, 3.6 m diameter circular excavation at a depth of ~270 m. This experiment has provided data from a number of instruments such as piezometers, inclinometers, extensometers and convergence arrays, with excavation advance (Fierz, 1999). The surrounding rock mass of the tunnel was instrumented prior to tunnel driving, allowing for monitoring of the rock-mass response with tunnel advance. The instrumentation records contain unique deformation signatures that provide insight into the mechanical responses of the Opalinus clay to unloading and the formation of an EDZ—a region of micro- and macro-fractured rock mass that forms around the tunnel boundary due to excavation-induced stress redistribution.

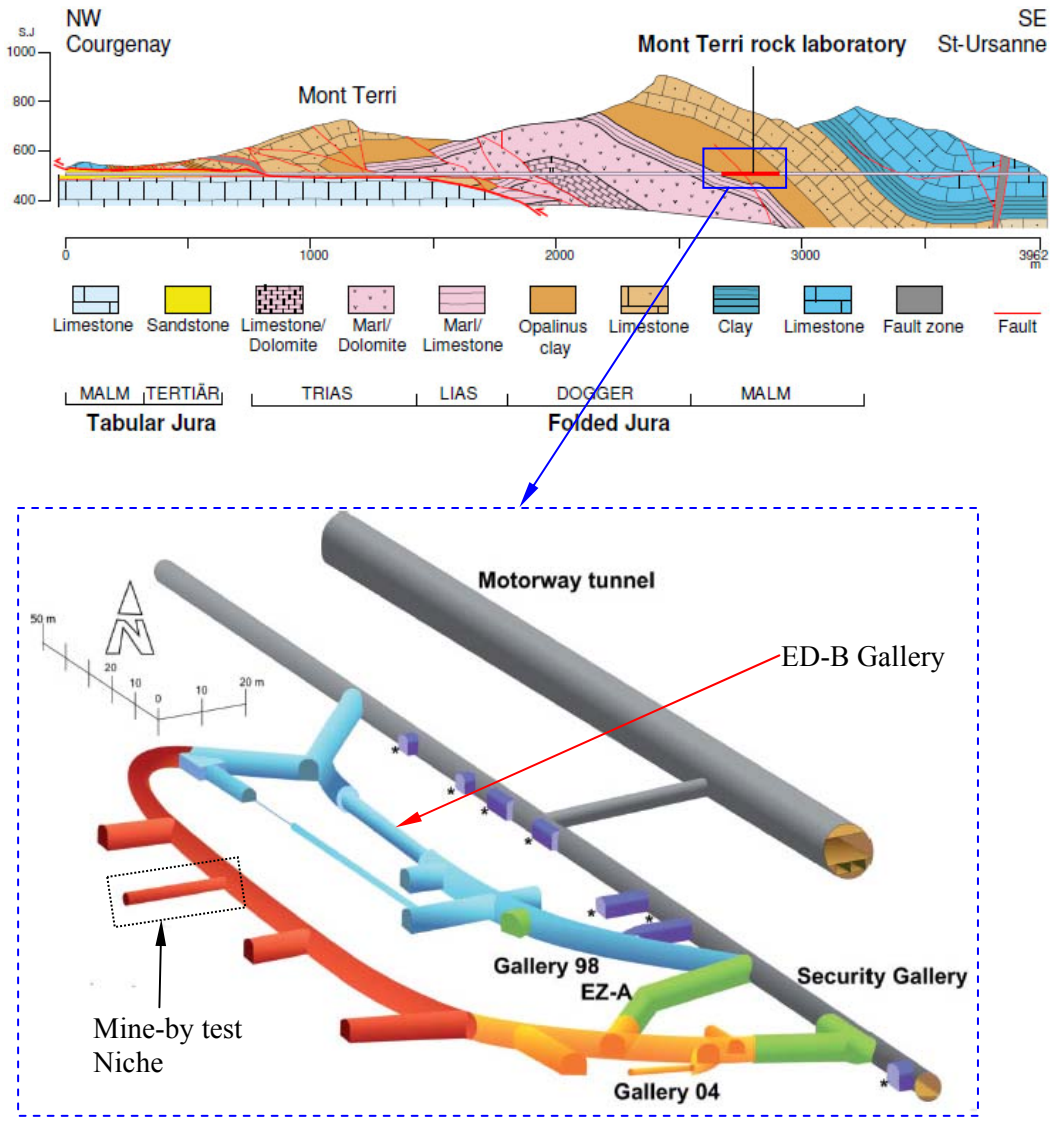

Figure 2-5. Vertical cross section of the Mont Terri anticline along the motorway tunnel (Bossart and Thury, 2008)

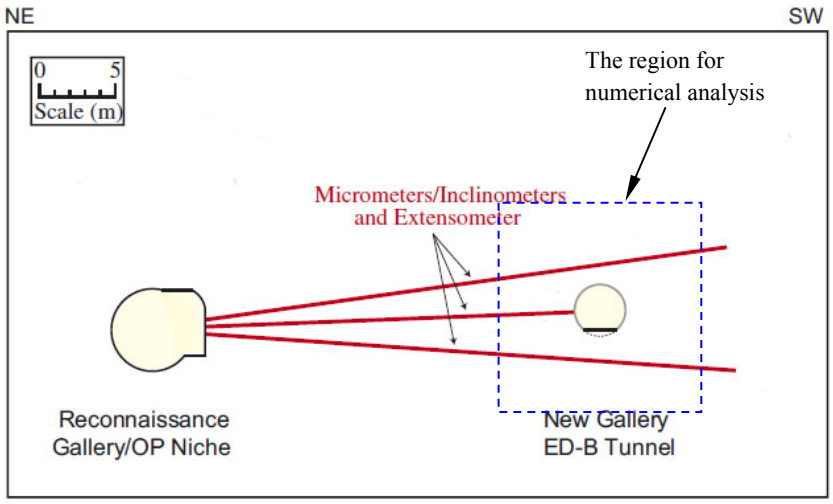

Figure 2-6. Layout of ED-B mine-by experiment instrumentation and tunnel system.

In 2008, it was decided to expand the underground rock laboratory by an additional gallery of 165 m length and 4 niches (the tunnel marked with red color in Figure 2-5). An experiment team took the opportunity to set up the mine-by (MB) experiment (as shown in Figure 2-7). The aims of this experiment accompanying the excavation were to verify or improve data and the methodology of determination for: (1) deformation evolution during excavation with particular emphasis on the tunnel face processes; (2) hydraulic response to excavation works in the excavation near field; (3) influence of different support strategies onto the long-term deformation of the tunnels; (4) far-field hydraulics (HM coupling; total stress changes versus pore-pressure changes); and (5) far-field deformation (reaction of faults, e.g., Main Fault, MI–niche versus the intact rock). The resulting data from the excavation of the MB Niche can now be used to model the niche deformation in order to improve understanding of coupled processes that lead to permanent damage of the rock.

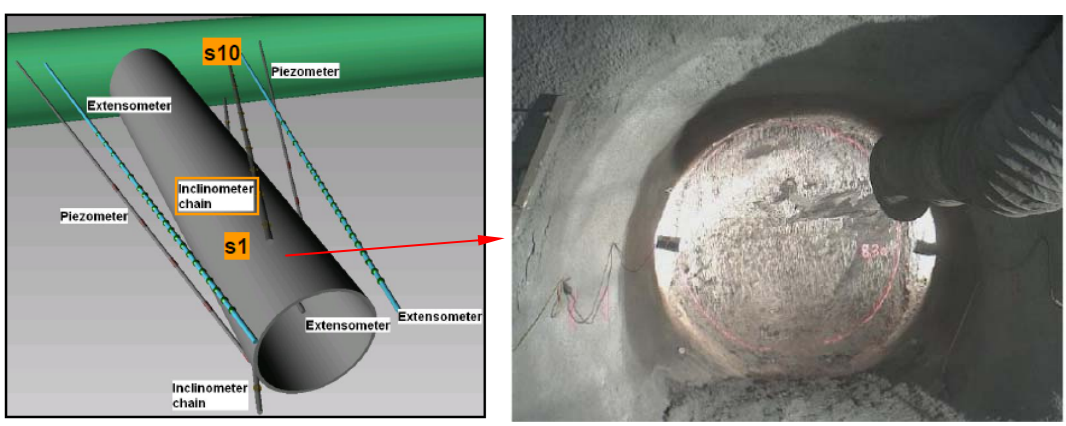

Figure 2-7. Layout of MB experiment Niche and the *in situ* excavating process (Vietor, 2011).

In this study, only the geometry and data from ED-B tunnel are employed to develop 2D numerical models, whose results are compared with the field observations. (More realistic, three-

dimensional (3D) modeling of the mine-by experiment will be performed in the future.) In the following subsections, we describe our work on microscopic crack development and propagation, as well as the macro-mechanical response of the surrounding rock mass around the ED-B tunnel. TOUGH-FLAC3D is used to simulate the short-term rock-mass deformation and EDZ around the circular excavation in the Opalinus clay.

2.3.2. Numerical models

In this study, two different 2D numerical models are developed, called "coarse-grid" and "fine-grid," respectively. These two models have the same geometry and model domain, but differ in that the former has a uniform distribution of mechanical parameters and a relatively coarse grid typical for practical modeling studies. The purpose of developing the coarse-grid model is to evaluate how accurately the TPHM can reproduce macro-mechanical response of surrounding rock mass around ED-B tunnel when deformation is approximately elastic. The purpose of developing the fine-grid model is to evaluate whether the field-scale EDZ evolution can be explicitly captured using a numerical approach that considers the heterogeneity of rock mechanical properties (Section 2.4).

The numerical models contain one circular tunnel, consisting of 16,860 zones and 33,978 grid points for the fine-grid model, and 1,452 zones and 3,002 grid points for the coarse-grid model. The Z-axis is set as vertical in the model, while the horizontal Y- and X-axes are aligned parallel and perpendicular to the tunnel, respectively. The dimensions of the model are 60 m in the X-direction, 1 m in the Y-direction, and 60 m in the Z-direction, respectively. Following the previous studies on tunnels in Opalinus clay (Corkum and Martin, 2007a; Bossart et al., 2002; Popp et al., 2008), the mechanical boundary conditions employed in our study include a total stress of $\sigma_x = 2.2MPa$, $\sigma_y = 4.3MPa$, and $\sigma_z = 6.5MPa$ at the outer boundaries.

The temperature at the tunnel opening and within the rock matrix is assumed to be a constant, 15°C. The underground water table is assumed to be located 100 m above the top boundary of the model, and the rock matrix is initially saturated. A pore-pressure distribution of $P_w = 1000000 + (60 - Z)\rho_w g$ Pa (where Z is height) is directly incorporated into the numerical model. The outer boundary condition is the imposed pressure distribution without change over time.

A constant pressure boundary is imposed at the tunnel wall, as the tunnel is excavated. The corresponding capillary pressure is given by Kelvin's equation incorporating humidity in TOUGH2 (Pruess et al., 1999):

$$P_c = \ln(RH) \cdot \rho_w \frac{RT}{M_W} \tag{2-30}$$

where RH is the relative humidity, ρ_w is the density of water, R is the gas constant, T is the absolute temperature, and M_w is the molecular weight of water. Field test results have shown that the humidity of the air within the tunnel varies with the season (Mayor et al., 2007; Mayer et al., 2007; Shao et al., 2008). In this study, an average relative humidity of 80% in the tunnel is selected.

Opalinus clay is of interest not only as a host formation for radioactive waste repositories, but also as a formation through which new transportation tunnels have been constructed. For this reason, a number of investigations have been published. The mechanical parameter values employed in this study are obtained from laboratory experiments, model calibration, and field research (Corkum and Martin, 2007b; Bock et al., 2010; Zhang et al., 2008; Jobmann et al., 2010), as shown in Table 2-1.

Table 2-1. Physico-mechanical parameters employed in simulations.

Parameter	Value	Unit
Bulk density(ρ_m)	2450	kg/m^3
Initial porosity(ϕ_0)	0.16	
Young's modulus(E_e)	4	GPa
Poisson's ratio(ν)	0.27	
Tensional strength(σ^t)	1.5	MPa
Cohesion(c)	3.6	MPa
Friction angle(φ)	25	°
Clay content (F_c)	60%	
Young's modulus for the soft parts (E_t)	0.002	GPa
γ_t	0.01	
Homogeneity index (m)	3.0	
Degradation index (n_d)	0.0752	

2.3.2. Calibration of the mechanical parameter values

To investigate the stress–strain response and calibrate values for the mechanical parameters (Young's modulus, tensional strength, homogeneity index, and degradation index) that are employed in the following modeling of EDZ around the tunnel in Opalinus clay, we present, in this subsection, comparisons between observed and numerical simulation results on rock specimens in uniaxial and triaxial laboratory tests, in terms of isolated fracture processes and the stress–strain curve associated with fractures. Results demonstrate that the developed approaches and code are effective and promising for more complex applications.

The stress–strain response of geomaterials is required when analyzing underground excavations. The full stress–strain response of brittle rock has been investigated by many authors. Note, however, that inappropriate use of simple linear elastic models may introduce significant errors for this class of problems. Bock (2001) has observed that the stress–strain curves of unconfined compression tests on samples of Opalinus clay have unusually nonlinear stiffness in the low stress region (Corkum and Martin, 2007b). This behavior is illustrated by the unconfined compression test stress–strain curve for a sample of Opalinus clay, shown in Figure 2-8. It can be seen that the deformation behavior of Opalinus clay at low stress levels is characterized by a shallow sloping stress–strain curve near the origin ($0 < \sigma < 2MPa$). The low-stress region is of most interest in the context of unloading around tunnels.

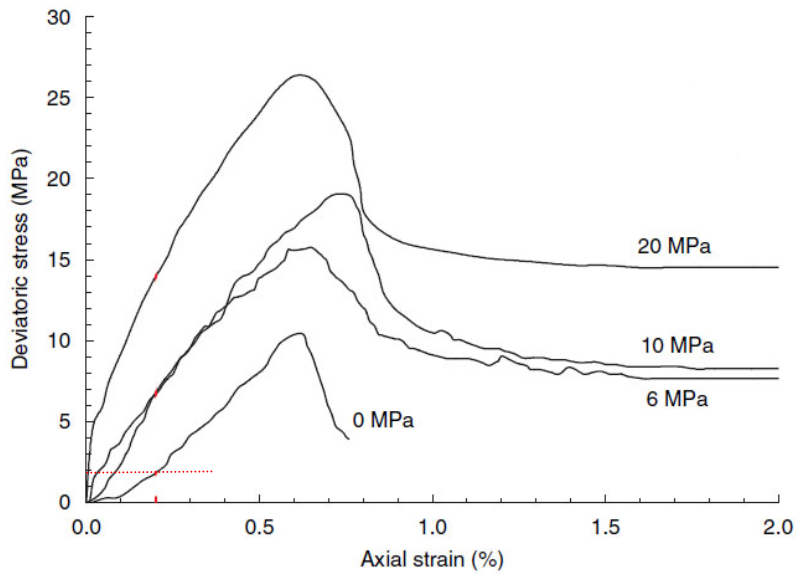

Figure 2-8. Stress–strain plots for a range of σ_3 values (0–20 MPa) (Olalla et al. 1999).

There is a clear need to capture the stress–strain response of Opalinus clay observed in the field and laboratory. To capture the highly nonlinear, low stiffness stress–strain response of Opalinus clay at low stress levels, we employed the newly developed constitutive model, TPHM, to conduct numerical simulation in this study. First, we set up a 2D numerical specimen with a width of 80 mm and height of 160 mm, composed of 40×80 elements that are produced randomly by a computer, according to the Weibull distribution for a given homogeneity index. The homogeneity index, *m*, is a key parameter in this modeling. The analysis and microstructural observations conducted by Wong et al. (2006) indicate that values for the Weibull parameter *m* are greater than 2.0, but fall in the typical range of *m* = 2.0~6.0 (McClintock and Argon, 1966). In addition, a series of numerical models, with different homogeneity indices, had ever been performed to conduct a uniaxial compressive strength test using RFPA code. It is shown that a homogeneity index ranging from 1.2 to 5.0 is common for rock materials (Liu et al., 2004; Tang and Hudson 2010). Therefore, we selected the Weibull parameter *m* = 3.0 to describe the heterogeneous material properties of rock in this study. Each elemental zone has individual

strength properties, bulk modulus, shear modulus, Poisson's ratio, and dilation angle. During the simulation, the bulk and shear moduli of an elemental zone may degrade once the strength criterion is violated, but the other parameters, such as Poisson's ratio and dilation angle, remain constant throughout the entire course of a simulation. In all numerical simulation, axial loading is performed with incremental axial displacements being applied in a sequence of steps to the outer surface of the specimen. To do so, a displacement velocity is specified to both the top and bottom grid points of the specimen. The rock specimen is represented by the modified FLAC Mohr-Coulomb model (a Mohr-Coulomb model based on TPHM).

Experimental results imply that degradation index, n_d, is a mechanical property of the rock, and that different rocks have different values for n_d in Equation (2-22). The value for the degradation index, n_d, of a rock also varies with confining pressure. Thus, laboratory testing is required to determine this parameter for a specific rock. Consolidated undrained triaxial tests have been used to assess the effects of confining stress on the shape of the stress–strain curve. Stress–strain plots for consolidated undrained triaxial tests of Opalinus clay samples at confining stresses of 0, 6, 10, and 20 MPa are shown in Figure 2-8. These tests, conducted by Olalla et al. (1999), were carried out at a strain-rate of 1×10^{-6} per second on Opalinus clay samples. At low confining stress, the low stiffness non-linearity is similar to unconfined compression tests. This behavior diminishes with increased confining stress. The samples show brittle response at all confining stress levels. Based on laboratory test results and Equations (2-21) and (2-22), the degradation index, n_d, is plotted in Figure 2-9 showing a value of n_d for Opalinus clay of about 0.0752.

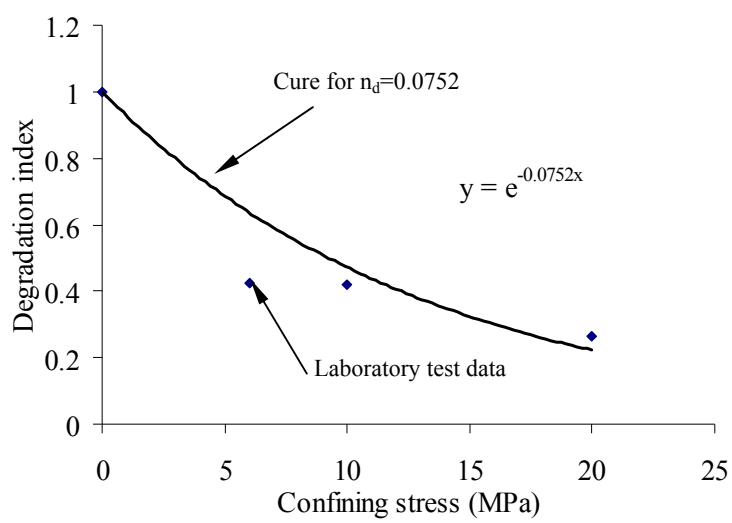

Figure 2-9. Variation in the degradation index for Opalinus Clay with confining stress.

The numerically obtained stress–strain curve is shown in Figure 2-10. The stress–strain curve of Opalinus clay, although it is considered to be a relatively weak rock, is similar to that of brittle rock. It can be seen that the deformation behavior of Opalinus clay at low stress levels is

characterized by a shallow sloping stress–strain curve near the origin ($0 < \sigma < 2MPa$). The corresponding simulated fracture process for uniaxial conditions is shown in Figure 2-11. Two types of plots are given in the simulation results. One is the cumulative failure pattern, which is a plot of all those elements that have failed during the previous loading history; the other is the active failure pattern, which indicates those elements undergoing degradation within the current time step. In the plots shown here, elements showing historical failure are marked by a grey color, and actively failing elements are marked by a dark color.

As indicated in Figure 2-11(a), at a strain level of 2.5%, local failures are initiated at a few sites. With a small increase in axial strain, some new failure sites develop. These, together with some of the previously failed sites, begin to extend in the direction parallel to the major principal stress (Figure 2-11(b)). This results in the stress–strain curve beginning to deviate from linearity, a process that continues up to peak strength, when linkage starts to take place between elongated failure sites (Figure 2-11(c)). Further increases in axial strain lead to a further increase in the elongation and coalescence of the failure sites (Figure 2-11(d)), and the stress–strain curve begins to descend. This is followed by a rapid development in the formation of a macroscopic through-going fracture plane (Figure 2-11(e).

Modeling for the case with a confining stress of 10MPa was also conducted. Figure 2-12 shows the corresponding simulated fracture process of the specimen. It is shown that as the strain increases, more individual failure sites tend to develop, rather than extension of the current failure sites parallel to the major principal stress (as is shown in Figure 2-12(b)). It is only when the diffused failed sites become dense that extensile cracks begin to propagate from failed sites (Figure 2-12(c)), and it is at this stage that the stress–strain curve diverts from linearity (as shown in Figure 2-10). A further increment in axial strain causes these cracks to tend to link with each other (Figure 2-12(d)), corresponding to the peak strength of the specimen. The increase in axial strain enhances the linkage between failed sites to form a macroscopic shear fracture plane, and the stress–strain curve descends rapidly. The shear fracture plane continues to grow (Figure 2-12(e)) until finally, the formation of the macroscopic through-going shear fracture plane is complete.

Geophysical measurements reported and discussed by Corkum (2007a; 2007b) indicate an average isotropic Young's modulus for the rock mass of 4 GPa. As a result, an elastic Young's modulus (E) of 4 GPa was used for all analyses with elasto-plastic constitutive models. The mechanical properties calibrated with the numerical model are summarized in Table 2-1.

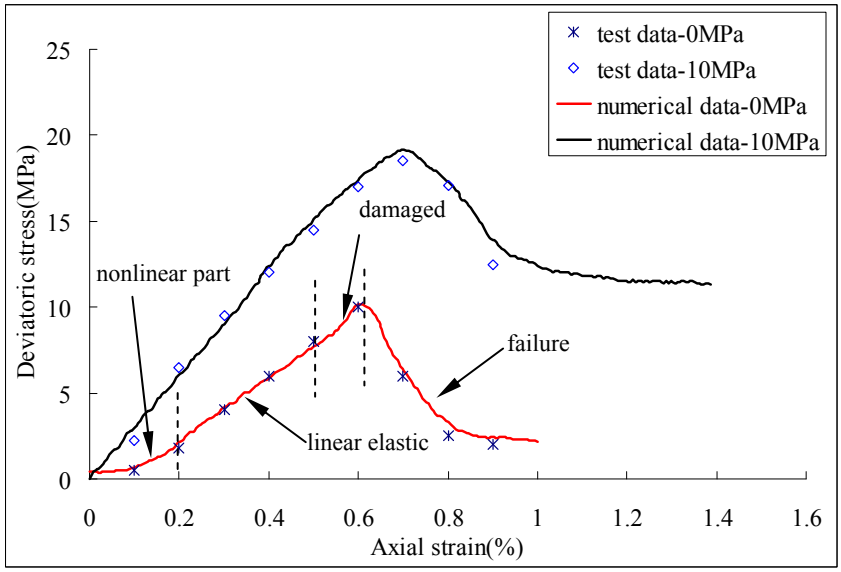

Figure 2-10. Simulated stress–strain curve corresponding to the fracture process displayed in the following Figures 2-11 and 2-12.

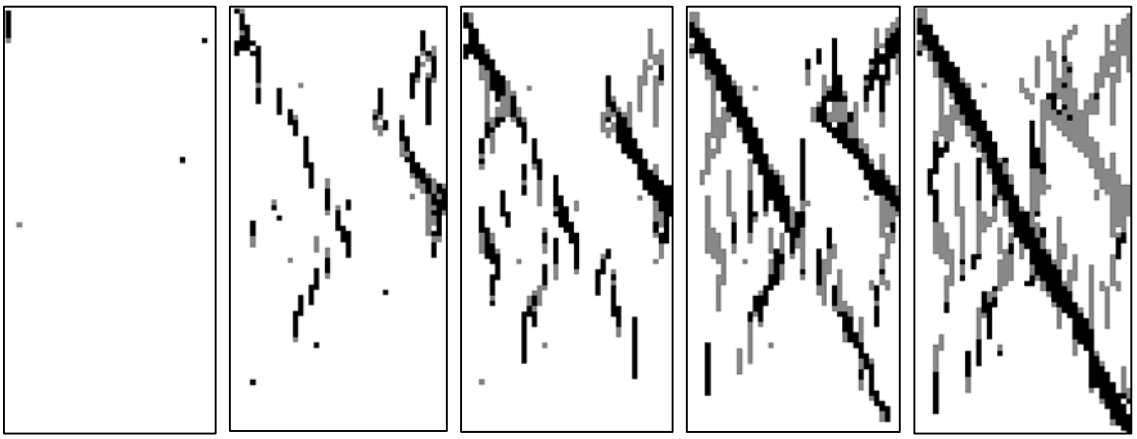

(a) Random initiation of local failures | (b) Extension and coalescence of failed sites | (c) Further development of site coalescence | (d) Formation of macroscopic fractures | (e) Completion of macroscopic fractures

Figure 2-11. Simulated fracture process of a rock specimen under uniaxial compression.

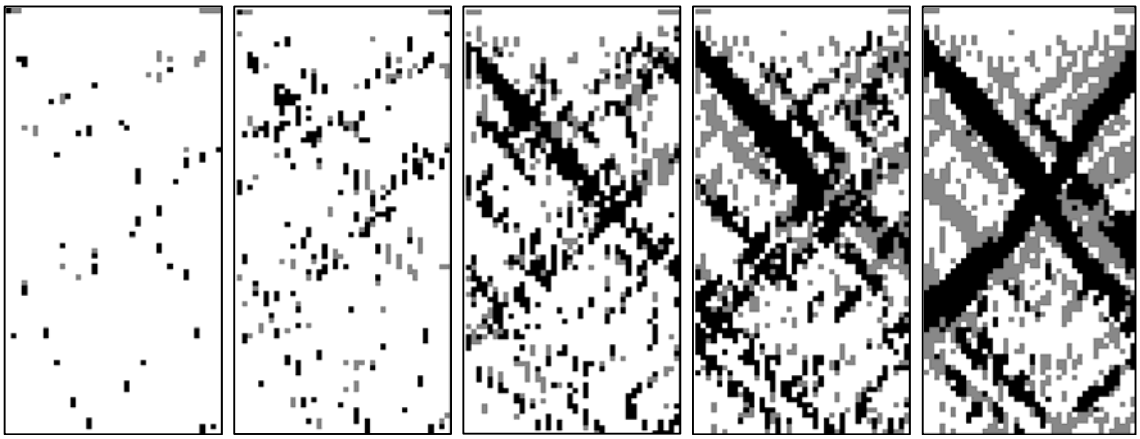

(a) Random initiation of local failures | (b) Extension and coalescence of failed sites | (c) Further development of site coalescence | (d) Formation of macroscopic fractures | (e) Completion of macroscopic fractures

Figure 2-12. Simulated fracture process of a rock specimen subjected to a confining pressure of 10 MPa.

2.3.3. Coarse-grid simulation of displacement around the tunnel opening

The deformation around a tunnel induced by pure excavation was investigated based on elastic analysis using the coarse-grid model. To make a detailed observation on deformation of the rock mass around the tunnel, we select the points located on the red dotted line in the model, as shown in Figure 2-13, as the key points for monitoring displacement variations. Simulated displacement of the rock mass around the tunnel is shown in Figure 2-14, in which the length of the arrow denotes the magnitude of displacement, and the orientation of the arrow denotes the direction of deformation.

Correspondingly, the displacement magnitudes at the key points, shown in Figure 2-13, are illustrated in Figure 2-15. As a comparison, the elastic response described by conventional Hooke's law (SPHM) is also numerically obtained with TOUGH-FLAC3D. Figure 2-15 is a comparison of deformation distribution based on TPHM and SPHM, respectively. It is shown that while the general distribution trend of displacement is similar for both models, the magnitude is clearly different. Numerical results based on TPHM show that there is no evident deformation near the side walls of the tunnel, while points A and C on the roof and floor of the tunnel recorded a maximum of 7.52 mm of inward movement with the maximum deformation in line with the direction of σ_1. The calculated inward displacements based on the TPHM are larger throughout the tunnel section (including the roof and floor) compared to those displacements predicted by SPHM. Based on *in situ* measurement, the roof and floor displacement near points

A and C range from 6.5 to 8.0 mm (Corkum and Martin, 2007a). Clearly, the TPHM model results are much closer to the field observations.

Based on the stress field at Mont Terri and the strength data, only limited plasticity is anticipated around the ED-B tunnel during the initial stage of its excavation (Corkum and Martin, 2007a). Thus, the simulation results regarding deformation are based on elastic analyses only. Considering that the displacement was monitored as a function of time and found to increase with time (Corkum and Martin, 2007a; Bossart and Thury, 2008), we pay attention only to the observed displacement at the beginning of monitoring.

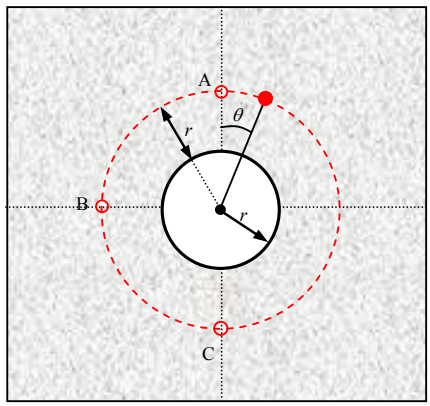

Figure 2-13. Location of key points for monitoring displacement variations around the tunnel.

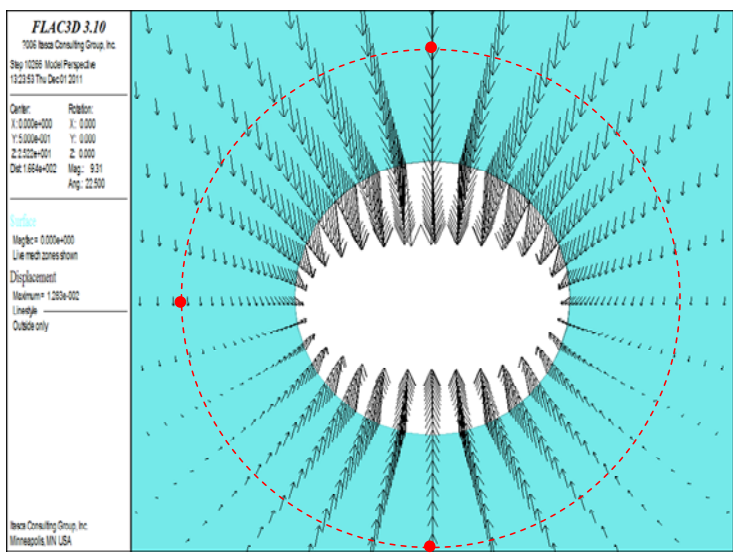

Figure 2-14. Numerically obtained displacement mode based on TPHM.

Assuming that the pre-peak nonlinearity to be represented by the modulus as a function of the confining stress, the distance from the opening wall, or the combined effect of the hydrostatic, confining, and deviatoric stresses, many studies have captured the stress variation and large deformation around underground openings in rock matrix (Corkuma and Martin, 2007a; Lionco

and Assis, 2000; Weng et al., 2008). Our numerical results are consistent with these previous studies, although the constitutive model employed in this study is different. It can be expected that the incorporation of the TPHM in analyzing the behavior of underground excavations affects not only the displacements and stress distributions, but also the size of the damage zone.

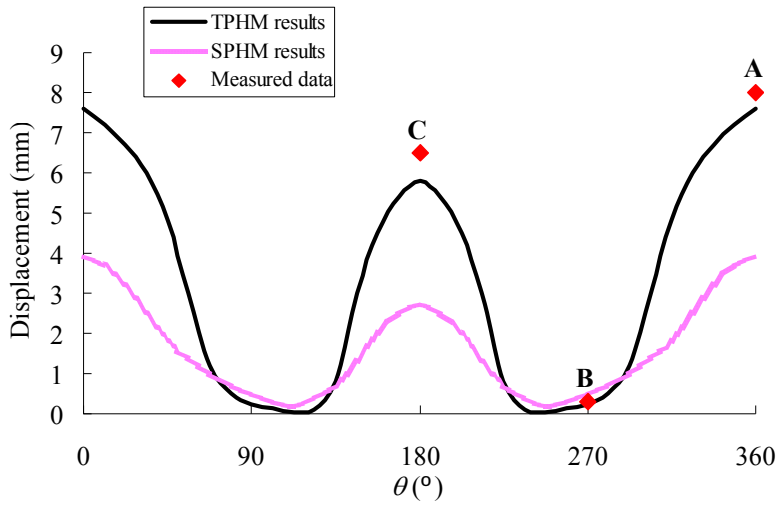

Figure 2-15. Displacement variation (magnitude) at points around the tunnel.

Two important observations can be made from this comparison between model and test results. First, the TPHM model results are significantly different from those obtained from traditional (SPHM) approaches and agree very well with field observations. This highlights the validity of the TPHM and the need to use it for practical applications. Second, laboratory-measured mechanical properties can be used to fairly accurately predict field-scale mechanical deformations, as long as validated constitutive relationships are employed.

2.4 Investigation into EDZ Evolution with the Fine-Grid Model

As previously discussed in Section 2.1, use of fine-grid models, together with incorporation of small-scale heterogeneity, may be able to simulate the fracturing process in a rock mass. A comprehensive review of fine-grid model studies of damage processes (based on RFPA code) was documented in a recent book (Tang and Hudson, 2010). The usefulness of this approach is also presented in Section 2.3.2 of this report. However, most previous studies based on this approach have focused on laboratory-scale problems. In this study, we are interested in (1) how well this approach can capture field-scale fracturing processes with a grid that is reasonably (or feasibly) fine in practice and (2) how effective this approach is in investigating EDZ evolution in a clay repository.

In numerical modeling, mesh (grid) dependency is unavoidable. Many previous studies focused on aspects related to the mesh effect (Fang and Harrison, 2002; Zhu and Tang, 2004). In general, a finer numerical grid will give higher modeling accuracy, but makes the computation more

expensive and time-consuming. In the fine-grid modeling of the EDZ documented in this chapter, we employed a grid block size of 0,05 m for the near-field rock mass around the tunnel.

One simple way of estimating the evolution of the EDZ is to use an elastic stress analysis to determine the induced stresses and compare them with the rock-mass strength. The stress is sufficient to create a very thin failed zone, which may significantly underestimate the size of the actual breakout or failed zone. One method, often used to overcome the limitation of elastic analyses, is to simulate the progressive nature of slabbing and spalling in the EDZ formation (Hajiabdolmajid et al., 2002). This method is used in this study.

Fine-grid simulation in this study takes any previously failed neighboring elements (zones) into consideration. After the initial redistribution of stress, some elements may fail due to stress variation. Thus, at each loading step, the stress redistribution procedure is repeated until all of the elements for which the criteria presented in Equation (2-7) or (2-8) are met. The failed elements release stress, and the released stresses are distributed between the intact neighbors, such that global equilibrium of the model is achieved. As the next loading step is achieved, the broken elements form clusters that grow and coalesce with increasing load. Ultimately, the "critical" cluster of the broken elements is formed at a certain loading step. A brittle fracture initiation and propagation is the end result of the micro damage accumulation process, rather than a single event.

A numerically modeled EDZ evolution around the tunnel is shown in Figure 2-16(a). The results indicate that for the given grid system, the damage zone can be fairly well captured by the numerical model, but not individual fractures. The modeled EDZ evolution in this study is the result of quasi-static response of unloading. Initially, tensile damage of scattered elements is observed in the roof and floor, as is the shear damage of scattered elements at the sidewalls. They are individual and do not coalesce with each other to form a crack. Subsequently, more elements in the roof and floor of the opening undergo damage in tensile mode, which eventually leads to the formation of primary (tensile) cracks in the roof and floor. But the cracks in the roof and floor remain stable and do not propagate any further into the surrounding rock mass. In contrast, scattered damaged elements at the sidewalls gradually coalesce with each other to form macroscopic fractures and continue to propagate into the surrounding rock mass. The shear modes of element damage in the zones of high compression, located at the sidewalls, result in slabbing and crushing. Finally, V-shaped notch zones form at the sidewalls.

The induced damage decreases when moving from the tunnel boundary towards the surrounding rockmass. This is in general agreement with the characterization results reported by Hajiabdolmajid et al. (2002). The arrest of the observed slabbing process, after a new, more stable geometry is reached, can be explained by an increase in confinement (progressive frictional strengthening) coupled with a decrease in the induced damage (plastic strain), and thus

a decrease in cohesion loss, arresting the failure process and the growth of the notch. Beyond the damaged zone, where there is no plastic straining, there is no mobilized frictional strength, and the cohesive strength is not affected.

Due to the heterogeneity of the rock, the pattern of fracturing in the rock around the opening is not totally symmetrical. The variation in the fracture mode is highly sensitive to the interaction between the isolated fractures and the local disorder features of the rock matrix within the high-stress field. As a result, the fracturing path is flexural (instead of straight), and the fracture surface is rough. In reality, there are high-stress and low-strength failure types, which occur in different materials. In a homogeneous material, failure begins at a high-stress site, whereas in a heterogeneous material such as rock, failure may start at the weaker locations because of the presence of pores, micro-fractures, grain boundaries, and so on. For this reason, Fairhurst (1964) introduced the notion of "stress severity," which represents the ratio of the theoretical stress at the moment of failure to the stress that would theoretically be necessary for failure to occur at any given point. Heterogeneity is the main reason for the failure that occurs at locations where the stress is not necessarily the greatest.

The development of fractures is associated with strain softening of the surrounding rock. Localization of micro-cracks and formation of a macroshear plane ("shear band") leads eventually to the full mobilization of the frictional strength after the initial cohesion is lost and reaches its residual value. The process of slabbing around underground openings cannot directly be compared with the shear banding process in laboratory compression tests, even though it also involves a process of cohesion loss and frictional strength mobilization. Actually, the initially local failure within the "shear band" is tension failure, as shown in Figure 2-17. The cohesional component of strength is the predominant strength component at the early stage of brittle failure, with cohesion loss the predominant failure process leading to the observed brittle behavior. The cohesive strength is gradually destroyed by tensile cracking and crack coalescence. The normal stress-dependent frictional strength can only be fully mobilized after the cohesional component of strength is significantly reduced, much damage has accumulated, and rock fragments can move relative to each other in shear. The delay in mobilization of the frictional strength is a characteristic of brittle failure in geomaterials in relatively low-confinement environments, where the brittle fracturing (extensile cracking) is the dominant mode of failure (Hajiabdolmajid et al., 2002).

Figure 2-16(b) shows the stress variation across the opening during EDZ development, which sheds some light on the failure mechanism of the tunnel. Initially, the stress concentrates around the opening adjacent to the tunnel surface. Although the stress distribution at the initial stage is statistically homogeneous on a macroscale, it varies on a microscale due to the microscale heterogeneity in the rock mass. Then, the stress evolution reflects the fracture propagation process. Because of the initiation, propagation, and coalescence of the fracture, a high-stress

concentration is induced, and the high-stress concentration zones continuously move forward into surround rock mass. The stress field concentrates around the newly formed fractures, producing further microfracture damage around and ahead of its tips. This continuous stress concentration leads to another new clustering of microfractures. When large fracture zones develop, highly non-uniform stress distributions also develop, especially when the fracture zone is not immediately stress free.

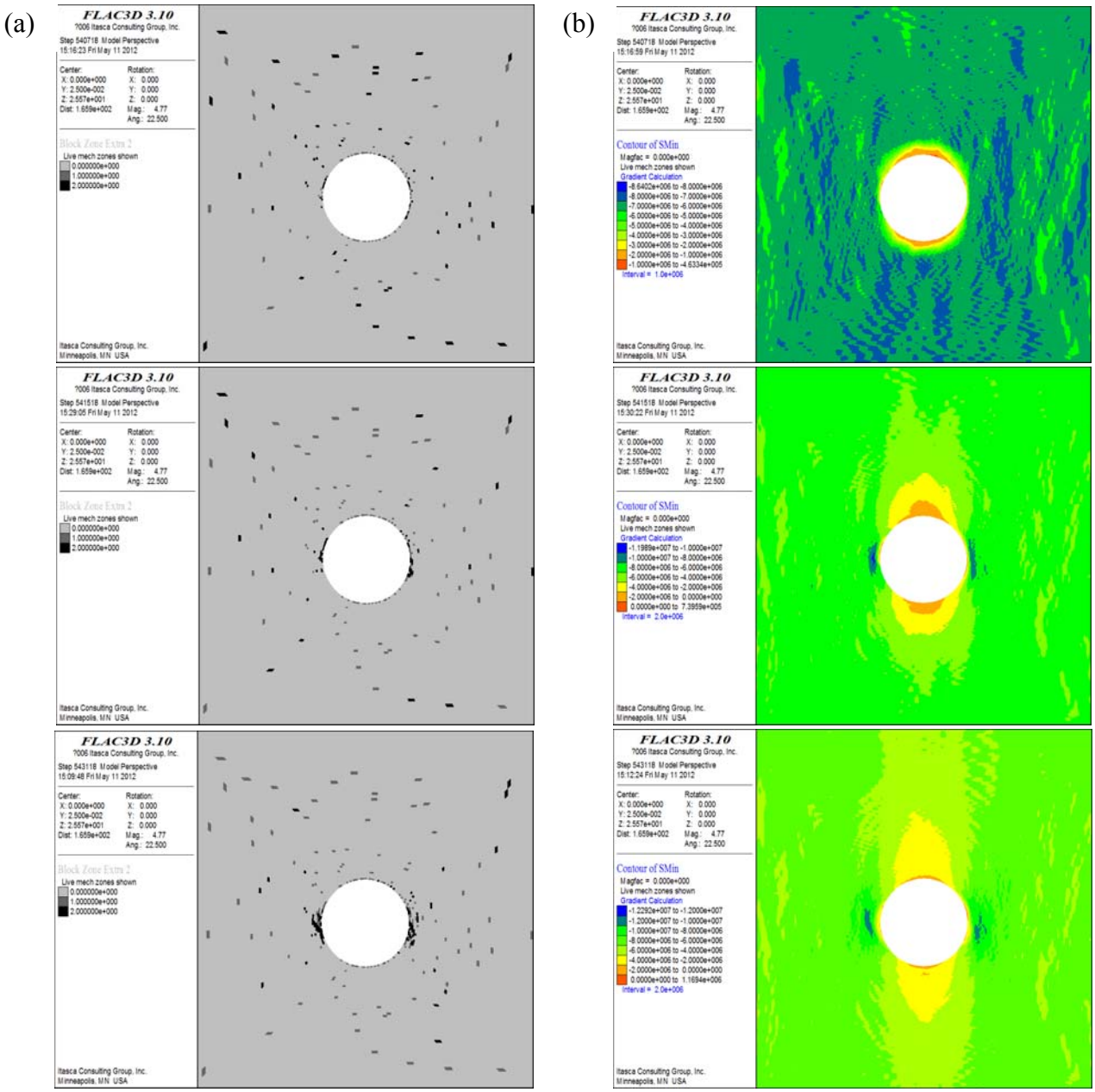

Figure 2-16. Numerically obtained EDZ (plastic zone) evolution: (a) EDZ (left), and (b) minimum principal stress (right).

(a) (b)

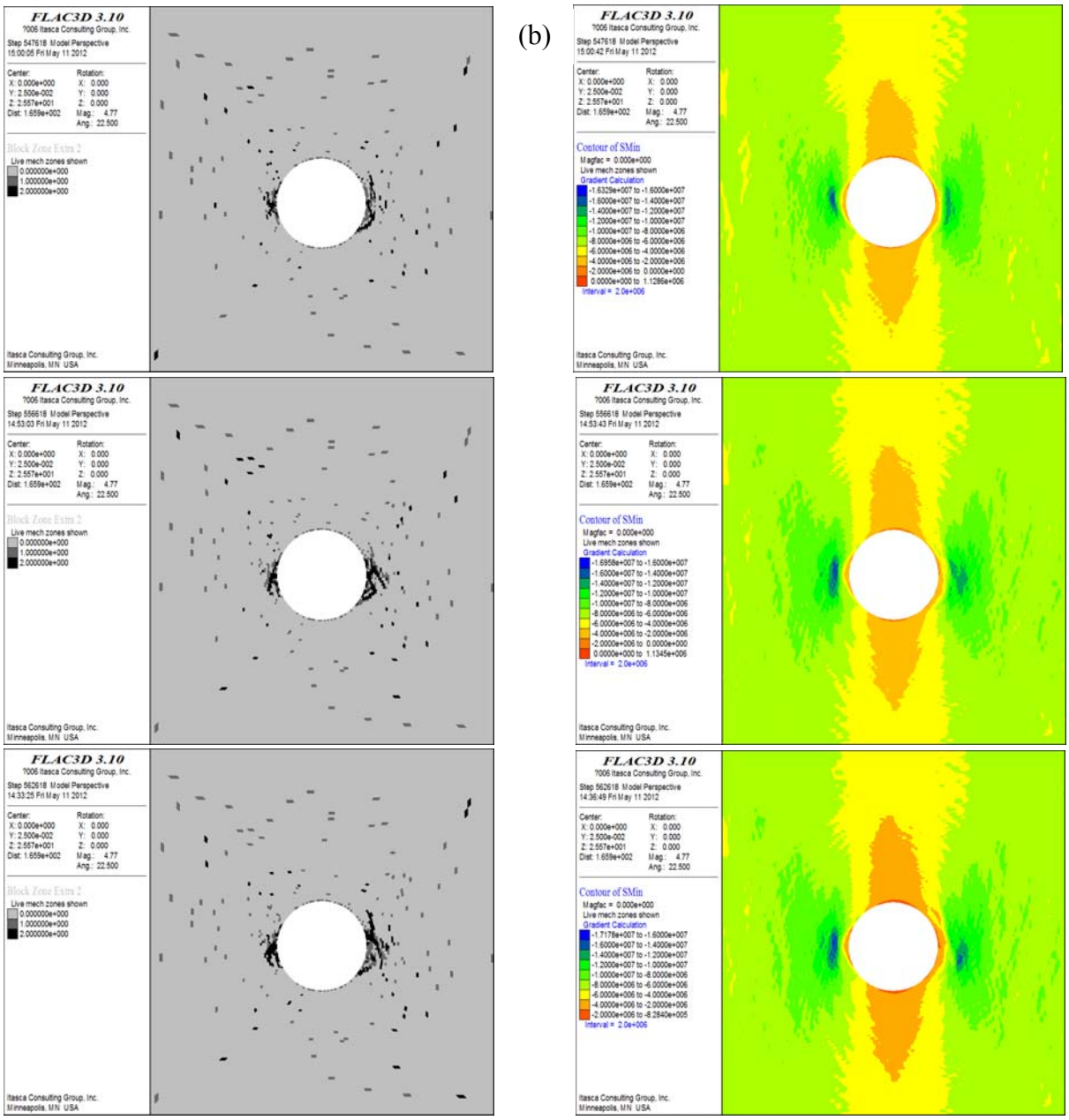

Figure 2-17 (continued). Numerically obtained EDZ (plastic zone) evolution: (a) EDZ (left), and (b) minimum principal stress (right).

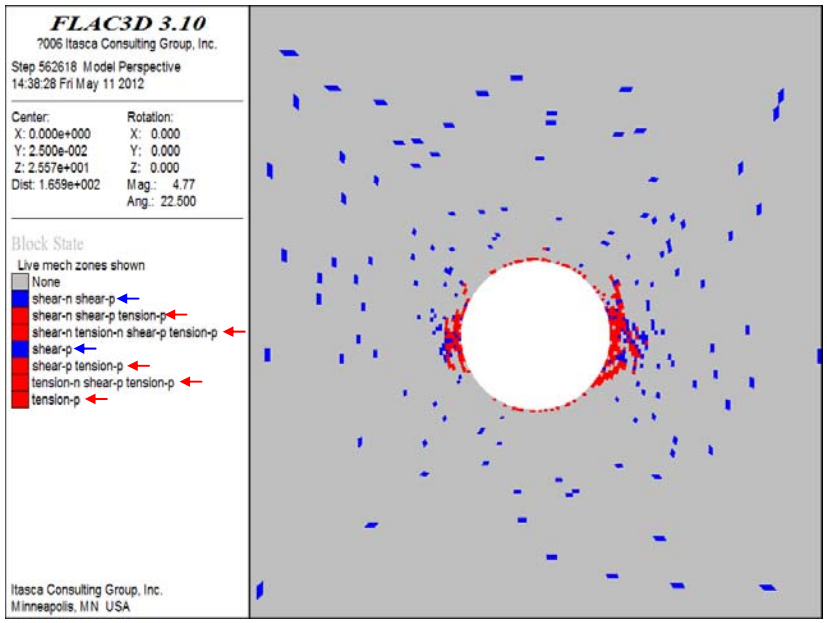

Figure 2-18. Failure type in the EDZ (tension failure marked by RED color and shear failure marked by BLUE color).

The distribution of hydraulic conductivity is shown in Figure 2-18. Correspondingly, a detailed distribution of hydraulic conductivity along the line A-A is shown in Figure 2-19. The permeability increase is induced around the opening, which is controlled by different mechanisms depending on the locations around the opening and on the *in situ* stresses. When the damage around the opening is still sparse and does not coalesce to form a flow path, the permeability increase is predominantly caused by the stress dependency of permeability. With more and more isolated fractures connected with each other, an interconnected fracture network in the zone with an average extent of 1 m within the tunnel sidewalls is formed. This interconnected fracture network is connected to the tunnel. In this context, the zone where the hydraulic conductivity is larger than its initial values is an indicator of the EDZ. Hydraulic conductivities within the EDZ are orders of magnitude higher when compared to those of undisturbed rock. Hydraulic conductivity values are especially high in the EDZ within the tunnel sidewalls, varying between $2.39 \times 10^{-14}\,\mathrm{m}^2$ and $7.45 \times 10^{-13}\,\mathrm{m}^2$, which is consistent with the report based on measured data (Bossart et al., 2002; Bossart et al., 2004).

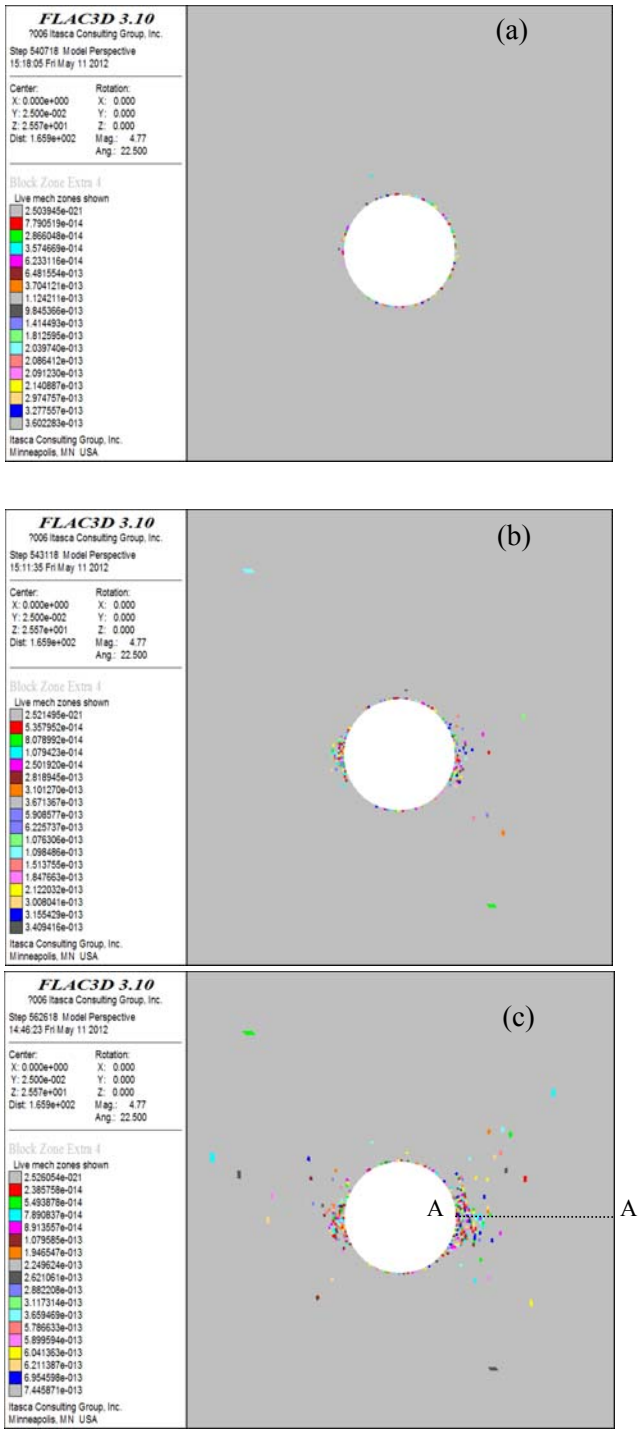

Figure 2-19. Variation in hydraulic conductivity of the surrounding rock mass.

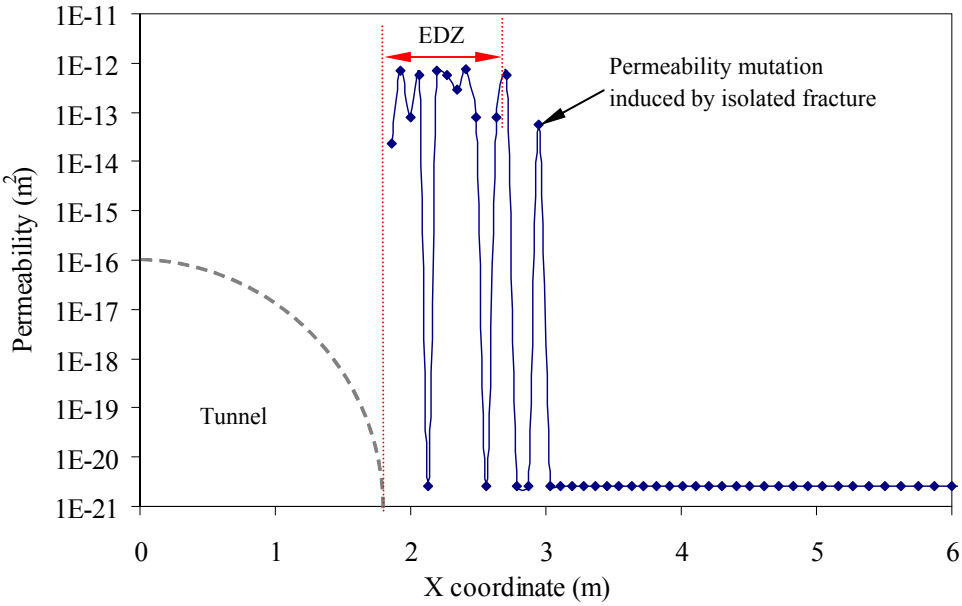

Figure 2-20. Distribution of hydraulic conductivity along the line A-A.

Attempt to predict the maximum depth to which the failure process will propagate is one of the main concerns in the stability of underground opening. Figure 2-20 is a conceptual model of EDZ fractures such as steeply inclined unloading joints and shear fractures on both side walls of the ED-B Gallery (as shown in Figure 2-5) in clay. A simple deviatoric stress criterion has been used to estimate the extent of the EDZ fractures in the gallery walls (Bossart et al., 2004). An EDZ fracture depth of 0.5–1 m in the New Gallery walls was estimated, based on a suggested deviatoric stress value of 8–10 MPa (the value is comparable with the average uniaxial compressive strength of Opalinus clay). Estimated EDZ depth is in good agreement with the inner zone of the EDZ, where an interconnected fracture network is observed in the first meter of the gallery wall (Bossart et al., 2002). In this study, the depth of failure (d_f) was carefully recorded in a progressive, nondestructive manner. To compare the EDZ mode, we also present the results based on SPHM in this section, as shown in Figure 2-21. It is shown that, for both TPHM and SPHM results, tensile damage is associated with cracks that are very narrow and do not penetrate deep into the surrounding rock. By way of contrast, shear damage induces a diffuse crushing over a broad zone. Comparing the EDZ mode based on TPHM and SPHM, we find that the EDZ extension as calculated by TPHM is much larger than that obtained by using the SPHM (as shown in Figure 2-22). The final maximum d_f near sidewalls determined by TPHM is ~1.0 m, while the final maximum d_f is just ~0.5 m for the case based on the SPHM. *In situ* measurement has revealed that the extent of the EDZ is ~1.0 m, but varies between 0.6 and 2.2 m (Schuster et al., 2001; Bossart et al., 2002; Bossart et al., 2004; Martin and Lanyon 2004). Compared with the *in situ* observations, the modeling results based on TPHM model predicts an EDZ mode that is closer to reality than the one predicted by conventional SPHM. As previously mentioned, the non-symmetry in observed notch shapes in the side walls is attributed to excavation effects and the local heterogeneity of rock mass.

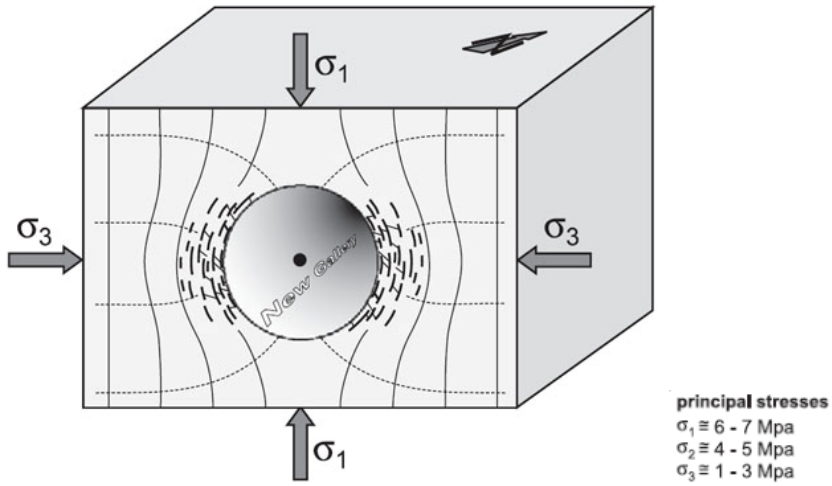

Figure 2-21. Conceptual model of the EDZ and EDZ fractures in the tunnel walls induced by stress redistributions; around New Gallery after excavation (Bossart et al., 2004).

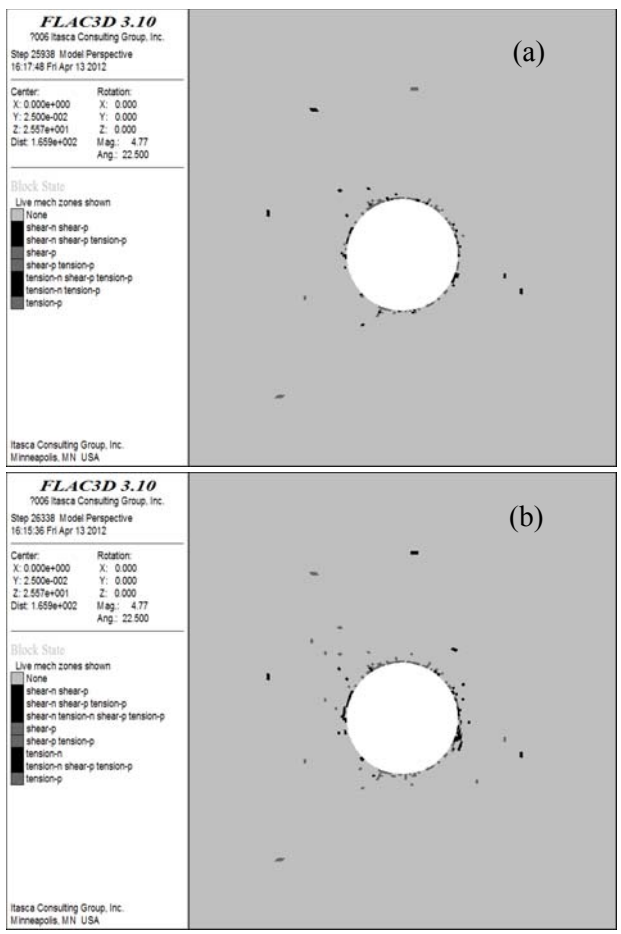

Figure 2-22. Numerically obtained EDZ (plastic zone) evolution based on SPHM.

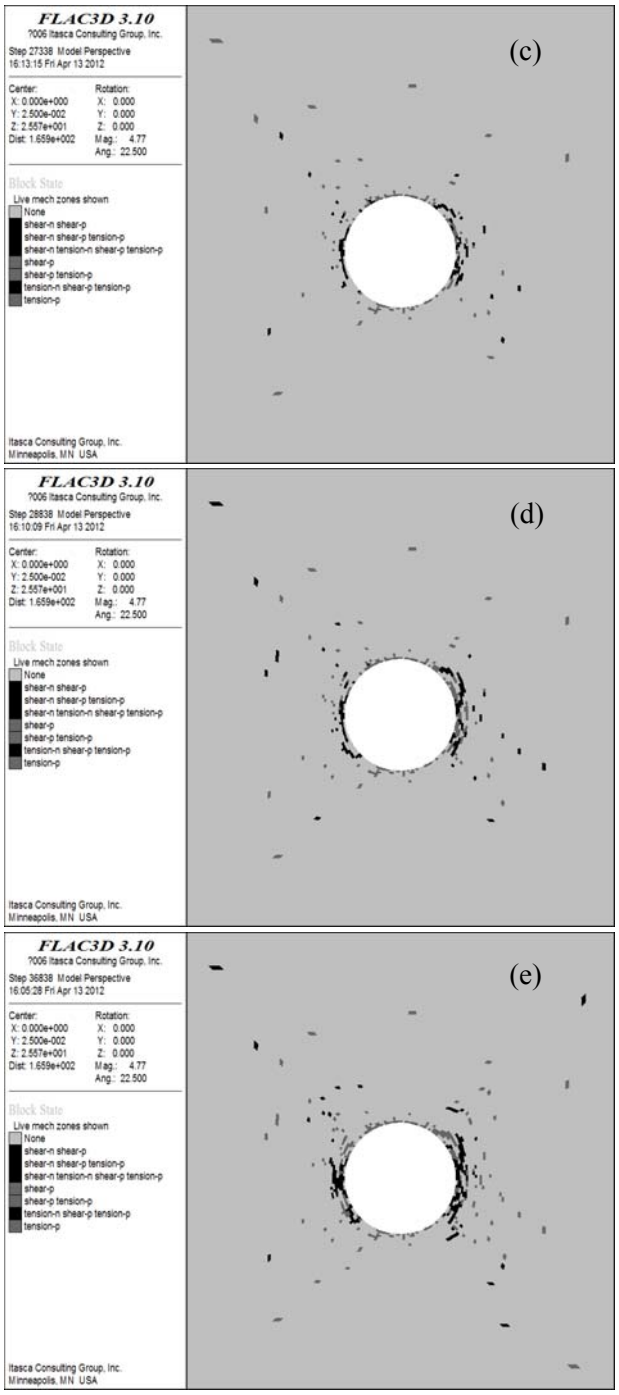

Figure 2-23(continued). Numerically obtained EDZ (plastic zone) evolution based on SPHM.

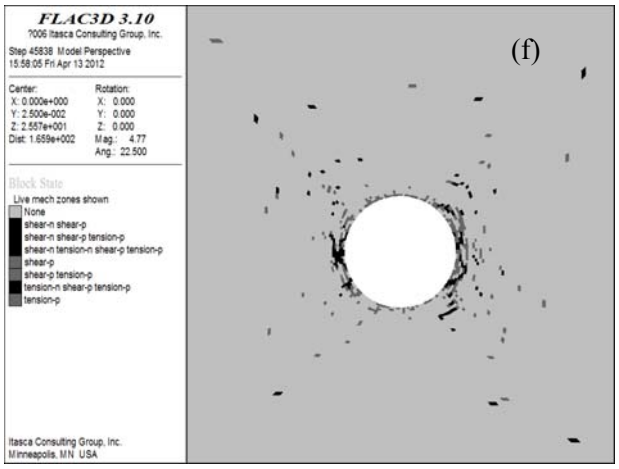

Figure 2-24(continued)**.** Numerically obtained EDZ (plastic zone) evolution based on SPHM.

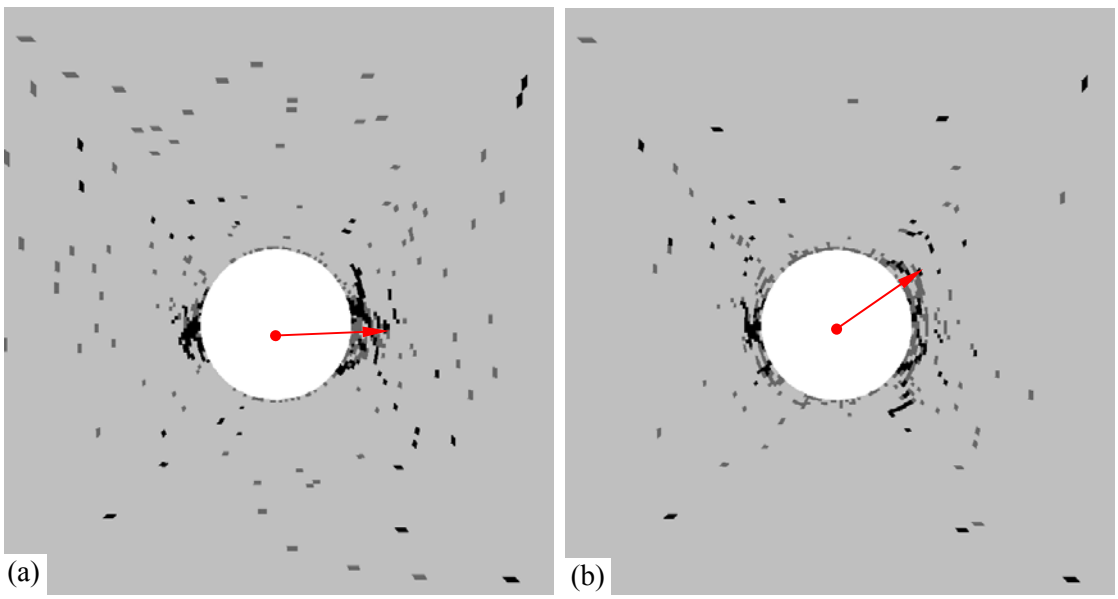

Figure 2-25. The final EDZ mode based on (a) TPHM and (b) SPHM, respectively.

2.5 Discussion of Uncertainties

Knowledge about the EDZ is critically important for constructing a clay repository, because the EDZ may provide pathways for groundwater flow and potentially radionuclide transport of radioactive waste. The EDZ formation and evolution are largely determined by coupled THM processes. However, uncertainties exist in modeling those coupled processes, because they are complex and generally involve a large number of parameters.

Constitutive relationships refer to relationships among hydraulic, mechanical, thermal, and mechanical properties. Accuracy in modeling such coupled processes in a clay/shale repository essentially depends on the validity of the constitutive relationships, because these relationships determine how coupled processes are coupled in a numerical model. While many studies have developed constitutive relationships for brittle rock and unconsolidated soils, such relationships for clay formations are not well established yet in the literature, because clay exhibits complex mechanical-deformation behavior that is generally a mixture of the behavior of brittle rock and soils.

It is obvious that developing reliable constitutive relationships is important for reducing uncertainties involved in modeling the THM processes in a clay repository. This is the major motivation for the R&D activity documented in this chapter. In FY10 and FY11, we developed the THPM to model the nonlinear elastic behavior of clay deformations. In FY12, we implemented the TPHM and associated formulations regarding rock hydraulic/mechanical properties into the TOUGH-FLAC3D code. The usefulness and validity of the TPHM and associated formulations are demonstrated by the consistency between simulation results and field observations from the mine-by tests at the Mont Terri site.

2.6 Concluding Remarks

Coupled THM processes are critical for EDZ formation and evolution in a clay repository. Understanding and establishing the constitutive relationships involved in these coupled processes are the key elements in modeling these processes. This chapter has documented our progress in implementing and validating the new constitutive relationships (TPHM). Based on this study, the following specific conclusions can be made:

(1) The TPHM and associated formulations regarding rock hydraulic/mechanical properties were implemented into TOUGH-FLAC3D code. This provides the capability for modeling the coupled processes with newly developed constitutive relationships. While TPHM was developed for elastic processes, some features for describing property degradation due to damage and stress-dependence of hydraulic properties of fractures were also considered in the implementation, although this consideration is preliminary at this stage.

(2) The usefulness and validity of the TPHM and associated formulations are demonstrated by the consistency between simulation results and field observations from the mine-by tests at the Mont Terri site. The simulation results, which are sensitive to the constitutive relationships used in the model, capture both the observed displacements and the size of the damage zone, whereas the approach based on the conventional Hooke's law significantly underestimates both. The comparison between simulated and observed results also indicates that laboratory-measured mechanical properties can be used to

fairly accurately predict field-scale mechanical deformations, as long as valid constitutive relationships are employed.

(3) A fine-grid numerical approach, together with an explicit incorporation of the small-scale heterogeneity of mechanical properties, is able to capture the overall behavior of EDZ, as demonstrated by the consistency between the simulated and the observed EDZ size. This approach can be used for investigating the EDZ formation and its evolution. The simulations show that the fracturing process in EDZ is caused by the high deviatoric stresses during unloading process (excavation), and that the cohesive strength is gradually destroyed by tensile cracking and crack coalescence. They also indicate that there exist two important mechanisms controlling the permeability variation around the underground opening: (1) the stress dependency of permeability, which is dominant before the formation of the damage zone around the opening, and (2) the damage-induced permeability increase.

3. Development of a Discrete Fracture Network (DFN) Approach for Fractures in Argillaceous Rock

3.1 Overview of Thermal-Hydrological-Mechanical (THM) Coupling and Fractures in Argillaceous Rock

Geologic disposal of radioactive waste has been investigated for a variety of geologic environments. Isolation of the waste generally relies on a low-flow environment around the waste and in many cases this low-flow environment is supported by the low permeability of rock in which the waste is deposited. Argillaceous rock has been identified by several countries investigating radioactive waste disposal as a favorable rock type because of its low rock matrix permeability and its limited fracturing, which typically does not result in conductive fracture networks (Mazurek et al., 2003).

Geomechanical processes are known to play an important role in hydrogeological behavior (Neuzil, 2003). Linkage between mechanics and hydrogeology occurs in two fundamental ways through feedback between (1) rock strain, the geometry of pores and fractures, and their permeability and porosity; and (2) fluid pressure and rock mechanical stress. Although there have been great strides in the capability to compute problems involving hydro-mechanical coupling (e.g. Rutqvist et al., 2002), the problem of fracture initiation and propagation, and its impact on fluid flow processes, remains a major difficulty. These problems are of particular importance for low-permeability, mechanically weak rock such as clays and shales because fractures can be relatively transient as a result of fracture self-sealing processes (Bastiaens et al. 2007). Such issues are important, e.g., for geo-environmental issues related to nuclear waste disposal (Bossart et al., 2004) and geologic carbon sequestration (Chiaramonte et al., 2008).

While argillaceous rock typically acts as a flow barrier, under certain conditions significant and potentially conductive fractures may be present. Two types of fracture formation are possible under distinctly different conditions. The first type of fracturing is a result of strong differential stress that occurs in the vicinity of a waste emplacement drift through argillaceous rock (Bossart et al., 2004). The differential stress is induced by the presence of the excavation, which introduces a stress at the drift boundary that in general sharply contrasts with the natural stress present throughout the rock caused by gravitational loading and tectonic forces. The drift also is affected by repository ventilation during construction and operational phases leading to dryout of the near-drift region of the rock. Argillaceous rock often displays volumetric shrinkage in response to drying and volumetric swelling in response to wetting (Tsang et al. 2010). This behavior imposes stress gradients in the vicinity of the drift that can contribute to fracturing. The second type of fracturing has been observed in natural argillaceous rock as a result of hydraulic overpressure. Because of the low-permeability of argillaceous rock, pressure changes can only be transmitted very slowly. As a result, many argillaceous rock systems are not in pressure equilibrium (Gonçalvès et al., 2004). Overpressure conditions can cause hydraulic fracturing if

the fluid pressure leads to tensile effective stresses that exceed the tensile strength of the material (Cosgrove, 2001).

In both types of fracturing, argillaceous rock shows the ability to self-seal, and perhaps self-heal once the conditions that led to fracturing abate (Bock et al., 2010; Cosgrove, 2001). Self-sealing refers to fracture closure such that the rock hydrogeologic properties return to levels representative of an unfractured rock. Self-sealing has been directly observed in fractures near excavations in argillaceous rock. In natural rock, fracturing is not commonly found, which is consistent with the general characteristic of argillaceous rock acting as a fluid flow barrier. However, in some cases evidence of hydraulic fracturing has been preserved by infilling materials, even if the fractures are no longer preferential pathways. It appears that fracturing can occur in argillaceous rock over limited time periods in which fractures are active flow pathways. Unless fracture infilling materials are present, self-sealing tends to obscure evidence of previous fracturing.

The first part of this report covers a computational method applicable to 3D discrete fracture networks (DFN). Fractures are considered as discrete features that interact with a porous rock matrix. Fracture configurations are mapped onto an unstructured, 3D Voronoi grid, which is based on a random set of spatial points. DFN are represented by the connections of the edge of a Voronoi cell. This methodology has the advantages that fractures can be more easily introduced in response to coupled hydro-mechanical processes, and that it generally eliminates several potential issues associated with the geometry of DFN and numerical gridding. The multi-phase fluid flow numerical simulator TOUGH2 is used to simulate flow and transport through discrete fractures in a porous rock. Fracture cells are introduced at the boundaries of Voronoi cells so that flow and transport through a discrete fracture network interacting with a permeable rock matrix can be studied. Analytical solutions of saturated flow and transport through a single fracture are also developed to verify the numerical results.

To explore the hydrological behavior of such a fracture representation, we first investigate simple single-fracture systems in two-dimensional domains to demonstrate the ability of the numerical approach to match analytical solutions. These solutions are valid for simple fractures that are straight and connected across an entire domain. Solutions for the case of flow parallel to the fracture already exist. Using similar methods, analytical solutions have been extended to included flow fields that are not parallel to the fracture. In other words, the solutions also include the effects of matrix cross-flow. We then investigate irregular fractures discussed above that are of interest for conducting coupled hydro-mechanical processes in which fractures can develop or self-seal as a result of mechanical and hydrological conditions. The results for irregular fractures are compared with equivalent linear fracture geometries for both parallel-flow and cross-flow conditions.

The second part of this report describes a newly developed coupling between a mechanical-damage model and TOUGH2. This allows computation of fracture evolution as well as flow and transport through the fractured porous rock accounting for dynamically changing thermal-hydrological-mechanical (THM) conditions. Elastic response and fracture development is modeled by the mechanical-damage model, based on the rigid-body-spring network (RBSN). Spring constants are related to elastic rock-mechanical properties, and fracture initiation is determined using a classical brittle approach. Both models share the same geometrical information from a 3D Voronoi grid and associated nodes, where the scalar field quantities (e.g., temperature, pressure, and saturation) and the generalized displacements are obtained by TOUGH2 and RBSN, respectively. Fractures propagate along Voronoi cell boundaries as induced stresses evolve and exceed the material strength. In particular, an example application to shrinkage cracking demonstrates the modeling of moisture-driven fracture-propagation problems.

3.2 Discrete Fracture and Dual-Permeability Models for Hydrogeologic Processes

There are a variety of methods that have been developed to model hydrogeologic processes in fractured rock (Lichtner 2000; National Research Council, 1996). One distinction between modeling methods is whether or not the model includes the effects of a porous matrix. The work developed here for argillaceous rock includes the effects of flow and transport in fracture and the rock matrix. Given the interaction of fractures and matrix for flow and transport, the main modeling methods available are the dual-permeability method and the discrete fracture method.

A dual-permeability model represents the fractures and matrix as distinct, overlapping continua that both occupy the same spatial domain (Barenblatt et al., 1960; Duguid and Lee, 1977). The conservation equations for flow and transport in each continuum are connected through a spatially-distributed interaction term based on local values of the relevant state variables in each continuum.

A discrete fracture model treats fractures as individual objects embedded in the rock matrix and have hydrogeologic properties that are distinct from the rock matrix. An interconnected set of discrete fractures is called a discrete fracture network. A fracture network is often approximated as a fracture continuum in hydrogeologic problems that have a high fracture density. A discrete fracture modeling approach is used in this report. This is considered appropriate for cases in which fracturing is sparse (Lichtner, 2000), particularly where a fracture network is characterized by significant localized anisotropy and preferred channeling (Moinfar et al, 2011).

Two examples are given here to illustrate some differences between a discrete fracture representation and a fracture continuum. The first example illustrates how a single-fracture with porous matrix system differs from a dual-permeability representation, as shown in Figure 3-1. In this case, a rock fracture is imbedded in a low-permeability rock matrix. The pressure gradient

across the domain has x and y components, leading to corresponding components of the flow velocity in the fractures and matrix.

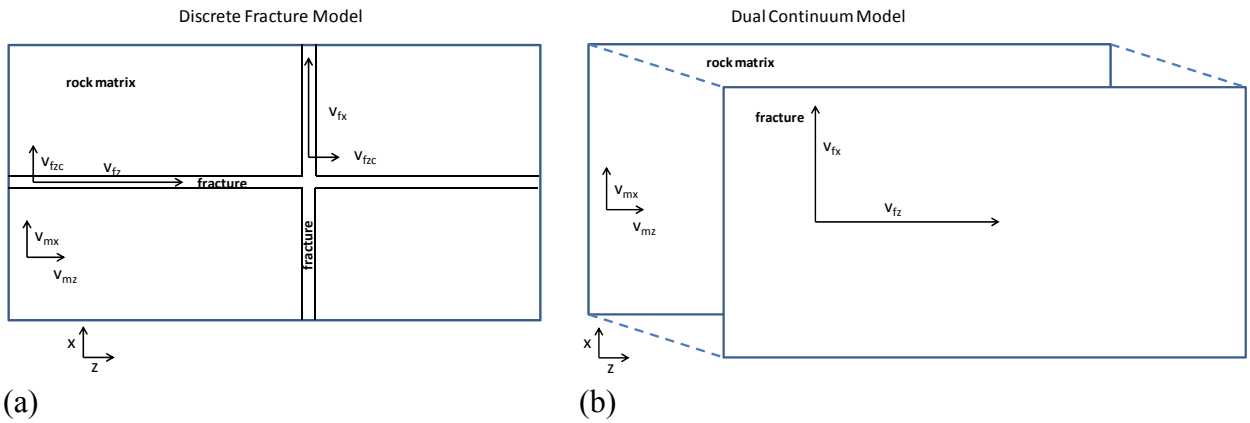

(a) (b)

Figure 3-1. Model representations of a two-dimensional fracture-matrix system. (a) discrete fracture model; (b) dual continuum model.

For the discrete fracture model shown in Figure 3-1(a), there is matrix flow (v_{mz} and v_{mx}), fracture flow (v_{fz} and v_{fx}), and fracture-matrix cross flow (v_{fzc} and v_{fxc}). As is apparent in Figure 3-1(a), the geometry of fracture networks can isolate matrix regions such that matrix flow requires fracture-matrix cross flow. Even if such isolation is not absolute, the presence of fractures that obstruct matrix flow pathways will tend to enhance cross flow. The dual-permeability model in Figure 3-1(b) is more abstract, having overlapping fracture and matrix continua that occupy each point in the domain. For this model, cross flow will be limited, because the parallel structure of the two continua can accommodate matrix flow without necessarily requiring cross flow. Thus, it may be difficult to represent the process of cross-flow exchange between fractures and rock matrix in a dual-permeability model.

In some cases, the response of a fracture system may not be consistent with a dual-permeability representation. As a second example, consider a single numerical grid element in a dual-permeability model that represents 129 parallel fractures as an effective fracture continuum. Assume the flow is parallel to the fractures but that one fracture has an aperture two times larger than the other 128 fractures. For individual, parallel-plane-type fractures, flow is proportional to the square of the fracture aperture. Thus, about 97% of the flow is carried by the smaller fractures. If the transport processes in each fracture are assumed to be independent, with flow only in the fracture, then an analytical solution (e.g., Tang et al., 1981) may be applied to compute the transport response. The mass arrival rate normalized by the total mass released for such a system of fractures was computed, as shown in Figure 3-2. In this case, there was an instantaneous release of solute mass in each fracture; solute mass arrival occurs at a point 4 m downstream from the release position. The mass released in each fracture is in proportion to the flow rate in each fracture. The first peak in solute mass arrival rate at about 9 days is transmitted

through the large fracture. Solute mass arrivals decrease from this peak until about 68 days, when the mass-arrival rate begins to rise again, leading to a secondary peak in the mass arrival rate at about 220 days. This secondary peak is caused by transport through the smaller fractures. Although the highest solute mass arrival rate occurs at the first peak, the solute mass represented by the first peak is only 3% of the total solute mass; 97% of the solute mass arrives in the second peak. Because of the predominance of small fractures for flow behavior, average fracture properties used for the dual–continuum model result in a transport response similar to the small fractures in the discrete-fracture model, completely missing the transport response of the large fracture. Typically, the individual fracture information used for the discrete fracture model is not available; however, including individual fracture variability in a discrete fracture model allows for transport responses that may be difficult to represent in a dual-permeability model using average fracture properties. More complex multiple-continuum models that divide a fracture system into multiple overlapping continua have been developed (e.g., Wu at al., 2004) and could potentially produce multiple-mode transport responses as in Figure 3-2. However, these continuum approaches become increasingly abstract because the ways in which the different continua interact are difficult to relate to physical reality for flow and transport processes.

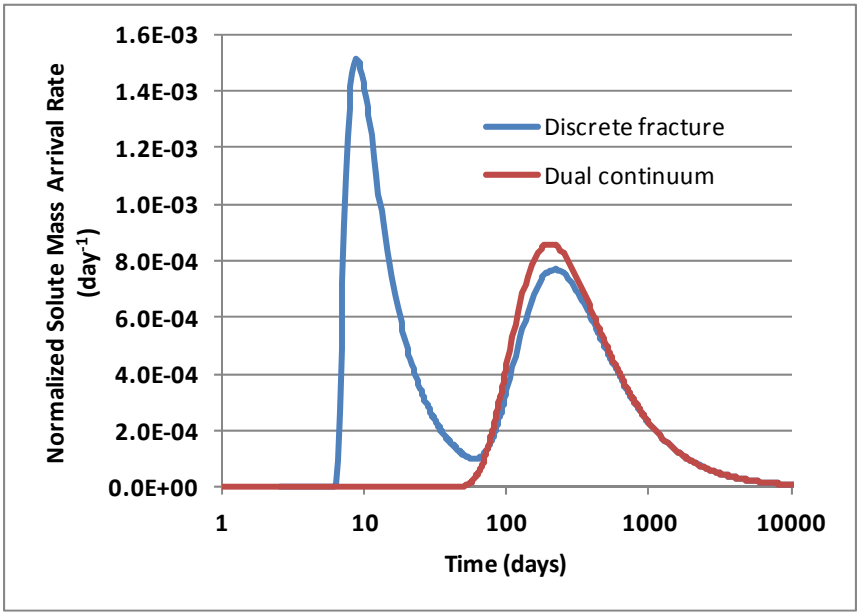

Figure 3-2. Solute mass arrival rates from discrete-fracture and dual-permeability models.

3.3 Representing Discrete Fractures and Rock Matrix- Numerical Gridding Strategy

3.3.1 Voronoi Tessellation for Irregular Geometries

Voronoi discretization is an effective approach to partition a computational domain containing a set of nodal points into a set of spatial regions or cells, where each cell is associated with an individual nodal point. In this study, the procedure of Voronoi discretization starts with nodal

point insertion. Nodal points are sequentially placed into the domain by a pseudo-random number generator. The use of a random point set simplifies mesh generation and increases flexibility in the model geometry. Two inputs, the dimensions of the computational domain and a minimum allowable distance l_m between nodes, are prescribed to control the mesh size. The domain is eventually saturated with a set of points with the l_m constraint. The condition of point saturation is important for controlling the mesh gradation (i.e., the nodal density) by setting l_m, as a function of the nodal coordinates.

The Voronoi tessellation of a point set can be generated by various approaches. For the work presented here, the Delaunay tessellation is first generated using the concept of a supertriangle (or supertetrahedron) (Sloan, 1987; Taniguchi et al., 2002), after which the dual Voronoi tessellation is constructed. The Delaunay tessellation of the point set is defined by the set of triangles whose circumcircle do not include any point as illustrated in Figure 3-3 for a 2D case. The defining characteristic of the Voronoi cell is that all locations within the cell lie closer to the associated nodal point p_i than to any other nodal point p_j. Each edge ij of a Delaunay tetrahedron corresponds to a Voronoi cell boundary between neighboring points p_i and p_j. The circumcenter for a given tetrahedron defines a Voronoi vertex. Figure 3-4 shows the process of generating a 3D L-shape domain. More details about Voronoi discretization techniques can be found in Asahina and Bolander (2011).

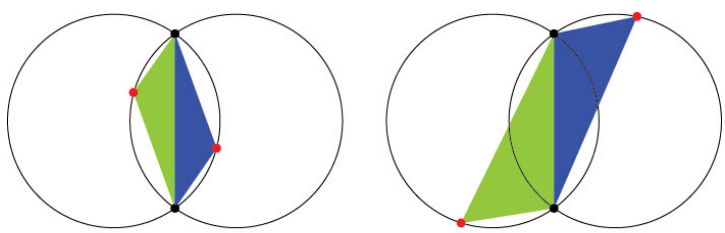

(a) (b)

Figure 3-3. Selection of Delaunay tessellation: (a) a node within a triangle circumcircle (not accepted); and (b) no node within a triangle circumsphere (accepted).

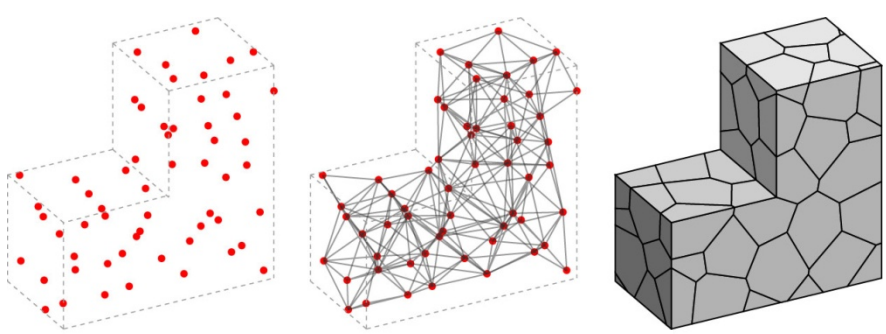

(a) (b) (c)

Figure 3-4. Mesh construction sequence: (a) nodal point set; (b) Delaunay tessellation; and (c) Voronoi diagram.

3.3.2 Gridding and Nodal Assignment Method to Incorporate Discrete Fractures in Rock Matrix

In this study, fractures are considered as discrete features that interact with a porous rock matrix. An irregular Voronoi grid is used to represent the rock matrix as a basic material structure. Existing or newly generated fractures are directly mapped onto such a Voronoi grid. Figure 3-5 shows a discrete fracture explicitly represented by a series of Voronoi cell boundaries (i.e., edges of a polygon). Fracture geometric data (e.g., fracture orientation, length, width, and shape) can be obtained by field mapping or by the computer-generated information based on statistical representation. A single straight fracture is discretized as follows (Fig. 3-5):

- Discretize rock matrix with an irregular Voronoi grid.
- Overlay a reference fracture on top of the Voronoi grid.
- Select node-node connections which cross the reference fracture. The corresponding Voronoi cell boundaries of such node connections are defined as a part of the discrete fracture.
- Connect all segments of the discrete fracture.

By repeating this process for a series of fractures, a network of discrete fractures can be generated. The grid size must be carefully selected or scaled to obtain the required accuracy of discrete fracture representations. The advantages of this DFN generation method include: (1) simple activation and connection of new discrete fractures, (2) automated treatment of discrete fracture intersections, (3) capability to control mesh gradation (node density), and (4) straightforward extension to 3D geometry (Fig. 3-6). These advantages are especially beneficial when simulating fracture damage that develops into fracture networks. By automating the process of the proposed DFN approach, fracture intersections in 3D can be effectively generated. Figure 3-6(a) shows a fracture intersection mapped onto an irregular 3D Voronoi grid. The visualization of DFN is facilitated by tiling the discrete fractures with the Voronoi cell boundaries, especially for 3D representation. Alternatively, the Voronoi grid can be controlled to generate straight fractures with an intersection as shown in Figure 3-6(b). Such grid generation, however, becomes cumbersome due to greater limitation on the point allocations around straight fractures, especially for inclined fracture intersections in 3D.

Figure 3-7 shows a typical example of 2D discrete fracture networks in the excavation damage zone (EDZ). The general configuration of bedding planes and fractures are partly based on the conceptual model of Bossart et al. (2004). As can be seen from Figure 3-7, the common issues associated with mesh generation for ordinary DFN (Reichenberger et al., 2006) can be greatly minimized.

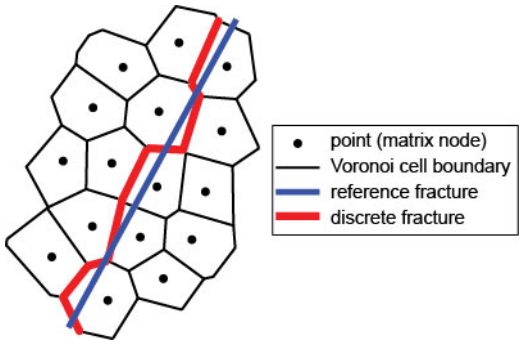

Figure 3-5. Mapping of a fracture geometry on top an irregular Voronoi grid.

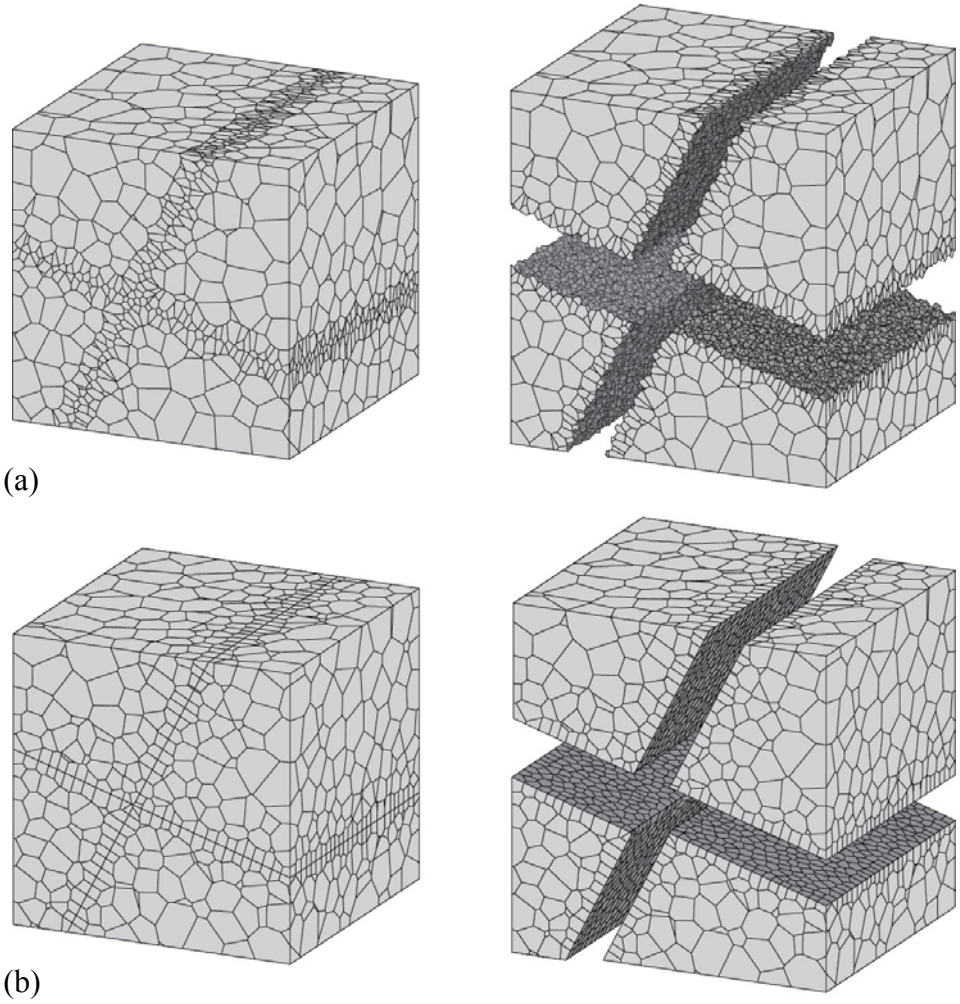

Figure 3-6. Fracture interface with the representation of DFN in 3D Voronoi grid: (a) irregular fractures, and (b) straight fractures.

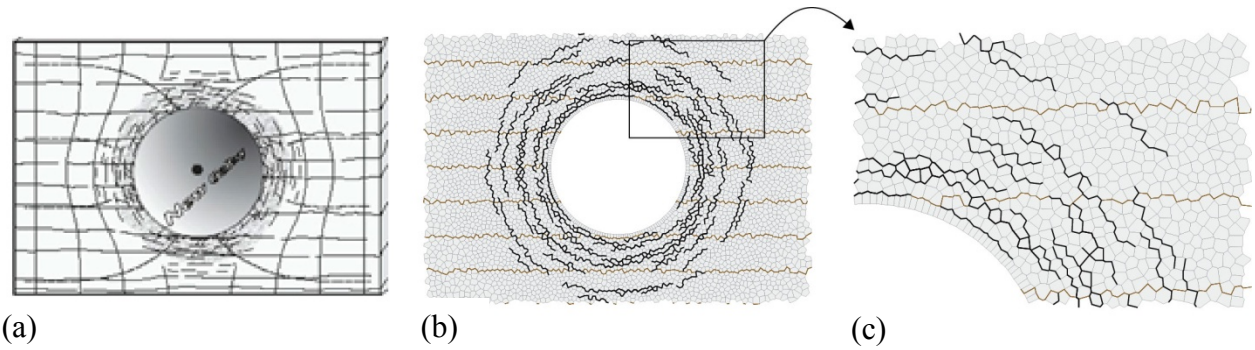

Figure 3-7. Bedding planes and fractures of EDZ in 2D representations: (a) conceptual model after Bossart et al., (2004); (b) DFN in Voronoi grid; and (c) enlarged view.

3.3.3 Implementation for Hydrogeology

The simulations of flow and mass transport through discrete fractures, presented in Section 3.4, are based on the TOUGH2 EOS7R simulator (Oldenburg and Pruess, 1995). As discussed in the preceding section, the DFN is explicitly represented at the Voronoi cell boundaries in a computational domain. To activate flow pathways along a discrete fracture, the fracture nodes and connections are newly introduced at the Voronoi cell boundary, in addition to Voronoi cell nodes and connections for the rock matrix (Fig. 3-8). A new fracture node is inserted at the intersection of a Voronoi cell boundary and the original matrix-matrix connection. Then, the connection is generated between the fracture node and the adjacent matrix nodes. Also, the fracture vertex node is added to support fracture-fracture connections along the Voronoi cell boundary. Without vertex nodes, flow between nodes, flow between nodes can produce unphysical flow pathways. Without the vertex node, flow between nodes 1 and 2 can take an unphysical route through node 3 (see green pathways and arrows, see Figure 3.8-(c)). With the vertex node, flow between nodes 1 and 2 is constrained to move along the physically-correct pathway (red fracture path and arrows). These additional nodes and connections in the TOUGH2 simulator permit flow and transport through the DFN. Indication of model accuracy and applicability of this approach are given in the Sections 3.4 and 3.6.

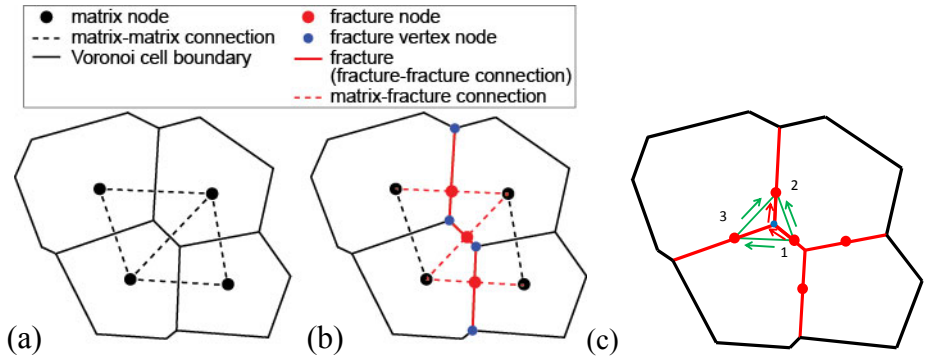

Figure 3-8. Node and connection in the TOUGH2 simulator: (a) ordinary matrix nodes and connections; (b) new fracture nodes and connections; and (c) effect of vertex node on flow pattern.

3.4 Hydrogeologic Processes in Discrete Fractures

The complexity of discrete fracture systems leads to a number of difficulties for mathematical models of hydrogeologic processes in such systems. A major issue is the geometry of the fracture network, as discussed in Section 3.3 in terms of Voronoi gridding with fractures for numerical modeling. Another difficulty is the evaluation of a model. There are many degrees of freedom in setting up a numerical discrete fracture model and it is important to check the constraints on the numerical model such that it can accurately represent the transport processes included in the model. One way to perform such a check is to compare against an analytical model that represents transport processes exactly for a limited set of idealized cases. Here, we have developed a new analytical model that extends results for a single fracture with transport by advection and matrix diffusion to include matrix advection that occurs at an arbitrary oblique angle to the fracture.

3.4.1 Analytical Model for Flow and Transport through a Single Fracture and Porous Rock Matrix

Transport through saturated fractured rock was investigated in analytical models by Neretnieks (1980), Tang et al. (1981), Sudicky and Frind (1982), and Maloszewski and Zuber (1985). However, these models did not include flow through the rock matrix; transport in the rock matrix occurred through diffusion only. Houseworth (2006) extended these modeling approaches for unsaturated flow and included longitudinal and transverse flow and transport in the matrix, as well as advective and diffusive transport between the fracture and rock matrix; longitudinal diffusion/dispersion was not included for the fracture or matrix because this greatly simplifies the analytical model and is shown in Section 3.4.2.1 to be a reasonable simplification. For an unsaturated fractured rock, the flow patterns for advective exchange between the fractures and matrix are different than for a saturated rock, where cross-flow can lead to advective exchange. In the unsaturated system, symmetry with respect to water potential about the fracture ensures

that advective exchange on each side of the fracture leads to water either flowing into the fracture from the matrix, or the converse. In a saturated system with cross-flow, water moves into the fracture from the matrix on one side and out of the fracture into the matrix on the other side. This difference in the flow pattern, as well as other differences between a saturated and unsaturated system, results in a modified governing equation for flow and transport.

The problem to be solved is saturated flow and transport through a single fracture in a porous rock matrix. Here, the longitudinal direction is defined to be the same direction as the axis of the fracture. The transverse direction is orthogonal to the fracture. While this is standard terminology, note that the pressure gradient is not required to be parallel to the fracture axis, but can be at a general oblique angle to the fracture axis. The flow problem is relatively simple: it can be characterized by three independent velocities— a fracture velocity and velocities in the matrix parallel and orthogonal to the fracture shown in Figure 3-1(a). Because solute within the fracture is assumed to be well-mixed in the transverse direction, there is no need to define a transverse fracture velocity, nor transverse diffusion in the fracture for lateral transport within the fracture. Therefore, the fracture transport problem is one-dimensional in the longitudinal direction. Transverse fluxes are treated through specifying boundary source-sink terms with the matrix. As for the previous analysis presented in Houseworth (2006), longitudinal diffusion/dispersion is not included for the fracture or matrix. The tracer is released at a general point in the fracture or rock matrix. For a single fracture in a porous rock matrix, the tracer mass conservation equation for the fracture is:

$$\begin{aligned}\phi_f\left(\frac{\partial c_f}{\partial t}+\lambda c_f\right)+\rho_{bf}\left(\frac{\partial c_{fa}}{\partial t}+\lambda c_{fa}\right)+q_f\frac{\partial c_f}{\partial z}\\ =A_{vfm}\left(\frac{1}{2}\phi_m D_m\frac{\partial c_m}{\partial x}\bigg|_{x=0^s}+\frac{1}{2}\phi_m D_m\frac{\partial c_m}{\partial x}\bigg|_{x=0^o}+\frac{1}{2}q_{fm}\big|_{x=0^s}c_m|_{x=0^s}\right.\\ \left.+\frac{1}{2}q_{fm}\big|_{x=0^o}c_m|_{x=0^o}\right)\end{aligned} \tag{3-1}$$

with initial and boundary conditions,

$$c_f(z,t)=0 \tag{3-2}$$

$$\lim_{z\to\infty}c_f(z,t)=0 \tag{3-3}$$

where, c_f is aqueous solute concentration in the fracture, $c_{fa}$is the mass of solute sorbed per unit mass of minerals in the fracture, c_m is the aqueous solute concentration in the matrix, $q_f$is the water flux in the fracture.

The fracture interface conditions are distinguished with respect to the side of the fracture where the tracer is released, designated with a superscript or subscript "s" for the side of the fracture

where tracer was released and with a superscript or subscript "o" for the opposite side of the fracture from where the tracer is released. Therefore, $q_{fm}\big|_{x=0^s}$ and $q_{fm}\big|_{x=0^o}$ denote the values of water flux normal to the fracture-matrix interface on each side of the fracture.

The pore diffusion coefficient is D_m, λ is the radioactive decay constant, ρ_{bf} is the bulk density of minerals in the fracture, $A_{vfm} = \frac{2A_r}{b}$ is the fracture area per unit fracture bulk volume and b is the fracture aperture, A_r is a fracture-matrix area reduction factor , ϕ_f is the fracture pore volume per unit fracture bulk volume, ϕ_m is the matrix pore volume per unit matrix bulk volume, t is the time since tracer release, z is the longitudinal coordinate along the fracture, and x is the transverse coordinate perpendicular to the fracture, which is zero at each fracture wall and then increases moving away from the fracture on each side of the fracture.

The conservation equation for solute mass in the matrix corresponding to Equation (3-1) is:

$$\phi_m\left(\frac{\partial c_{mk}}{\partial t} + \lambda c_{mk}\right) + \rho_{bm}\left(\frac{\partial c_{mak}}{\partial t} + \lambda c_{mak}\right) + q_{mz}\frac{\partial c_{mk}}{\partial z} + q_{mxk}\frac{\partial c_{mk}}{\partial x} = \phi_m D_m \frac{\partial^2 c_{mk}}{\partial x^2} \qquad (3\text{-}4)$$

where subscript k refers to the source (s) or the opposite (o) side of the fracture with respect to the tracer release location. The transverse flux, q_{mxk}, is defined to be positive when flowing away from the fracture for each side; therefore, $q_{mxs} = -q_{mxo}$ for a given cross-flow moving across the fracture.

The initial and boundary conditions for the matrix conservation equation are:

$$c_{ms}(z,x,0) = \frac{bM_0}{A_f \phi_m R_m}\delta(x - x_0)\delta(z) \qquad (3\text{-}5)$$

$$c_{mo}(z,x,0) = 0 \qquad (3\text{-}6)$$

$$c_{mk}(z,0,t) = c_f(z,t) \qquad (3\text{-}7)$$

$$\lim_{x\to\infty} c_{mk}(z,x,t) = 0 \qquad (3\text{-}8)$$

where M_0 is the mass of tracer released, A_f is the fracture cross-sectional area, and δ is the Dirac delta function that is dimensionally an inverse length. Equation (3-5) gives the initial condition on the source side of the fracture, and Equation (3-6) gives the initial condition on the opposite side of the fracture from the source release point. Note that if $x_0 = 0$, the initial condition is equivalent to tracer release in the fracture.

The following variables and relationships are used: $c_{fa} = K_{df}c_f$, $c_{ma} = K_{dm}c_m$, $R_f = 1 + \frac{\rho_{bf}K_{df}}{\phi_f}$, $R_m = 1 + \frac{\rho_{bm}K_{dm}}{\phi_m}$, $v_f = \frac{q_f}{\phi_f R_f}$, $v_{mx} = \frac{q_{mx}}{\phi_m R_m}$, $v_{mz} = \frac{q_{mz}}{\phi_m R_m}$, $D_m^* = \frac{D_m}{R_m}$, $c_{f\lambda} = c_f \exp(\lambda t)$, $c_{m\lambda} = c_m \exp(\lambda t)$, $\varsigma = z - v_{mz}t$, $v_f^* = v_f - v_{mz}$, as well as the following dimensionless variables, $\ell = \frac{b}{2A_r}\frac{\phi_f R_f}{\phi_m R_m}$, $\tau = \frac{v_f^* t}{\ell}$, $\xi = \frac{\varsigma}{\ell} = \frac{z - v_{mz}t}{\ell}$, $\eta = \frac{x}{\ell}$, $c_{fd} = \frac{A_f \phi_f R_f \ell}{2M_0} c_{f\lambda}$, $c_{md} = \frac{A_f \phi_f R_f \ell}{2M_0} c_{m\lambda}$, $Pe = \frac{v_f^* \ell}{D_m^*}$, $V_k = \frac{v_{mxk}}{v_f^*}$, $\delta(\eta - \eta_0) = \ell\delta(x - x_0)$, $\delta(\xi) = \ell\delta(z)$.

Using these variables in Equations (3-1) through (3-3), and recognizing that $c_m|_{x=0^s} = c_m|_{x=0^o} = c_f$ and $q_{fm}\big|_{x=0^s} = -q_{fm}\big|_{x=0^o}$ gives,

$$\frac{\partial c_{fd}}{\partial \tau} + \frac{\partial c_{fd}}{\partial \xi} = \frac{1}{2}\left(\frac{1}{Pe}\frac{\partial c_{md}}{\partial \eta}\bigg|_{\eta=0^s} + \frac{1}{Pe}\frac{\partial c_{md}}{\partial \eta}\bigg|_{\eta=0^o}\right) \tag{3-9}$$

$$c_{fd}(\xi, 0) = 0 \tag{3-10}$$

$$\lim_{\xi\to\infty} c_{fd}(\xi, \tau) = 0 \tag{3-11}$$

and Equations (3-4) through (3-8) become:

$$\frac{\partial c_{mdk}}{\partial \tau} + V_k \frac{\partial c_{mdk}}{\partial \eta} = \frac{1}{Pe}\frac{\partial^2 c_{mdk}}{\partial \eta^2} \tag{3-12}$$

$$c_{mds}(\xi, \eta, 0) = \delta(\xi)\delta(\eta - \eta_0) \tag{3-13}$$

$$c_{mdo}(\xi, \eta, 0) = 0 \tag{3-14}$$

$$c_{mdk}(\xi, 0, \tau) = c_{fd}(\xi, \tau) \tag{3-15}$$

$$\lim_{\eta\to\infty} c_{mdk}(\xi, \eta, \tau) = 0 \tag{3-16}$$

A Laplace-transform method is used to solve these equations, similar to the solution method presented in Houseworth (2006). The result for dimensionless fracture concentration is,

$$c_{fd}(\xi, \tau) = H(\tau - \xi)H(\xi)\frac{\xi + Pe\eta_0}{4\sqrt{\pi}\sqrt{Pe}(\tau - \xi)^{\frac{3}{2}}}\exp\left(-\frac{PeV_s}{2}\eta_0\right)$$
$$\exp\left(-\frac{(\xi + Pe\eta_0)^2}{4Pe(\tau - \xi)} - \frac{PeV^2(\tau - \xi)}{4}\right) \tag{3-17}$$

The matrix concentration for the side of the fracture opposite the source is

$$c_{mdo}(\xi,\eta,\tau) = H(\tau-\xi)H(\xi)\exp\left(\frac{PeV_o(\eta+\eta_0)}{2}\right)\frac{\xi+Pe(\eta+\eta_0)}{4\sqrt{\pi}\sqrt{Pe}(\tau-\xi)^{\frac{3}{2}}}$$
$$\exp\left\{-\frac{\left(\xi+Pe(\eta+\eta_0)\right)^2}{4Pe(\tau-\xi)}-\frac{PeV^2(\tau-\xi)}{4}\right\} \tag{3-18}$$

and for the matrix on the source side of the fracture,

$$c_{mds}(\xi,\eta,\tau) = H(\tau-\xi)H(\xi)\exp\left\{\frac{PeV_s(\eta-\eta_0)}{2}\right\}\frac{\xi+Pe(\eta+\eta_0)}{4\sqrt{\pi}\sqrt{Pe}(\tau-\xi)^{\frac{3}{2}}}$$
$$\exp\left(-\frac{\left(\xi+Pe(\eta+\eta_0)\right)^2}{4Pe(\tau-\xi)}-\frac{PeV^2(\tau-\xi)}{4}\right) \tag{3-19}$$
$$+\frac{\sqrt{Pe}\delta(\xi)}{2\sqrt{\pi\tau}}\exp\left\{\frac{PeV_s}{2}(\eta-\eta_0)-\frac{PeV^2\tau}{4}\right\}\left[\exp\left\{-\frac{Pe(\eta-\eta_0)^2}{4\tau}\right\}-\exp\left\{-\frac{Pe(\eta+\eta_0)^2}{4\tau}\right\}\right]$$

These results for concentrations in the fracture and matrix can be integrated at a position downstream along the fracture for cumulative mass arrivals in the fracture, M_f, and on both sides of the matrix, M_k. For the cumulative mass solutions, the following additional dimensionless variables are defined: $V_\ell = \frac{v_{mz}}{v_f}$, $\zeta_e = \frac{z_e}{\ell}$, $\lambda_d = \frac{\lambda\ell}{v_f}$, $\psi = \frac{v_f T}{\ell}$, where z_e is the downstream location at which cumulative mass arrivals are computed and T is the time of observation at z_e. The result for cumulative mass arrival in the fracture is:

$$\frac{M_f(\psi)}{M_0} = \frac{\sqrt{V_\ell^2+Pe^2V^2+4Pe\lambda_d}+V_\ell}{2\sqrt{V_\ell^2+Pe^2V^2+4Pe\lambda_d}}$$
$$\exp\left(\frac{\{\zeta_e(1-V_\ell)+Pe\eta_0\}\left\{\sqrt{V_\ell^2+Pe^2V^2+4Pe\lambda_d}+V_\ell\right\}-2Pe\lambda_d\zeta_e}{2Pe}-\frac{PeV_s\eta_0}{2}\right) \tag{3-20}$$
$$\operatorname{erfc}\left(\frac{\{\zeta_e(1-V_\ell)+Pe\eta_0\}}{2\sqrt{Pe}\sqrt{\psi-\zeta_e}}+\frac{\sqrt{V_\ell^2+Pe^2V^2+4Pe\lambda_d}\sqrt{\psi-\zeta_e}}{2\sqrt{Pe}}\right)$$
$$+\frac{\sqrt{V_\ell^2+Pe^2V^2+4Pe\lambda_d}-V_\ell}{2\sqrt{V_\ell^2+Pe^2V^2+4Pe\lambda_d}}$$

$$\exp\left(-\frac{\{\zeta_e(1-V_\ell)+Pe\eta_0\}\left\{\sqrt{V_\ell^2+Pe^2V^2+4Pe\lambda_d}-V_\ell\right\}+2Pe\lambda_d\zeta_e}{2Pe}-\frac{PeV_s\eta_0}{2}\right)$$

$$\operatorname{erfc}\left(\frac{\{\zeta_e(1-V_\ell)+Pe\eta_0\}}{2\sqrt{Pe}\sqrt{\psi-\zeta_e}}-\frac{\sqrt{V_\ell^2+Pe^2V^2+4Pe\lambda_d}\sqrt{\psi-\zeta_e}}{2\sqrt{Pe}}\right)$$

The result for cumulative mass arrival in matrix on opposite side of fracture from the source release location is:

$$\frac{M_{mo}(\psi)}{M_0}=\frac{V_\ell V_s}{2(V_sV_\ell+2\lambda_d)}\exp\left(-\frac{(V_sV_\ell+2\lambda_d)(\psi-\zeta_e)-V_s(1-V_\ell)\zeta_e+2\lambda_d\zeta_e}{2}\right)$$

$$\operatorname{erfc}\left\{\frac{\{\zeta_e(1-V_\ell)+Pe\eta_0\}+(PeV_s-V_\ell)(\psi-\zeta_e)}{2\sqrt{Pe}\sqrt{\psi-\zeta_e}}\right\}$$

$$-\left\{\frac{V_\ell V_s(PeV_s-V_\ell)+V_\ell V_s\sqrt{Pe^2V^2+V_\ell^2+4Pe\lambda_d}}{4(V_sV_\ell+2\lambda_d)\sqrt{Pe^2V^2+V_\ell^2+4Pe\lambda_d}}+\frac{V_\ell}{2\sqrt{Pe^2V^2+V_\ell^2+4Pe\lambda_d}}\right\}$$

$$\exp\left(\frac{\{\zeta_e(1-V_\ell)+Pe\eta_0\}\left\{\sqrt{Pe^2V^2+V_\ell^2+4Pe\lambda_d}+V_\ell\right\}-2Pe\lambda_d\zeta_e}{2Pe}-PeV_s\eta_0\right)$$

$$\operatorname{erfc}\left(\frac{\{\zeta_e(1-V_\ell)+Pe\eta_0\}+(\psi-\zeta_e)\sqrt{Pe^2V^2+V_\ell^2+4Pe\lambda_d}}{2\sqrt{Pe}\sqrt{\psi-\zeta_e}}\right) \qquad (3\text{-}21)$$

$$+\left\{\frac{V_\ell V_s(PeV_s-V_\ell)-V_\ell V_s\sqrt{Pe^2V^2+V_\ell^2+4Pe\lambda_d}}{4(V_oV_\ell+2\lambda_d)\sqrt{Pe^2V^2+V_\ell^2+4Pe\lambda_d}}+\frac{V_\ell}{2\sqrt{Pe^2V^2+V_\ell^2+4Pe\lambda_d}}\right\}$$

$$\exp\left(-\frac{\{\zeta_e(1-V_\ell)+Pe\eta_0\}\left\{\sqrt{Pe^2V^2+V_\ell^2+4Pe\lambda_d}-V_\ell\right\}+2Pe\lambda_d\zeta_e}{2Pe}-PeV_s\eta_0\right)$$

$$\operatorname{erfc}\left(\frac{\{\zeta_e(1-V_\ell)+Pe\eta_0\}-(\psi-\zeta_e)\sqrt{Pe^2V^2+V_\ell^2+4Pe\lambda_d}}{2\sqrt{Pe}\sqrt{\psi-\zeta_e}}\right)$$

Finally, the cumulative mass arrival in matrix on same side of fracture as the source release location is:

$$
\begin{aligned}
&\frac{M_{ms}(\psi)}{M_0} \\
&= \frac{V_\ell V_s}{2(V_s V_\ell - 2\lambda_d)} \exp\left(\frac{(V_s V_\ell - 2\lambda_d)(\psi - \zeta_e) - V_s(1 - V_\ell)\zeta_e - 2PeV_s\eta_0 - 2\lambda_d\zeta_e}{2}\right) \\
&\qquad \operatorname{erfc}\left\{\frac{\{\zeta_e(1 - V_\ell) + Pe\eta_0\} - (PeV + V_\ell)(\psi - \zeta_e)}{2\sqrt{Pe}\sqrt{\psi - \zeta_e}}\right\} \\
&+ \left\{\frac{V_\ell V_s(PeV_s + V_\ell) - V_\ell V_s\sqrt{Pe^2V^2 + V_\ell^2 + 4Pe\lambda_d}}{4(V_s V_\ell - 2\lambda_d)\sqrt{Pe^2V^2 + V_\ell^2 + 4Pe\lambda_d}} - \frac{V_\ell}{2\sqrt{Pe^2V^2 + V_\ell^2 + 4Pe\lambda_d}}\right\} \\
&\exp\left(\frac{\{\zeta_e(1 - V_\ell) + Pe\eta_0\}\left\{\sqrt{Pe^2V^2 + V_\ell^2 + 4Pe\lambda_d} + V_\ell\right\} - 2Pe\lambda_d\zeta_e}{2Pe} - \frac{PeV_s\eta_0}{2}\right) \\
&\qquad \operatorname{erfc}\left(\frac{\{\zeta_e(1 - V_\ell) + Pe\eta_0\} + (\psi - \zeta_e)\sqrt{Pe^2V^2 + V_\ell^2 + 4Pe\lambda_d}}{2\sqrt{Pe}\sqrt{\psi - \zeta_e}}\right) \\
&- \left\{\frac{V_\ell V_s(PeV_s + V_\ell) + V_\ell V_s\sqrt{Pe^2V^2 + V_\ell^2 + 4Pe\lambda_d}}{4(V_s V_\ell - 2\lambda_d)\sqrt{Pe^2V^2 + V_\ell^2 + 4Pe\lambda_d}} - \frac{V_\ell}{2\sqrt{Pe^2V^2 + V_\ell^2 + 4Pe\lambda_d}}\right\} \\
&\exp\left(-\frac{\{\zeta_e(1 - V_\ell) + Pe\eta_0\}\left\{\sqrt{Pe^2V^2 + V_\ell^2 + 4Pe\lambda_d} - V_\ell\right\} + 2Pe\lambda_d\zeta_e}{2Pe} - \frac{PeV_s\eta_0}{2}\right) \\
&\qquad \operatorname{erfc}\left(\frac{\{\zeta_e(1 - V_\ell) + Pe\eta_0\} - (\psi - \zeta_e)\sqrt{Pe^2V^2 + V_\ell^2 + 4Pe\lambda_d}}{2\sqrt{Pe}\sqrt{\psi - \zeta_e}}\right)
\end{aligned}
\tag{3-22}
$$

Examples of the analytical model transport responses are given in Figures 3-9 and 3-10 for flow parallel to the fracture, and in Figures 3-11 and 3-12, for flow at an oblique angle to the fracture. Figure 3-9 shows the symmetric contour pattern for concentration for the case where flow is parallel with the fracture. The parameters used for the calculation are given in this figure. Mass arrival results in 3-10(a) and 3-10(b) show most of the tracer arrival occurs via transport through the fracture, with equal contributions from each side of the matrix. Note that the terminology used for matrix sides (source and opposite) are arbitrary for the cases shown here because the source is in the fracture, not the matrix.

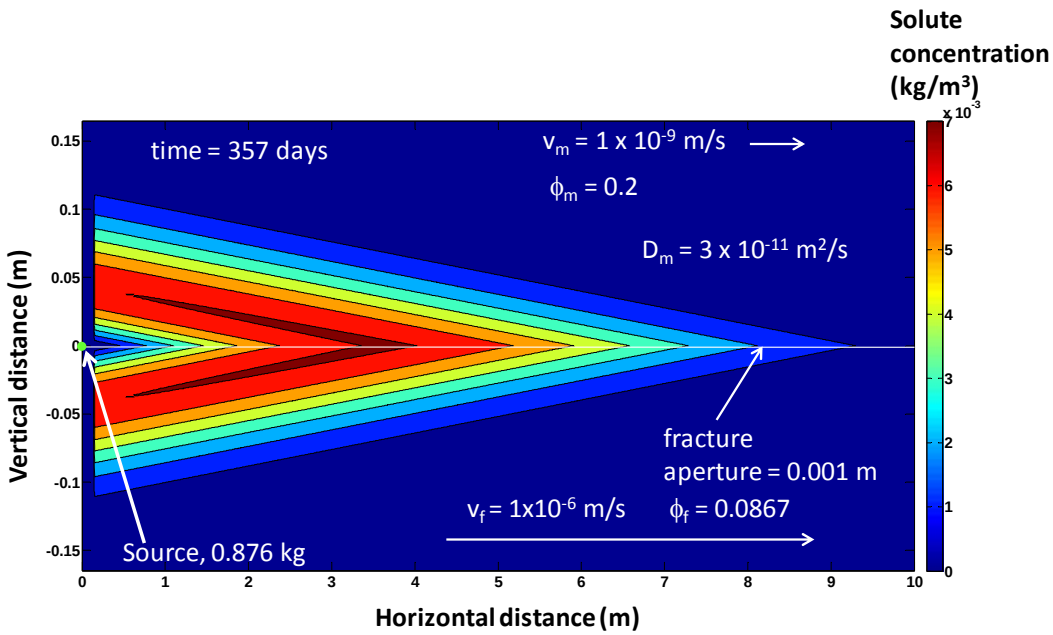

Figure 3-9. Transport results from single-fracture analytical model for flow parallel to the fracture. Contour plot of concentrations at 357 days.

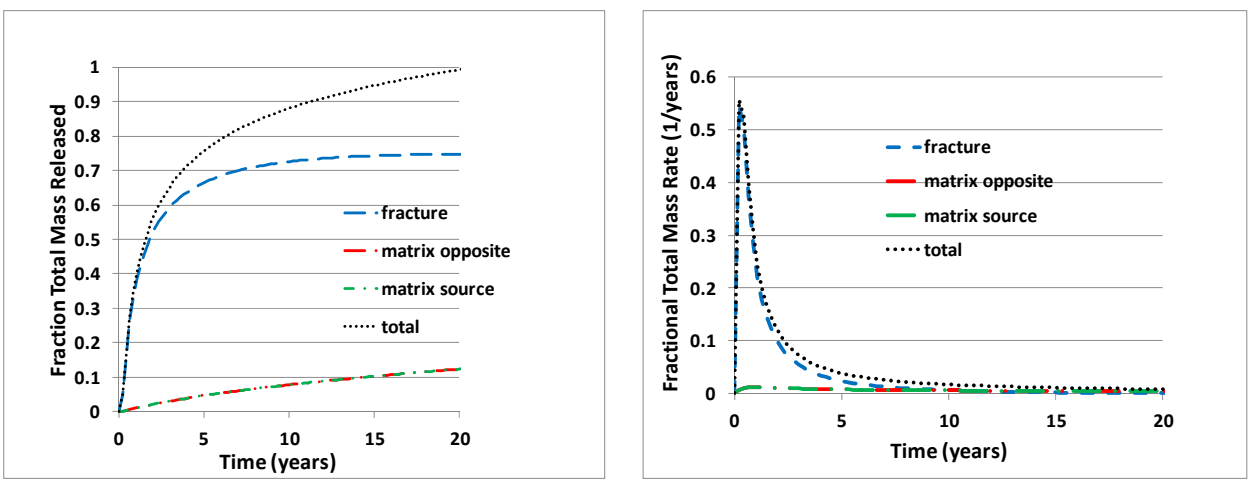

(a) (b)

Figure 3-10. Transport results from single-fracture analytical model for flow parallel to fracture; arrivals 10 m downstream of the source release point, normalized by mass released. (a) cumulative mass arrivals in fracture and matrix; (b) mass-arrival rates in fracture and matrix.

The case with an oblique cross-flow is shown in Figures 3-11 and 3-12. The only difference between this case and the case with parallel flow (Figures 3-9 and 3-10) is the non-zero cross-flow velocity in the matrix. The asymmetry of the contour plot relative to the fracture is a result of the matrix cross-flow component orthogonal to the fracture. Cumulative mass arrivals in Figure 3-12 are slower as compared with the parallel flow case, and a much larger fraction of the

arrivals occur through the matrix. The peak mass arrival rate in Figure 3-12(b) is slightly smaller than in the parallel flow case, but following the peak, a residual mass-arrival rate persists and even increases slightly over 20 years, as compared with the decay in mass-arrival rate for the parallel flow case.

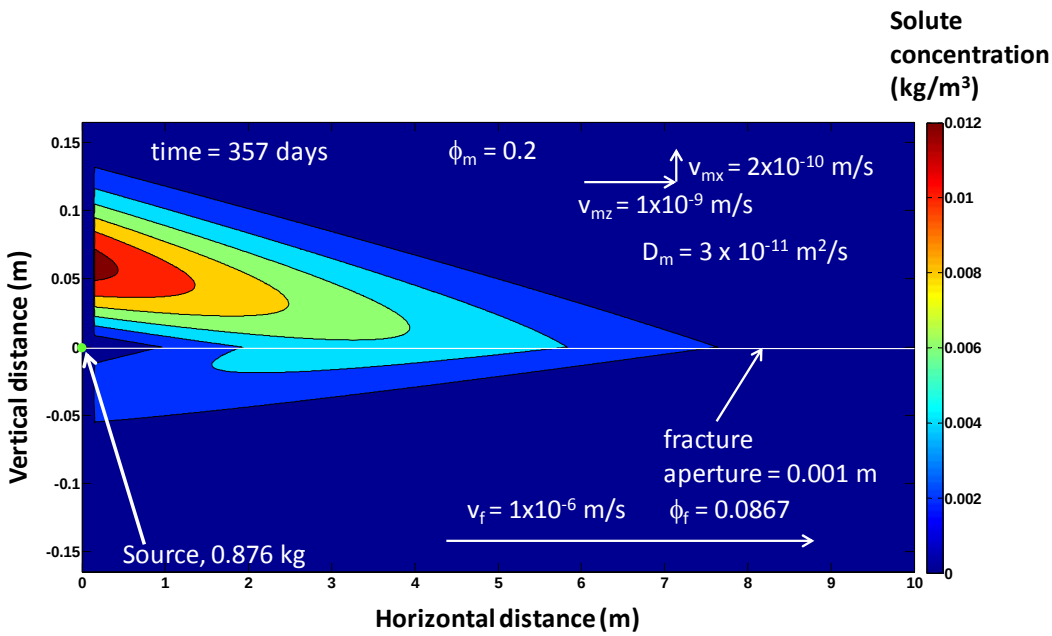

Figure 3-11. Transport results from single-fracture analytical model for matrix flow at an oblique angle to the fracture. Contour plot of concentrations at 357 days.

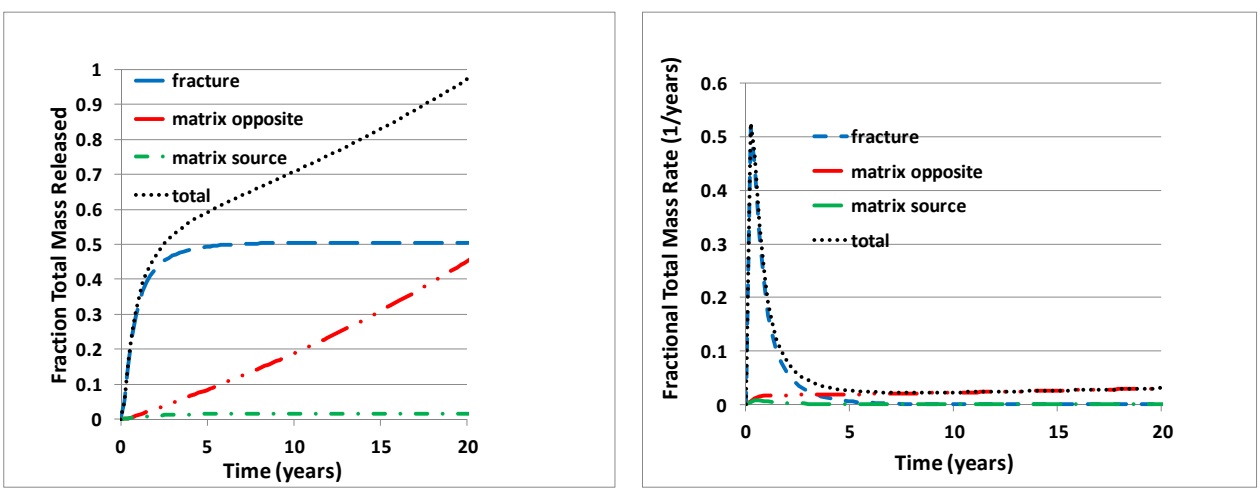

(a) (b)

Figure 3-12. Transport results from single-fracture analytical model for matrix flow at an oblique angle to the fracture; arrivals 10 m downstream of the source release point, normalized by mass released (a) cumulative mass arrivals in fracture and matrix; (b) mass-arrival rates in fracture and matrix.

The case with cross-flow at a 45-degree angle to the fracture is shown in Figures 3-13 and 3-14. The only difference between this case and the case with oblique flow (Figures 3-11 and 3-12) is the increase in cross-flow velocity in the matrix. The contour plot shows that the solute has effectively disconnected from the fracture at 357 days as a result of the strong cross flow. Cumulative mass arrivals at the downstream location are much slower compared with both previous cases and most of the arrivals occur through the matrix. The initial peak mass-arrival rate is also much smaller than in the previous cases and following this first peak and decline, the mass-arrival rate grows throughout the 20-year time period to a level approximately equal to the initial peak.

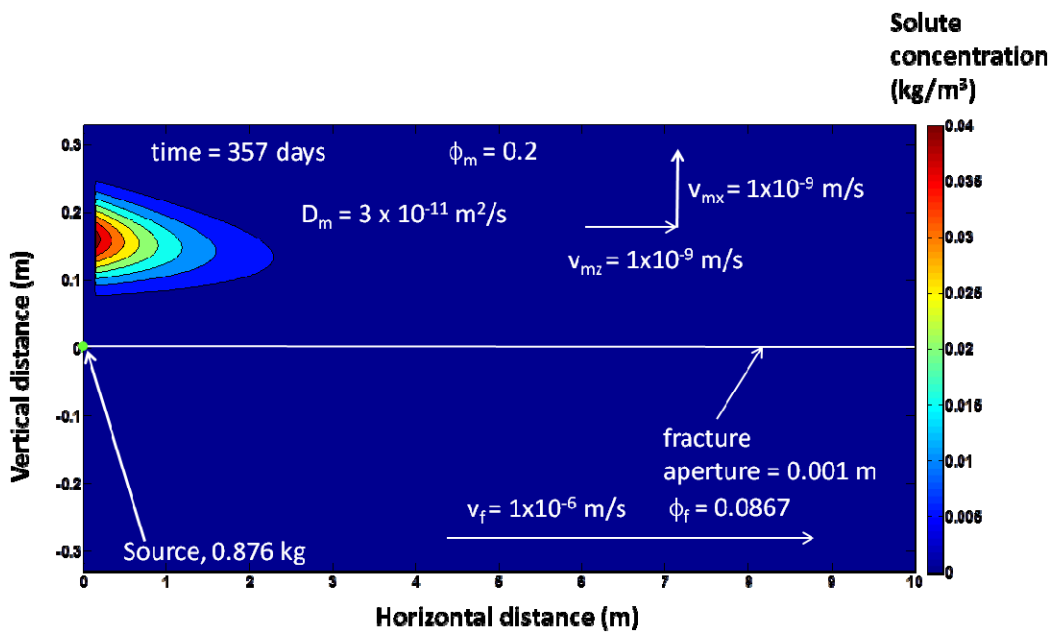

Figure 3-13. Transport results from single-fracture analytical model for matrix flow at a 45 degree angle to the fracture. Contour plot of concentrations at 357 days.

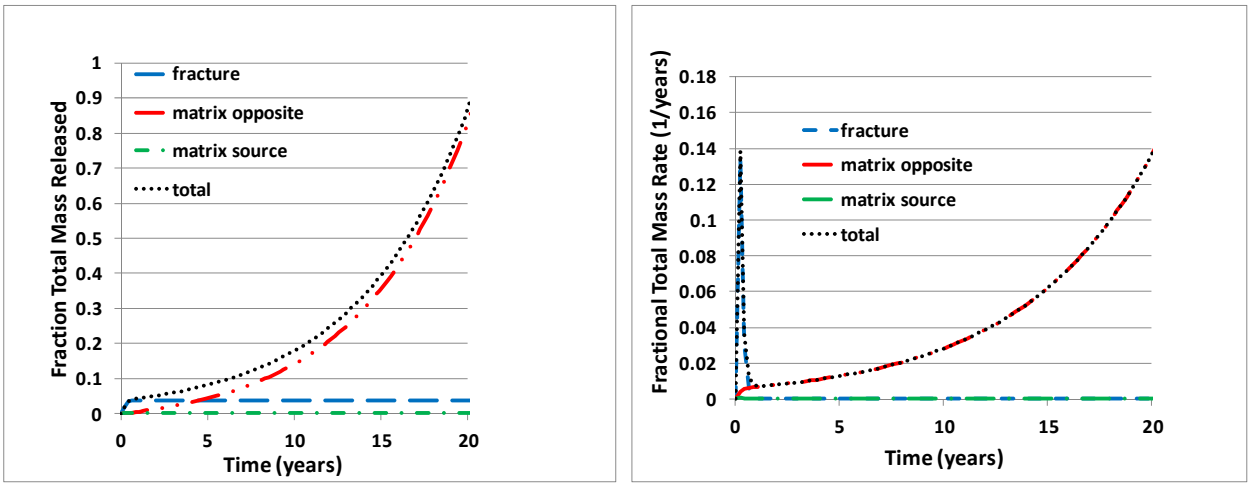

(a) (b)

Figure 3-14. Transport results from single-fracture analytical model for matrix flow at a 45-degree angle to the fracture; arrivals 10 m downstream of the source release point, normalized by mass released (a) cumulative mass arrivals in fracture and matrix; (b) mass-arrival rates in fracture and matrix.

3.4.2 Numerical discrete fracture hydrogeologic model

A numerical discrete fracture model for a single fracture in a porous rock matrix is described here. This model includes the case investigated with the analytical model in which the fracture is a single linear feature that connects across the entire domain, but also treats the more general case of an irregular fracture that follows along the cell boundaries of a random Voronoi grid. This set of models is useful because numerical results for the simpler straight fracture case can be verified against the analytical model and, therefore, provide a reliable baseline for flow and transport behavior to evaluate the effects of irregular fracture geometry. Four cases involving flow parallel to the fracture and flow at an oblique angle to the fracture are considered for the linear and irregular fracture geometries.

The numerical solutions for flow and transport were conducted using TOUGH2 with the EOS7R module (Oldenburg and Pruess, 1995). Flow calculations were performed to establish steady-state flow fields that were used as an initial condition for the tracer transport problem. For transport, an instantaneous point release of tracer was approximated by including at the beginning of the transport calculation tracer mass in one cell in the fracture. All problems were solved for a two-dimensional rectangular domain.

3.4.2.1 Linear fractures—verification with analytical solution

For parallel flow, the solution is symmetric about the fracture, so one boundary is taken along the fracture centerline. The domain is 10 m long and about 0.4 m in width, with a 0.015 m fracture

half-aperture. Flow was computed using constant-pressure boundary conditions at each end of the 10-m long domain and no-flow boundary conditions for the transverse direction. For the cross-flow case, symmetry is broken; therefore, the fracture is placed in the middle of the domain with a full aperture of 0.03 m. A uniform grid was used in the longitudinal direction (along the fracture axis). A longitudinal grid spacing of 1 cm was used for the parallel flow case and 2 cm for the cross-flow case. Grid spacing laterally was 0.002 m along the fracture and graded to coarser grids further from the fracture. For the cross-flow case, fine gridding in the transverse direction was necessary for a larger region around the fracture than for the parallel-flow case. Hydrogeologic parameters used are given in Table 3-1. Conditions and gridding that were varied are given in Table 3-2. In all cases, the domain length is 10 m and the pressure drop over this length is 5×10^4 Pa. Table 3-3 gives the flow velocities for each case.

Table 3-1. Linear Fracture Simulation Cases – Parameters.

Fracture permeability (m^2)	Matrix permeability (m^2)	Fracture aperture (m)	Fracture porosity	Matrix porosity	Diffusion coefficient (m^2/s)
2.4×10^{-15}	1.0×10^{-18}	0.03	0.087	0.2	1.0×10^{-11}

Table 3-2. Linear Fracture Simulation Cases – Grid and Domain.

Case	Pressure drop (transverse, Pa)	Transverse dimension (m)	Longitudinal grid spacing (m)	Lateral grid spacing (m)
Parallel flow – base case	0	0.4	0.01	0.002, 0.004, 0.008, 0.016, 0.032, 0.064, 0.128(2)
Parallel flow – sensitivity case 1	0	0.4	0.06	0.002, 0.004, 0.008, 0.016, 0.032, 0.064, 0.128(2)
Parallel flow – sensitivity case 2	0	0.4	0.1	0.002, 0.004, 0.008, 0.016, 0.032, 0.064, 0.128(2)
Parallel flow – sensitivity case 3	0	0.4	0.1	0.01, 0.02, 0.03, 0.04, 0.05, 0.06, 0.07, 0.08
Cross flow – base case	6.2×10^4	1.25	0.02	0.002 (80;20), 0.004, 0.008, 0.016, 0.032, 0.064, 0.128, 0.256, 0.512

Cross flow – sensitivity case 1	5.1×10^4	1.05	0.1	0.002, 0.004, 0.008, 0.016, 0.032, 0.064, 0.128, 0.256, 0.512
Cross flow – sensitivity case 2	5.1×10^4	1.05	0.02	0.002, 0.004, 0.008, 0.016, 0.032, 0.064, 0.128, 0.256, 0.512
Cross flow – sensitivity case 3	6.2×10^4	1.25	0.1	0.002 (80;20), 0.004, 0.008, 0.016, 0.032, 0.064, 0.128, 0.256, 0.512

Table 3-3. Flow velocities.

	v_f (m/s)	v_{mz} (m/s)	v_{mx} (m/s)
Parallel flow cases	1.6×10^{-7}	2.8×10^{-11}	0
Cross-flow flow cases	1.6×10^{-7}	2.8×10^{-11}	2.9×10^{-10}

Results for the simulations are compared with analytical solutions in Figures 3-15 through 3-17. Results in Figures 3-15 and 3-16 for concentration profiles show that the solution is most sensitive to grid refinement near the fracture, and that longitudinal grid dimensions may be coarser. Additional transverse grid refinement in the matrix near the fracture appears to be necessary to achieve the same level of accuracy in the numerical model for the cases with cross flow. This is a result of cross flow moving the peak mass concentration from the fracture and into the matrix. Steep concentration gradients are associated with the location of the peak mass concentration. The results also show that with sufficient grid refinement, numerical results can closely match the analytical solution, even though the numerical model includes longitudinal diffusion not represented in the analytical model. The numerical base-case results are compared with analytical results in Figure 3-17 for cumulative mass arrival at a downstream position 4 m from the release point. Cross flow is seen to slow longitudinal mass transport at later times. Cumulative mass arrival is a convenient metric for comparing results for linear and irregular fracture cases discussed next.

Lateral grid spacing is indicated for one side of fracture – and is symmetric about the fracture except for the cross-flow base case and cross-flow sensitivity case 3. Numbers in parentheses indicate repeated grid dimensions; for cross-flow base case and sensitivity case 3, 0.002 (80; 20) indicates 80, 0.002 m cells in the transverse direction next to fracture on downstream side of fracture and 20, 0.002 m cells on upstream side of fracture.

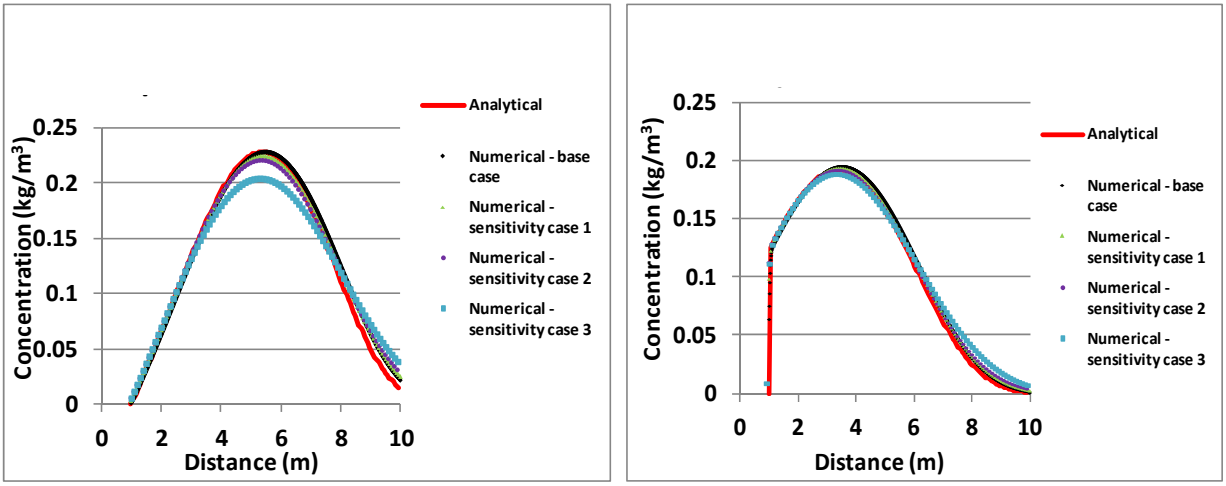

(a) (b)

Figure 3-15. Solute concentration profiles at 1042 days for parallel flow case: (a) fracture concentration profile; (b) matrix concentration profile about 2 cm from fracture.

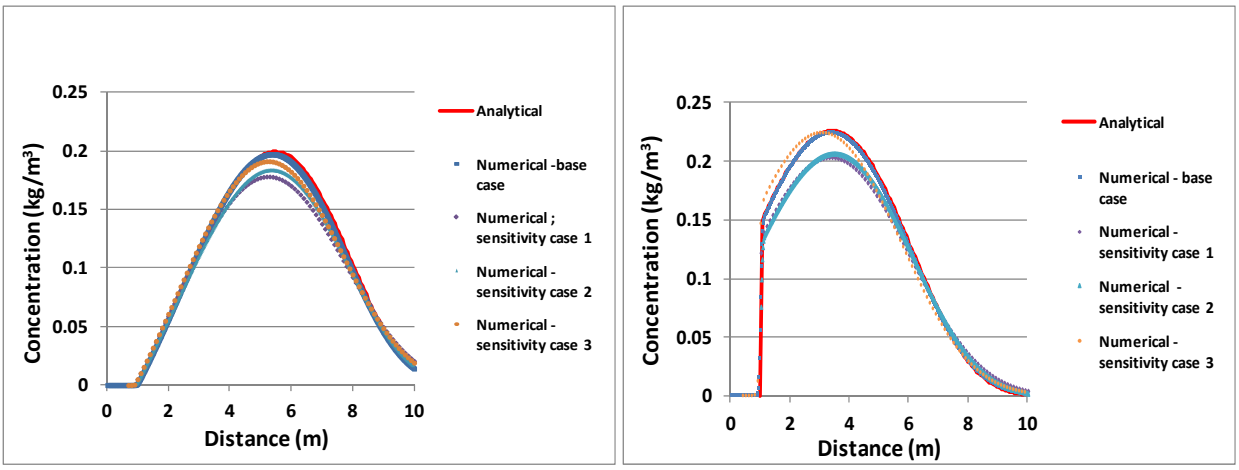

(a) (b)

Figure 3-16. Solute concentration profiles at 1042 days for cross-flow case: (a) fracture concentration profile; (b) matrix concentration profile about 2 cm from fracture.

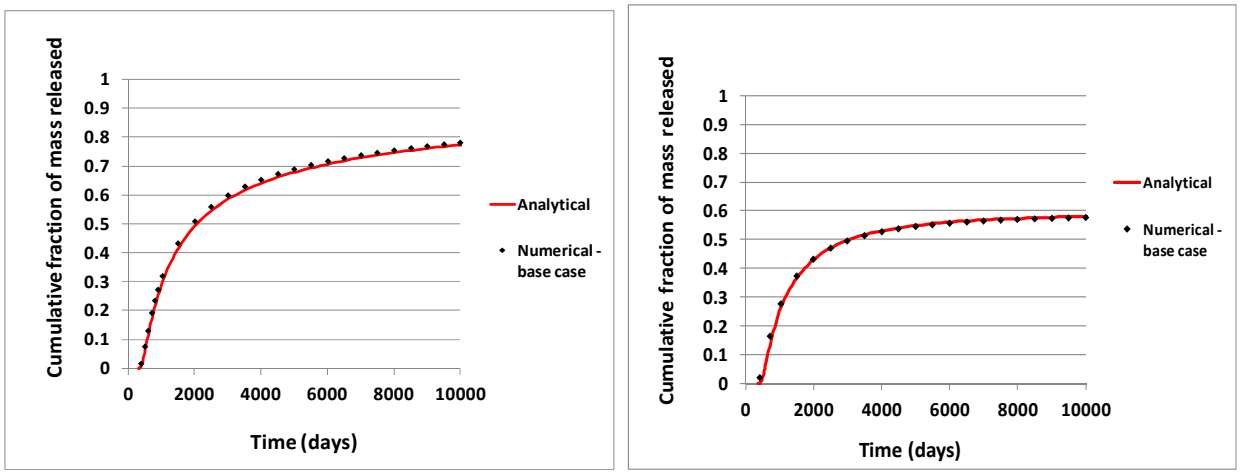

(a) (b)

Figure 3-17. Cumulative mass arrival 4 m from release point: (a) parallel flow base case; (b) cross-flow base case.

3.4.2.2 Irregular fractures – comparison with linear fracture results

The use of an irregular Voronoi grid permits a more flexible numerical method to account for fracture and matrix hydrogeological processes coupled with geomechanical damage processes that result in the introduction of new fractures. Therefore, it is of interest to compare a hydrogeological flow and transport calculation in which a fracture follows the Voronoi cell boundaries along the same mean fracture path as computed above for a straight fracture. The irregular case given here is comparable to the case above where the pressure gradient is aligned with the fracture axis. Figure 3-18 shows the Voronoi grid with a fracture following the Voronoi cell boundaries. Although the fracture follows an irregular path in detail, at a larger scale, the average fracture path is horizontal.

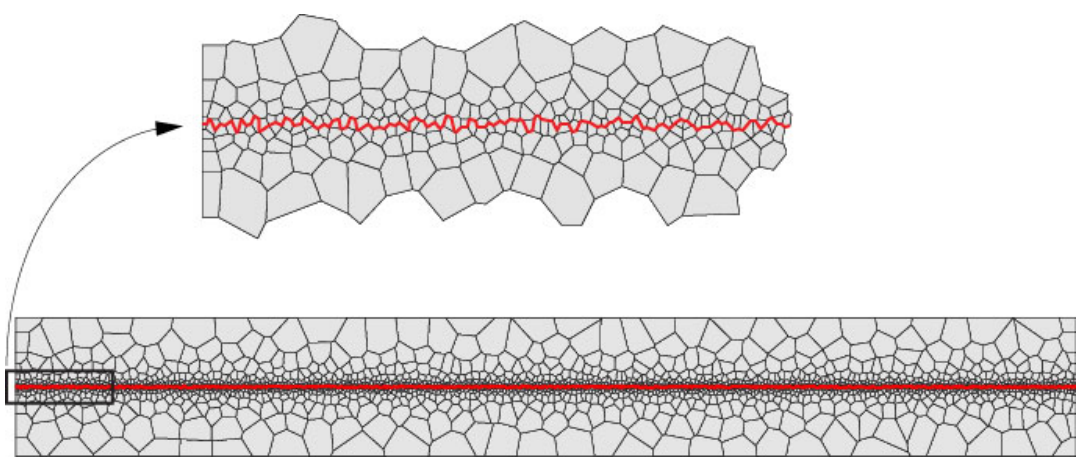

Figure 3-18. Voronoi grid with irregular fracture.

The fracture irregularities increase the overall fracture path length between any two horizontal coordinates. The fracture permeability for the irregular case is scaled such that the flow rate through the irregular fracture is the same as through a straight fracture for the same pressure boundary conditions. Given the same fracture aperture, this scaling is simply the ratio of the irregular fracture path length to the straight fracture path length.

Transport results are compared using the cumulative mass arrivals from a point source in the fracture. The results for the straight fracture at a position of 4 m downstream of the source are compared with the irregular case at a position 2.7 m downstream because this position corresponds to the same total fracture path length (4 m) for the irregular fracture case. It is also possible to achieve the same effect by scaling the fracture porosity and fracture-matrix interface area reduction factor, as discussed below, but this scaling was not done for the irregular cases computed here. Figure 3-19 shows the cumulative mass arrival curves for the analytical result for a straight fracture and for two irregular fracture cases. The irregular fracture cases represent different degrees of grid refinement, ranging from 1065 nodes to 8181 nodes. As seen in Figure 3-19, the irregular cases lead to faster arrivals as compared with the analytical straight-fracture case.

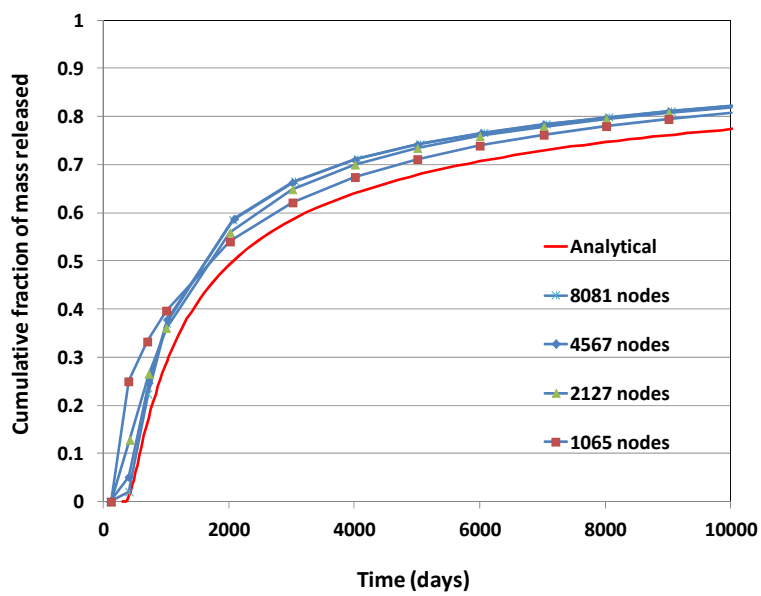

Figure 3-19. Comparison of mass cumulative mass arrivals at a fracture-path distance of 4 m from the source for a straight fracture (analytical) and for four irregular fracture cases (1065, 2127, 4567, and 8081 nodes).

This result is counterintuitive, because matrix cross-flow for the irregular case, not present in the straight-fracture case, was expected to cause more fracture-matrix exchange and slow down transport. Although cross-flow does result in an increase in fracture-matrix exchange, this

exchange is enhanced both for solute moving from the fracture to the matrix and for solute moving from the matrix to the fracture. This is indicated in the conceptual diagram of Figure 3-20. In this figure, the irregular fracture is idealized as a repeating saw-tooth pattern. The effects of matrix advection with an irregular fracture show that matrix advection leads to solute movement both out of the fracture and into the fracture. In fact, if there were no diffusion, matrix advection would cause solute to move from the fracture to the matrix, but would always return the solute back to the fracture. This is different from the effects of diffusion, which can move solute far from the fracture. Furthermore, solute that moves into the matrix by diffusion can return to the fracture through matrix advection, which cannot occur for the straight-fracture case. It appears that matrix advective transport tends to keep solute in closer proximity to the fracture for the irregular fracture case, causing a slight increase in the net solute transport rate.

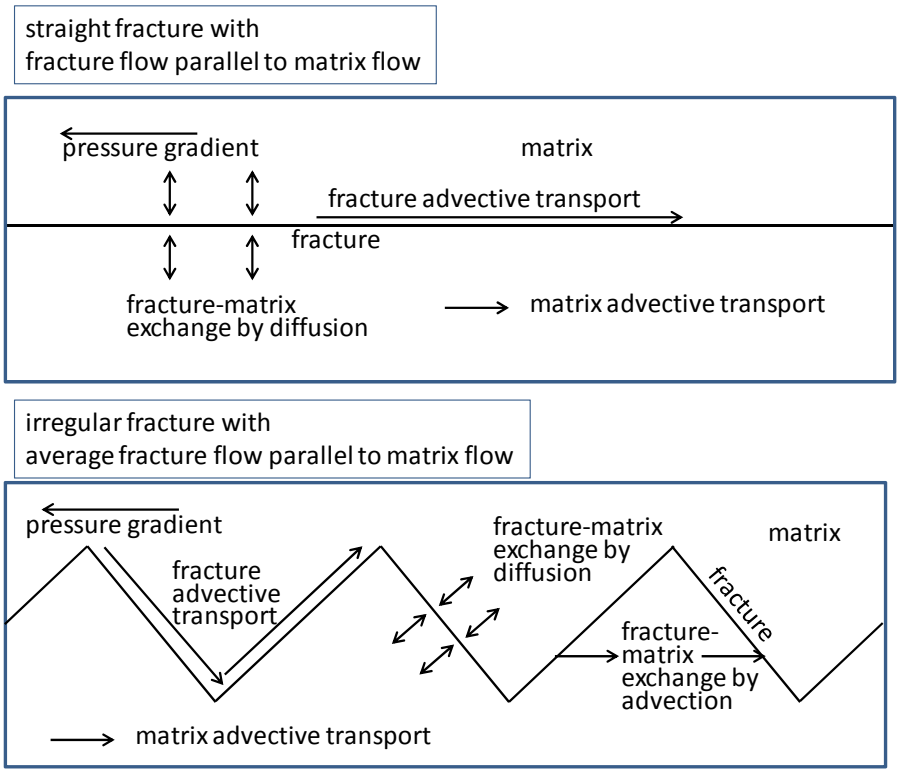

Figure 3-20. Conceptual diagrams for transport in a fracture-matrix system for a straight fracture and an irregular fracture.

Figure 3-19 also shows the effects of grid resolution on the results going from 1065 to 8081 nodes. These represent grid dimensions within the fine-gridded section on the order of 0.04 m for 1065 nodes to 0.006 m for 8081 nodes. The solution shows little sensitivity to grid refinement beyond 2127 nodes.

The comparison for irregular and straight fractures given above was done by comparing solute mass arrivals at positions that represent the same fracture path length for the two cases. This is

convenient for this comparison with single fractures, but not for scaling the effects of irregular fractures for a general fracture network problem. To utilize irregular fractures as a numerical approximation for straight fractures, the fracture properties must be scaled. The physical quantities that must be scaled are the fracture volume and the fracture-matrix interface area. These quantities need to be adjusted so that they are the same for an irregular fracture as for the corresponding straight fracture that the irregular fracture is intended to represent. This is done in the analytical model by reducing the fracture-matrix interface area reduction factor (A_r) and fracture porosity (ϕ_f) by the ratio of the irregular fracture path length to the straight fracture path length. Two examples are provided in Figure 3-21, where analytical model results using Equations (3-20), (3-21), and (3-22) are used to compute the cumulative mass arrival curves for two cases that have different fracture lengths, 4 m and 16 m, for the linear fracture problems discussed in Section 3.4.2.1. To arrive at the same cumulative mass-arrival curve for both cases, the fracture matrix area reduction factor is reduced from 1 to 0.25 and the fracture porosity is reduced from 0.0867 to 0.0217. The scaling is approximate because it is only valid for $v_{mz} \ll v_f$, although this is usually true for a fracture-matrix system.

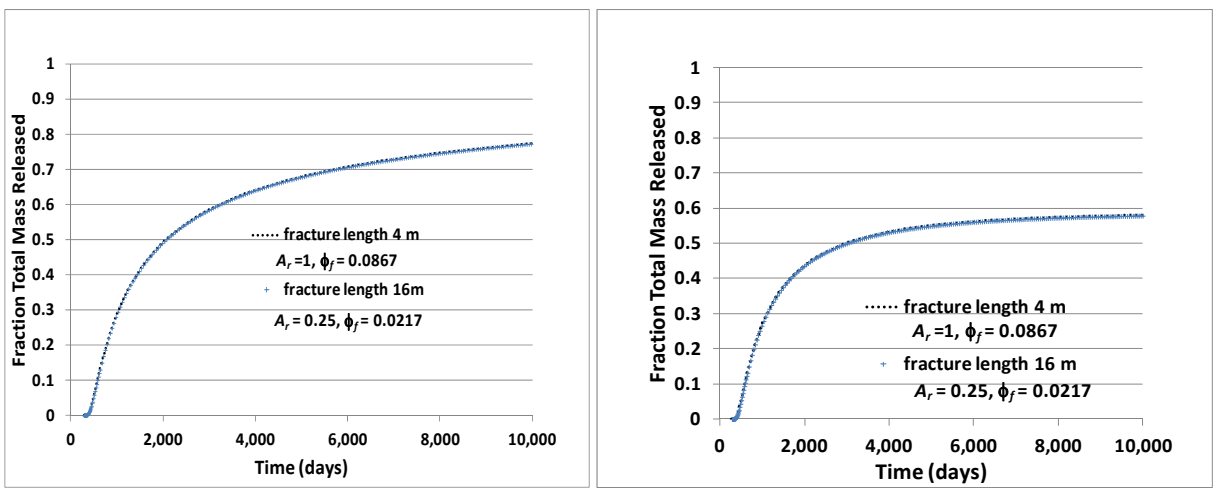

(a) (b)

Figure 3-21. Comparison of cumulative mass arrival scaling for different fracture lengths: (a) matrix flow parallel to fracture; (b) matrix flow at an oblique angle to fracture.

Other effects of an irregular fracture geometry cannot be scaled; Figure 3-19 provides an example of the discrepancy introduced by using an irregular fracture to represent a straight fracture. However, to the extent that fractures in nature have irregularities, these types of discrepancies are inherent in any model of a fractured, permeable rock that doesn't explicitly account for such irregularities.

3.5 Mechanical Damage Model using RBSN

Elastic response and fracture development is modeled by the mechanical-damage model based on the rigid-body-spring networks (RBSN). The RBSN is a special type of spring network that is based on the rigid-body-spring concept developed by Kawai (1978). The notable features of the RBSN are (1) geometry of the RBSN is defined by the Voronoi tessellation of the nodal points, and (2) the cell degrees of freedom are defined at the corresponding cell nuclei (i.e., Voronoi cell nodes). The method is elastically homogeneous under simple modes of straining and provides grid-insensitive representations of fracture. The information of this section summarizes some of the previous work (Bolander and Saito 1998; Berton and Bolander 2006; Asahina et al., 2011).

3.5.1 Model formulation

To provide a basic understanding of this modeling approach, an overview of the element formulation is given here. The geometry of a RBSN is defined by the dual Delaunay tessellation of the nodal points. The basic unit of a RBSN is a 1D lattice element (Figure 3-22) that consists of (1) a zero-size spring set that is located at the centroid of the Voronoi boundary; and (2) rigid arm constraints that link the spring sets and the nodal degrees of freedom (Fig. 3-22(c)). Each node has six degrees of freedom for the 3D case. The spring set is formed from three axial springs and three rotational springs as shown in Figure 3-22(c) (the rotational springs have been omitted for clarity). The axial and rotational springs are scaled in proportion to the distance between the element length, h_{ij}, and the area of the Voronoi cell boundary, A_{ij}, and assigned according to

$$k_s = k_t = \alpha_1 k_n = \alpha_1 \alpha_2 E \frac{A_{ij}}{h_{ij}}, \qquad k_{\phi n} = E \frac{J_p}{h_{ij}}, \qquad k_{\phi s} = E \frac{I_{ss}}{h_{ij}}, \qquad k_{\phi t} = E \frac{I_{tt}}{h_{ij}} \tag{3-23}$$

in which E is the elastic modulus, J_p, I_{ss}, and I_{tt} are the polar and two principal moments of inertia of the Voronoi cell boundary with respect to the centroid, respectively. By adjusting α_1 and α_2 in accordance with experimental results, macroscopic modeling of both elastic constants (E and Poisson ratio, ν) is possible. The relashionship between the generalized spring displacement, **d** (6×1 column vector), and the generalized nodal displacements in local coordinates, $\mathbf{u}_e$ (12×1 column vector), can be expressed by

$$\mathbf{d} = \mathbf{B}\mathbf{u}_e \tag{3-24}$$

where **B** is a 6×12 geometric transformation matrix:

$$\mathbf{B} = \begin{bmatrix} -\mathbf{I} & \mathbf{B}_{12} & \mathbf{I} & \mathbf{B}_{14} \\ \mathbf{0} & -\mathbf{I} & \mathbf{0} & \mathbf{I} \end{bmatrix}. \tag{3-25}$$

Submatrices $\mathbf{B}_{12}$ and $\mathbf{B}_{14}$ are defined by

$$\mathbf{B}_{12} = \begin{bmatrix} 0 & -z_C & y_C \\ z_C & 0 & -h/2 \\ -y_C & h/2 & 0 \end{bmatrix} \quad \text{and} \quad \mathbf{B}_{14} = \begin{bmatrix} 0 & z_C & -y_C \\ -z_C & 0 & -h/2 \\ y_C & -h/2 & 0 \end{bmatrix}, \tag{3-26}$$

where y_C and z_C are the distance between the centroid C and the intersection of the y- and z-axes and the Voronoi cell boundary, respectively (Fig. 3-22(b)). The element stiffnes matrix, $\mathbf{K}_e$, can be obtained by

$$\mathbf{K}_e = \mathbf{B}^T\mathbf{D}\mathbf{B}. \tag{3-27}$$

The material matrix, **D**, is expressed by

$$\mathbf{D} = (1 - \omega)\mathrm{diag}[k_s, k_t, k_n, k_{\phi n}, k_{\phi s}, k_{\phi t}], \tag{3-28}$$

where ω is a scalar damage index which ranges from 0 (undamaged) to 1 (completely damaged). In the classical brittle approach, which is applied to the studies presented in this report, ω is either 0 or 1. Nodal displacements, **u**, are obtained by solving the system equations

$$\mathbf{K}\mathbf{u} = \boldsymbol{\phi} \tag{3-29}$$

where **K** is the system stiffness matrix assembled from the element components and □ is the vector of nodal forces. The general structure (e.g., matrix dimensions) of the element stiffness matrix is same as those of the frame element, in which the stiffness matrix is assembled by the direct stiffness method. In fact, the matrix entries of a RBSN become identical to those of the frame element if a regular squre grid is used. At this stage of model development, a skyline form is used for the global stiffness matrix to economize the use of computer memory. The Crout elimination scheme is used to solve the system of equations.

In the RBSN approach, a Voronoi cell is considered as a rigid cell in the sense that it maintains its original shape during the course of loading and material deformation (assumption of small strain). The flexibility of the motion is lumped into the spring sets and Voronoi cell boundaries (e.g., Voronoi vertex) are not used for the mechanics; therefore, the separation or interpenetration of the cells are permitted.

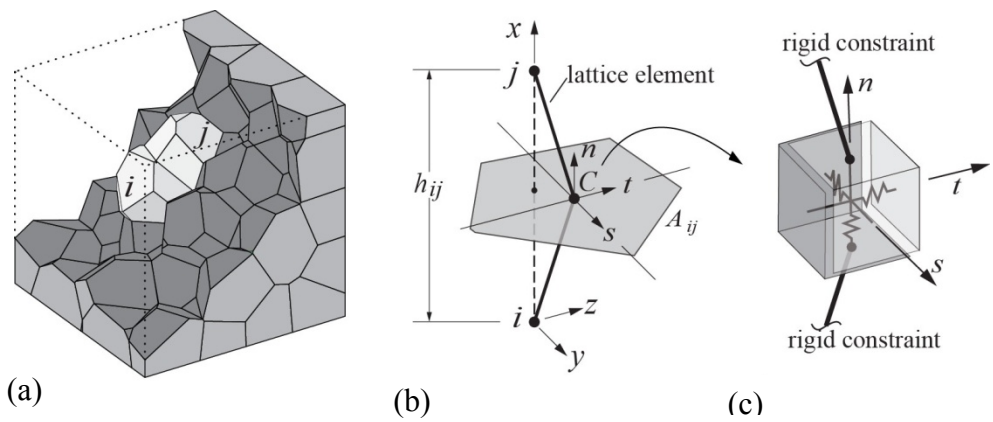

Figure 3-22. Typical lattice element *ij*: (a) within a Voronoi grid; (b) isolated from the network; and (c) a zero-size spring set (referenced to local coordinate axes *n-s-t*) located at centroid *C* of Voronoi cell boundary area A_{ij}.

3.5.2 Nodal stress calculation

The stress tensor at the Voronoi cell nodes can be calculated by considering the equilibrium conditions of the spring force. After solving the system equation (3-29), components of the spring force at the centroid of a Voronoi cell boundary can be obtained (Fig. 3-23(a)). Figure 3-23(b) shows local force components F_{nn}, F_{ns}, and F_{nt} for an arbitrary section of the cell (passing through the associated Voronoi cell node) with its corresponding local coordinates, *n-s-t*. Moment contributions to equilibrium are not considered here. Such local force components acting on the cell node can be calculated to satisfy equilibrium with the forces acting on all remained cell boundaries. By dividing these force components by the cut-face area, the corresponding stress components σ_n, σ_s, and σ_t can be obtained. By repeating this process for three mutually perpendicular sections, the full stress tensor is obtained (Fig. 3-23(c)). Details are given by Yip et al. (2005).

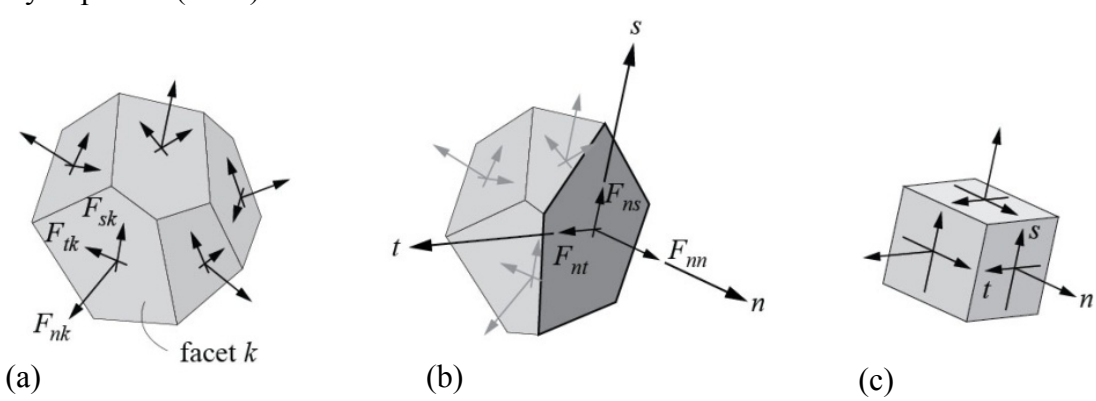

Figure 3-23. Stress tensor at Voronoi cell node: (a) components of spring force local coordinates; (b) a set of forces obtained by equilibrium; and (c) complete stress tensor at Voronoi cell node. Adapted from Yip et al. (2005).

3.5.3 Rigid-body-spring network requirements for compatibility with classical solid mechanics

3.5.3.1 Uniform stress-strain

Some basic properties of the RBSN are presented in this section for its application of modeling the elasticity and fracture of homogeneous materials (Asahina et al., 2011; Yip et al., 2005). Consider a cubic domain of dimension L that is subjected to uniform compressive loading, σ, in the vertical direction. A discretization of the computational domain and the direction of the loading are depicted in Figure 3-24(a). Appropriate boundary conditions are applied to ensure uniform compressive loading. Prior to cracking or other nonlinear behavior, a Mohr's circle representation of the stress state at each Voronoi cell node can be plotted using the nodal stress tensor calculations mentioned above for the *n-t* stress components. Due to the symmetry of the boundary condition, only the σ_n-σ_t pairs are plotted in Figure 3-24(b). A similar result can be produced for the *n-s* direction. For the case of $\alpha_1 = \alpha_2 = 1$, the model is elastically homogeneous with $\nu = 0$. Each of the darker dots represents the (σ_n, σ_t) stress pair results for all internal nodes for a particular inclination of the material element with respect to the loading direction. Relative errors of the nodal displacements are also estimated, where relative error is defined as

$$e_r = \frac{\|u-u^h\|_2}{\|u\|_2}, \quad \|u-u^h\|_2 = \sqrt{\sum_{i=1}^{N}(u(\mathbf{X}_i)-u^h(\mathbf{X}_i))^2}\ , \tag{3-30}$$

where $\|\cdot\|$ is the L_2 error norm, u and u^h are the exact and numerical solutions, respectively, and **X** is the nodal coordinates in loading direction, and N is the total number of nodes. The small relative error e_r=9.5×10^{-9} indicates the RBSN is elastically homogeneous under uniform modes of straining (to within algorithmic precision). As an example, a macroscopic Poisson ratio of ν = 0.17 is achieved by setting α_1 = 0.32 and α_2 = 1.56 in Equation (3-23). The stress pairs for this case, however, exhibit scatter about the theoretical solution. Although this form of artificial heterogeneity is undesirable, Berton (2003) determined that the RBSN model produces smaller errors that an ordinary lattice model.

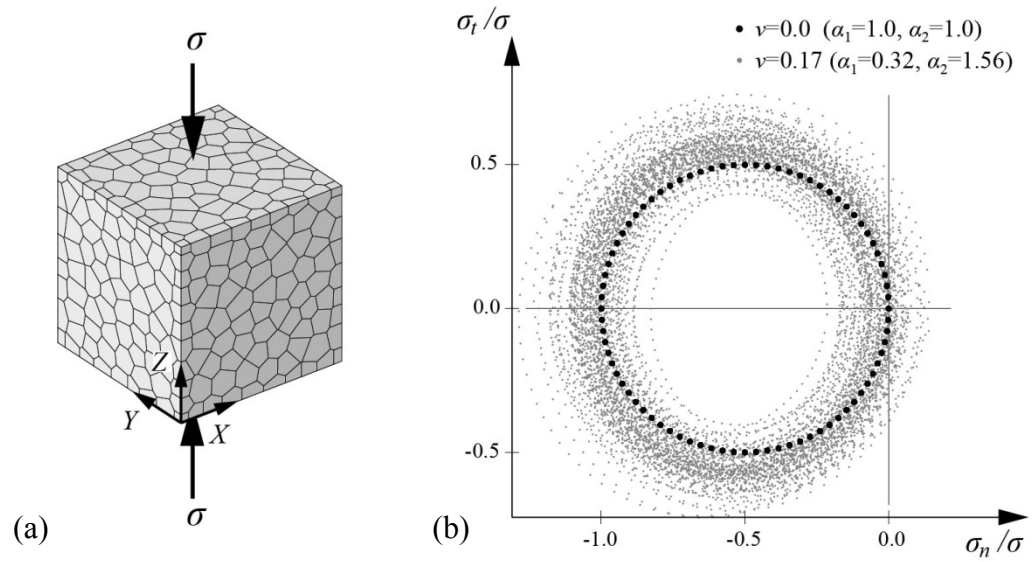

Figure 3-24. Tensoral stress calculation under uniaxial compressive loading: (a) Voronoi discretization of a cubic domain; (b) Mohr's circle representation of stress state at Voronoi cell nodes.

3.5.3.2 Fracture model

In RBSN modeling, fracture is represented by the breakage of the springs. Forces and/or displacements are applied incrementally with equilibrium iterations in each increment. Only one element is allowed to break per iteration. For each element *e* within the model, a stress ratio can be expressed by

$$\rho_e = \sigma_e / \hat{\sigma} \tag{3-31}$$

where σ_e is a measure of stress within element *e* and $\hat{\sigma}$ is a material strength. Element breaking occurs when $\rho_e > 1$. The most critical element undergoes fracture, which entails a reduction of its elastic stiffness and an associated release of element forces. As the fracture criteria of RBSN modeling, three approaches to select σ_e have been developed as follows.

Tensile stress measures

The RBSN has been applied to modeling fracture driven by predominately tensile loading (Berton and Bolander, 2006). In general, loading direction seldom coincides with the element axis *ij*; therefore, both the normal and tangential springs are activated. Under a tensile loading condition, a normal spring is in tension. The forces in the springs connecting neighboring cells at point C (Fig. 3-22(b)) are calculated for each iteration cycle. The resultant of the set of forces, $F_R = (F_n^2 + F_s^2 + F_t^2)^{0.5}$, is used to obtain a measure of tensile stress within each element

$$\sigma_R = F_R / A_{ij}^P \tag{3-32}$$

where A_{ij}^P is the projected area of A_{ij} on a plane perpendicular to F_R. This σ_R serves as σ_e in Equation (3-31), whereas $\hat{\sigma}$ varies according to a tensile softening relation. This uniaxial, vectorial stress approach to fracture within the RBSN is energy conserving and mesh insensitive for predominantly tensile stress fields. For example, Thomure et al. (2001) demonstrated the model objectivity with respect to size and geometry of the lattice network. A random mesh provides uniform, controllable energy consumption that yields practically the same results as a straight line discretization of the crack trajectory. However, complications arise when such uniaxial notions of stress are applied to modeling cases of multiaxial stress.

Maximum principal stress measures

Asahina et al. (2011) used the stress tensor to determine the failure of RBSN elements. As mentioned in Section 3.5.2, a complete set of the stress tensor can be obtained at the cell nodes. Whereas stress values at the nodes are useful for visualization purposes, stress values at the inter-element are needed for fracture simulation. Inter-element stresses are calculated according to

$$\bar{\boldsymbol{\sigma}} = (\boldsymbol{\sigma}_i + \boldsymbol{\sigma}_j)/2 \tag{3-32}$$

where $\boldsymbol{\sigma}_i$ and $\boldsymbol{\sigma}_i$ are the stress tensors at neighboring nodes i and j, respectively. Maximum principal tensile stress of $\bar{\boldsymbol{\sigma}}$ serves as σ_e in Equation (3-31). In this way, fracture under multiaxial stress conditions can be simulated. However, this approach does not readily account for the possibility of softening, since the stress at a given node is based on element forces from all connected elements.

Mohr-Coulomb criteria

The strength properties of elements are defined by a Mohr–Coulomb surface with a tension cut-off as shown in Figure 3.5-4. The fracture surface is defined by three parameters: surface inclination ψ with respect to the σ_n axis; surface intersection c with the shear axis; and the tensile strength, f_n, of the interface. Axial stresses are measured as $\sigma_I = F_I / A_{ij}$, where F represents axial spring force and index I corresponds to each of the n–s–t local axes (Fig. 3-22(b) and (c)), respectively. Figure 3-25 also shows the resultant of the axial stresses, $\overline{OP} = (\sigma_n^2 + \sigma_s^2 + \sigma_t^2)^{0.5}$, and the point, P_o, at which $\overline{OP}$ intersects the Mohr-Coulomb surface (or the tension cutoff surface). The determination of the critical stress ratio ρ_c (Equation (3-31)) is based on the measurement of $\rho = \overline{OP} / \overline{OP_o}$. At this stage in the model development, there is no option to soften the interface element or provide a frictional plateau for shear loading, even though test results indicate frictional resistance is maintained after interface strength is overcome in shear.

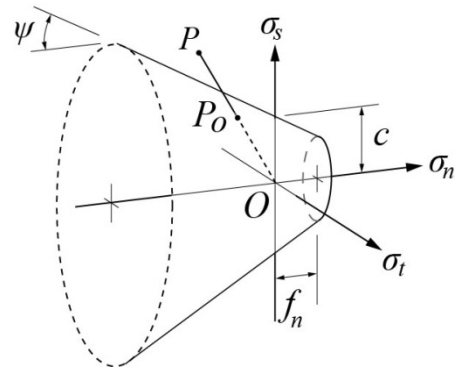

Figure 3-25. Mohr-Coulomb surface with tension cut-off.

3.6 Hydro-Mechanical Model using TOUGH2 and RBSN

3.6.1 Coupling through exchange of primary variables at each time step

TOUGH2 is coupled with RBSN to compute fracture damage development, as well as flow and transport through the fractured porous rock, accounting for dynamically changing THM conditions. The general procedure for the two-code coupling (hydraulic and mechanical code) is similar to the earlier work of Rutqvist et al. (2002) who linked TOUGH2 to a commercial continuum-mechanics simulator, FLAC3D. In this paper, TOUGH2 is used to simulate the hydraulic quantities (e.g., temperature, pressure, and saturation), while RBSN accounts for the mechanical quantities (e.g., stress, strain, displacement, and damage). Such primary variables are coupled through simplified linear relationships or through nonlinear empirical expressions, which could be estimated by laboratory experiments with appropriate calibration. The main advantage of coupling TOUGH2 and RBSN is that both models share the same unstructured, 3D Voronoi grid and the same set of nodes. This greatly simplifies the process of exchanging primary variables between two codes. At the current stage, TOUGH2 and RBSN are linked through an external coupling module, which transfers the relevant variables at each time step. It is assumed that the local changes of hydraulic variables produce strain as follows:

$$\Delta\varepsilon_T = \alpha_T \Delta T \tag{3-33}$$

$$\Delta\varepsilon_s = \alpha_s \Delta S \tag{3-34}$$

$$\Delta\sigma = (\Delta\varepsilon_T + \Delta\varepsilon_s)E \tag{3-35}$$

where ε_T is the thermal strain, ε_s is the shrinkage/swelling strain, ΔT and ΔS is the change in temperature and saturation over the time step in one lattice element, respectively, α_T is the coefficient of thermal expansion, α_s is the moisture swelling coefficient, and σ is the stress. The hydraulic variables, ΔT and ΔS, are taken as the average of two neighboring nodes i and j. At this stage of model development, hydro-mechanical coupling is based on one-way coupling, in which

flow processes affect mechanical strain but mechanical behavior does not affect flow parameters (e.g., permeability, porosity). Future work will include model developments for more general approaches, such as two-way coupling and a fully coupled poro-elastic model.

3.6.2 Model validation

3.6.2.1 Stress changes with imbibitions

Model description

The TOUGH-RBSN simulator is validated by comparison with an independent simulation of the same process using TOUGH-FLAC (Rutqvist 2011). Consider a soil sample (20×20×20 mm) which is wetted at the bottom and fully confined mechanically as shown in Figure 3.6-1. The model is discretized with 19 lattice elements and 20 nodes. Model boundaries are fully confined with mechanical fixed supports, and there is no flow across the boundaries except at the bottom water inlet. Both simulations were calibrated using data from an experiment that was a part of the international collaborative project DECOVALEX III. The experiment was conducted for about 10 days at isothermal condition (T=25°C). The initial saturation is 65% and the elastic modulus is 60 MPa. From this information, the moisture-swelling coefficient, α_s (Eq. 3), can be back-calculated to 0.238 as shown in Rutqvist et al. (2011).

Simulation results

Figure 3-26 shows the simulation results for time evolution of compressive stress and saturation. The hydraulic primary variables are accurately simulated by TOUGH2 as reported in Rutqvist et al. (2011). The stress increments are based on the saturation changes. The final stress is 5.12 MPa which consists of 5 MPa (calibrated value) on top of the initial atmospheric stress of 0.12MPa. Good agreement between the results simulated by TOUGH-RBSN and TOUGH-FLAC are obtained.

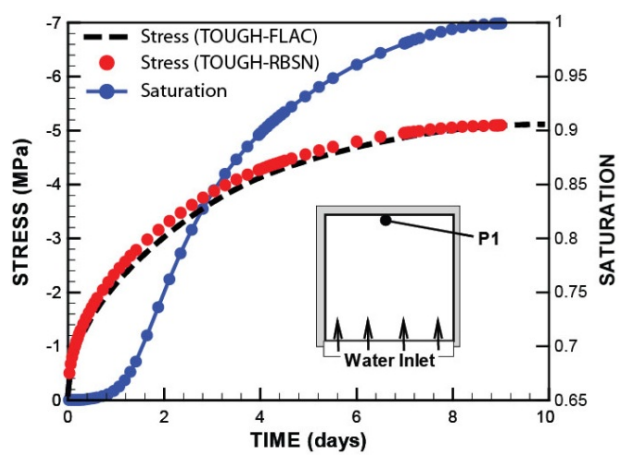

Figure 3-26. Time evolution of compressive stress and saturation at point P1 for simple swelling model.

3.6.2.2 Thermal-mechanical response around a circular opening

Model description

The thermal-mechanical process of the TOUGH-RBSN simulator is validated by comparison with an analytical solution. Consider a square, 2m×2m, 2D domain with a circular opening (a radius of 0.075 m) at the center (Fig. 3-27). The domain is subjected to a far-field compressive stress, σ_x=15 MPa in the horizontal direction and σ_y=10 MPa in the vertical direction. The constant temperature at the boundary of the circular hole and the square domain is set to T_a = 90°C and T_b = 0°C, respectively. The elastic modulus, E, is 50 GPa and Poison ratio, ν, is 0.17. The thermal conductivity coefficient is 1.0 $W \cdot m^{-1} \cdot K^{-1}$ and volumetric thermal expansion coefficient, α_T, is 1×10^{-6} $^{\circ}C^{-1}$. The model parameters and model set up are partly taken from Li et al. (2012). A discretization of the computational domain and boundary conditions are depicted in Figure 3-27(a). The areal density of nodal points (or Voronoi grid size) can be controlled by changing l_m, a minimum allowable distance between nodes (Sec. 3.3-1), as function of spatial coordinates. A theoretical solution of the stress components (in polar coordinate system), induced by temperature changes, at any location within the domain is given by

$$\sigma_r^T = \frac{\alpha_T E}{1-\nu}\frac{T_a - T_b}{2\ln(b/a)}\left[-\ln\frac{b}{r} + \frac{a^2}{b^2-a^2}\left(\frac{b^2}{r^2}-1\right)\ln\frac{b}{a}\right] \tag{3-36}$$

$$\sigma_\theta^T = \frac{\alpha_T E}{1-\nu}\frac{T_a - T_b}{2\ln(b/a)}\left[1-\ln\frac{b}{r} - \frac{a^2}{b^2-a^2}\left(\frac{b^2}{r^2}+1\right)\ln\frac{b}{a}\right] \tag{3-37}$$

where a is the radius of the circular opening, b is the half length of the square domain, and r is the distance from the center of the domain to an arbitrary point of measurement. The elastic properties, ν and E, can be adjusted by changing α_1 and α_2 in Equation 3-23. The values of α_1 and α_2 are calibrated with a uniform tension test using an irregular grid. For this example, α_1 = 0.32 and α_2 = 1.56 are used for ν = 0.17.

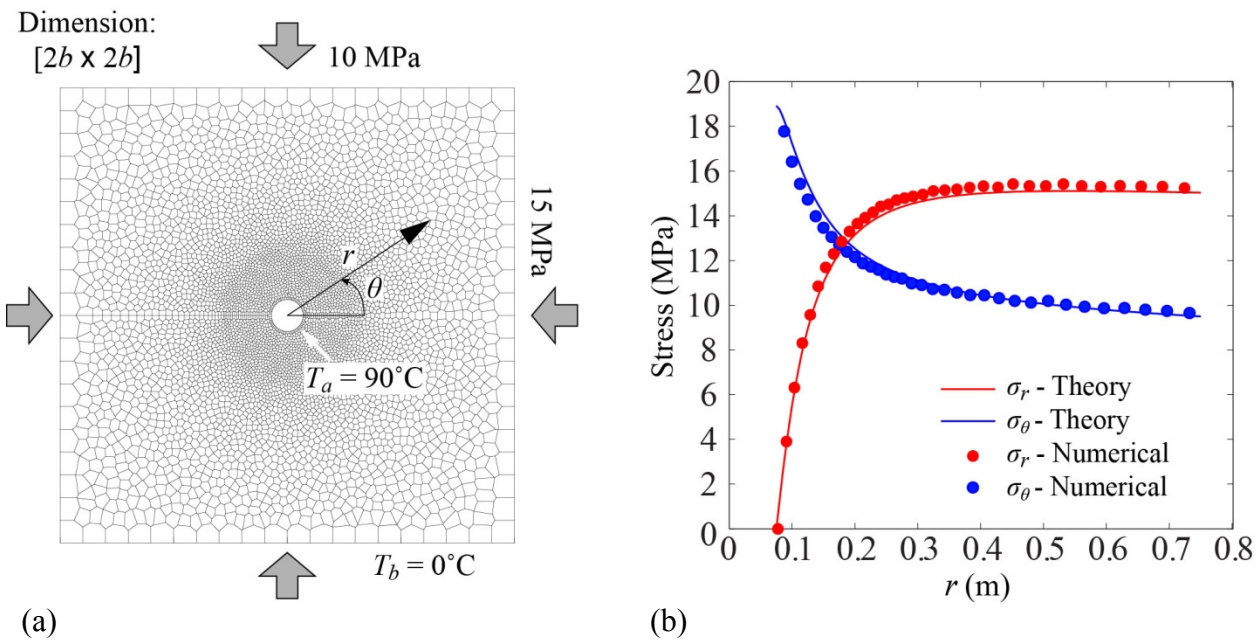

Figure 3-27. (a) Computational grid used for the TOUGH-RBSN simulator; and (b) simulation results of radial and tangential stresses for $\theta = 0$ and 2π, respectively, versus the distance from the center of the domain.

Simulation results

Figure 3-27(b) shows the simulation results of the stress profiles versus the distance from the center of the domain. Good agreement is obtained between the analytical solutions and the results simulated by the TOUGH-RBSN simulator.

3.6.2.3 Desiccation cracking

Dessication cracking is computed using the TOUGH-RBSN simulator to demonstrate its capabilities regarding hydro-mechanical coupled processes with fracture development. A slab structure is subjected to drying from the top surface. The saturation changes induce shrinkage strain and eventually elements break due to tensile stress. 2D models are first used to study basic aspects of fracture patterns in such conditions. Thereafter, the numerical simulations are conducted for 3D models to address the limitation of representing fracture processes in 2D models. The effects of boundary conditions and model dimensions to general fracture patterns are investigated.

2D simulations

Consider a 2D slab model subject to drying from the top surface. Figure 3-28(a) shows a discretization of the slab structure of dimension 10mmx100mm. The initial saturation is set to 80%. The convective boundary condition is implemented by a thin layer of nodes at the top surface with prescribed nodal saturation (30%). Two mechanical boundary conditions are

employed: 1) fixed at one node (associated Voronoi cell is colored in black) to avoid rigid movement, and 2) fixed at the bottom surface, whereas the vertical surfaces are only free to move in-plane.

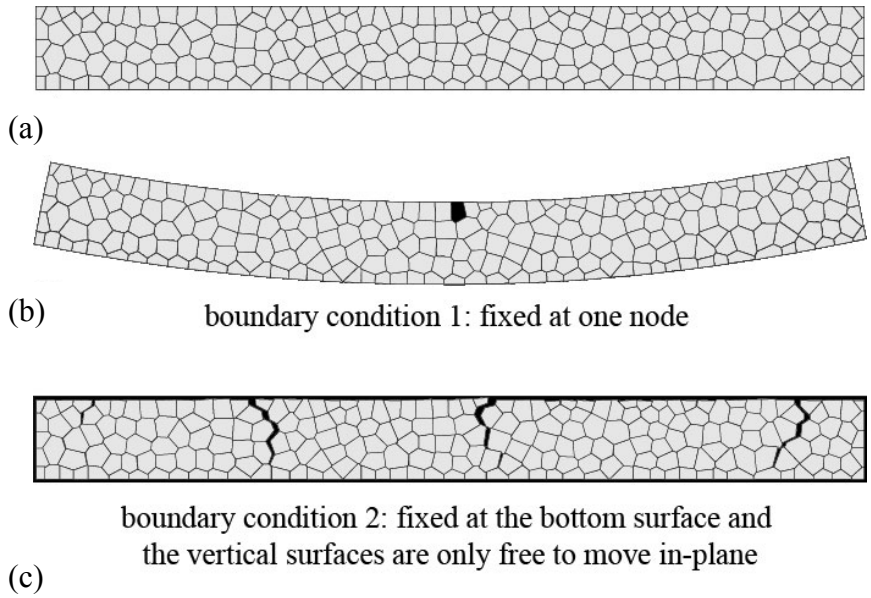

Figure 3-28. 2D Voronoi grid of slab structure (297 nodes) drying from top surface: (a) undeformed configuration; (b) deformed shape with the first boundary conditions; and (c) fracture pattern with the second boundary conditions.

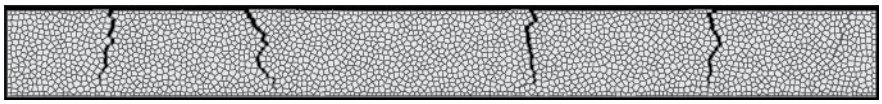

Figure 3-29. Fracture pattern with fine mesh (2680 nodes).

The vapor diffusion induced by saturation changes induces changes in strain within the mechanical element. In general, elements closest to the top surface shrink the most due to the largest changes in saturation. The model is parameterized using hydrogeological and mechanical properties characteristic of clay rock. Here, a classical brittle approach is used to break the lattice elements. The simulation is conducted until the crack pattern is fully developed. For the sake of visualization, the background of the model is colored with black if fracture occurred. The facets of the fractured elements portrayed in following figures do not represent any roughness properties of the fracture surface.

Figure 3-28 b) and Figure 3-28 c) shows the deformed shape of slab due to the first and second boundary conditions, respectively. It is clearly seen that the deformation patterns are dependent on the boundary condition. The insensitivity of the fracture pattern with respect to mesh size is studied using two different meshes with 297 nodes (Fig. 3-28(c)) and 2680 nodes (Fig. 3-29).

The results show about the same number of major crack features as well as the similar spacing between the cracks. The basic aspect of fracture patterns is further studied for various slab thicknesses as shown in Figure 3-30. Model thicknesses of 10mm (Fig. 3-28(c)), 20 mm, 40 mm, and 80 mm are simulated. The resulting number of major cracks is about 4, 2, 1, and 1, respectively. This general response, in which the distance between cracks increases with material thickness, has been observed in experiments (Colina and Roux, 2000). The same number of cracks is developed for the cases having thicknesses of 40 mm and 80 mm. This is partly because the corresponding distance between cracks exceeds the lateral length of the model at some point between the 20 mm case and the 40 mm case.

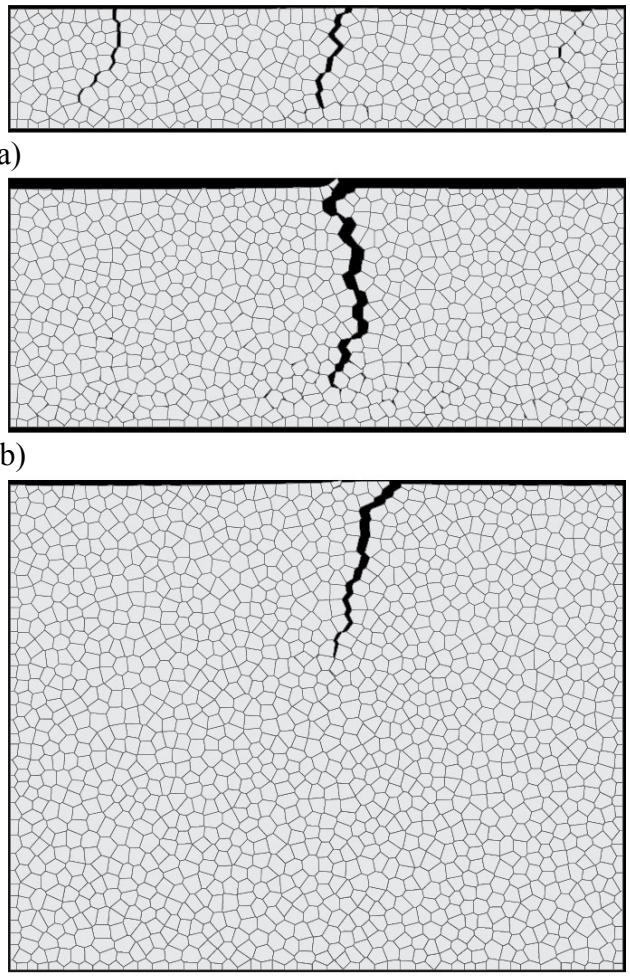

Figure 3-30. Fracture pattern with various thicknesses: (a) 20mm; (b) 40mm; and (c) 80mm.

3D simulations

A 3D computational grid is used to address the importance of using a 3D framework for studying fracture development. The slab thickness is 20 mm and the area is 100 mm × 100 mm. The same initial conditions and the second boundary conditions which are used for 2D case above are applied here. The process of shrinkage cracking is shown in Figure 3-31.

As shrinkage strain increases, the RBSN elements at the top surface are subjected to the in-plane movement. Early in the fracture stage (Fig. 3-31(b)), the elements at the top surface undergo fracture at almost the same time. The fracture pattern forms isolated patches due to uniform straining based on the homogeneity of the material. As the time step increases, the number of patches increases (Fig. 3-31(c)) and cracks develop in the vertical direction (perpendicular to the paper surface) followed by the drying process in deeper regions. At the later stage, when the fracture developments are stabilized, some of the fractures tend to seal and larger patches are eventually formed (Fig. 3-31(d)). The arrows in the figure indicate the location of the sealing behavior that occurred. Overall, the isolated patches simulated by the TOUGH-RBSN simulator capture the similar patterns of fracture that can be seen in clay-rich geomaterials (Figure 3-32).

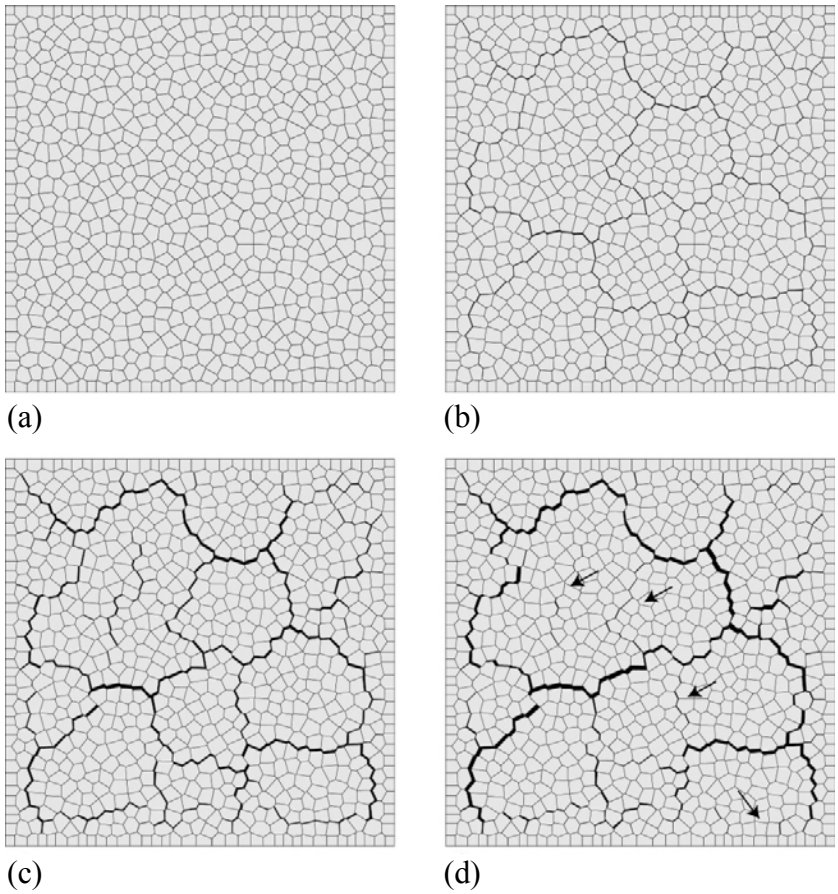

Figure 3-31. Evolution of shrinkage cracking in plan view (4802 nodes): (a) initial configuration; (b) early stage; (c) intermediate stage; and (d) late stage.

Figure 3-32. Drying surface of clay-rich geomaterial during dry seasons.

The fracture pattern for variable slab thicknesses in 3D is also studied. Figure 3-33 shows the fracture pattern of two different thicknesses 20 mm and 40 mm. As seen in the simulation results for 2D, the distance between fractures increases as the thickness increases. Bolander et al. (2007) have conducted a similar study for cement composite materials, where lattice-type models are used to calculate both mechanics and transport (e.g., moisture transport). Future work for desiccation cracking will involve more realistic simulations and quantitative comparisons with experimental data.

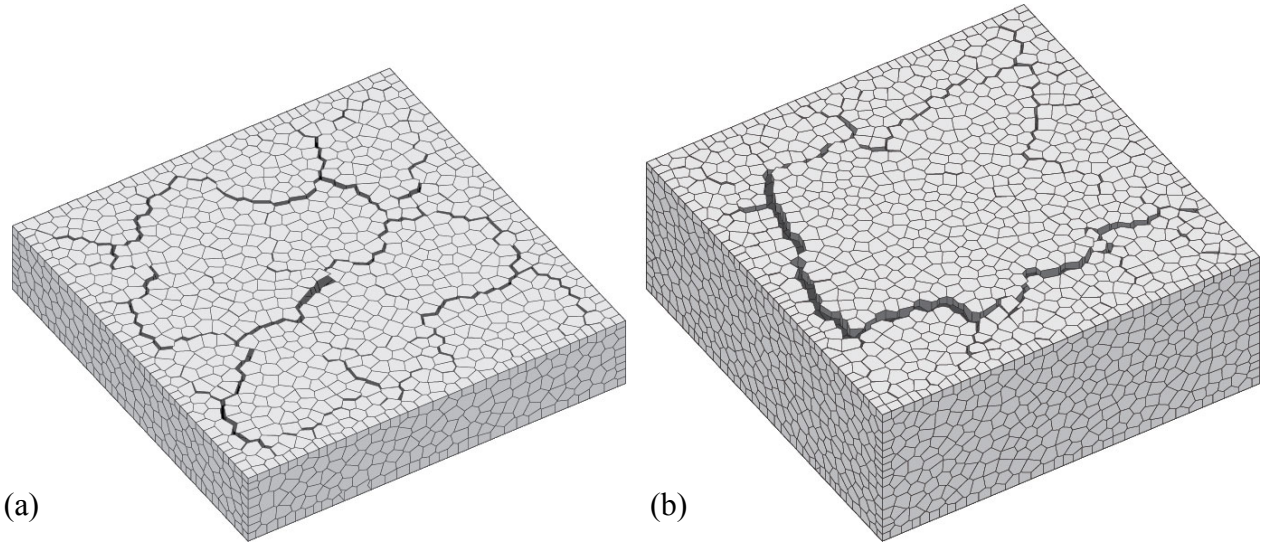

Figure 3-33. 3D view of fracture pattern with various thicknesses: (a) 20mm; and (b) 40mm.

3.7 Conclusions

Computational methods are needed to address fracture initiation and propagation as a THM coupled process. The method reported here uses a finite volume method for flow processes and the RBSN model for geomechanics. This allows for the coupling to be computed on a common

grid using a random Voronoi gridding approach for two or three dimensions. The proposed methodology in which fractures are placed along Voronoi cell boundaries eliminates many issues regarding incorporating new fractures into a numerical grid, minimizing computational aspects associated with regridding. This allows for a more practical incorporation of fracture initiation and propagation into numerical models of coupled THM processes.

A Voronoi gridding method is developed here for use both in geomechanical and fracture-damage models as well as for hydrogeologic flow and transport models. Voronoi grids are used to represent the rock mass (matrix) and fractures are inserted into the grid along Voronoi grid interfaces. The irregular Voronoi interfaces are used to approximate fracture paths by placing a fracture node at the midpoint of the Voronoi cell interfaces for fracture-matrix exchange, and fracture nodes at the Voronoi vertices where fractures intersect to control the fracture flow geometry, such that it moves along the Voronoi interfaces.

A hydrogeological model for discrete fractures in a rock matrix is presented. To validate this model, an analytical flow and transport model is developed for simple cases involving a single fracture and rock matrix. The model allows for both fracture and matrix flow, including matrix cross-flow relative to the fracture. Close comparisons are found for the numerical and analytical models. Flow and transport in an irregular fracture based on a random Voronoi grid is also analyzed, in which the average matrix flow is parallel to the average fracture direction. The results indicate that matrix cross flow causes a slight enhancement of transport rates for the irregular fracture as compared with a straight fracture. Scaling rules are developed for flow and transport that to account for the main effects of increased fracture path length associated with an irregular fracture network as compared with a straight fracture network.

A geomechanical and fracture-damage model is developed here using the Rigid-Body-Spring-Network (RBSN) numerical method. This method has been developed and applied to engineered materials over the past 35 years, and has been implemented here for use in THM coupled processes in geologic materials. The RBSN model has been shown to produce realistic results in terms of basic elastic behavior as well as fracture damage processes.

The coupled TOUGH-RBSN model is used to compute hydrological and elastic geomechanical responses when subjected to saturation-induced hydro-mechanical strain and thermal-mechanical strain. The model results are found to be in good agreement with independent numerical and analytical solution methods for the two validation cases investigated. Fracture development and propagation is examined with the TOUGH-RBSN model for conditions of dessication cracking, which are known to occur in saturation-induced, hydro-mechanically sensitive materials such as clay. The initiation and propagation of fractures is investigated in terms of different mechanical boundary conditions, grid resolution, dimensionality, and domain size. Qualitative agreement is found with results from other investigators and observations of dessication cracking in clay materials.

4. THM Modeling of the FE Experiment at the Mont Terri Site

4.1 FE Experiment at the Mont Terri Site

The Full-Scale Emplacement Experiment (FE) at the Mont Terri URL, Switzerland will be one of the largest and longest-duration heater tests worldwide (Figures 4-1 through 4-3). This heater experiment is undertaken by NAGRA and other international partners as an ultimate test for the performance of geologic disposal in Opalinus clay, with focus on both the EBS components and the host-rock behavior. The experiment will provide data useful for the validation of THM coupling effects regarding the processes in the host rock, while correctly accounting for (and examining) the conditions in the emplacement tunnel (temperature, saturation, and swelling pressure). Due to the 1:1 scale of the experiment, it will be possible to achieve realistic temperature, saturation, and stress gradients. It will also be possible to test backfilling technology with granular bentonite, as well as lining technology with shotcrete, anchors, and steel rips. Processes examined in the test cover many aspects of repository evolution, such as EDZ creation and desaturation of the EDZ during tunnel excavation and operation (including ventilation for about one year), as well as reconsolidation of the EDZ, resaturation, thermal stresses, and thermal pore-pressure increase after backfilling and heating (heating and monitoring period > 10 years).

As shown in Figures 4-1 through 4-3, the FE experiment will be conducted in a side tunnel at Mont Terri, excavated along the claystone bedding planes for this purpose, which is 50 m in length and about 2.8 m in diameter.

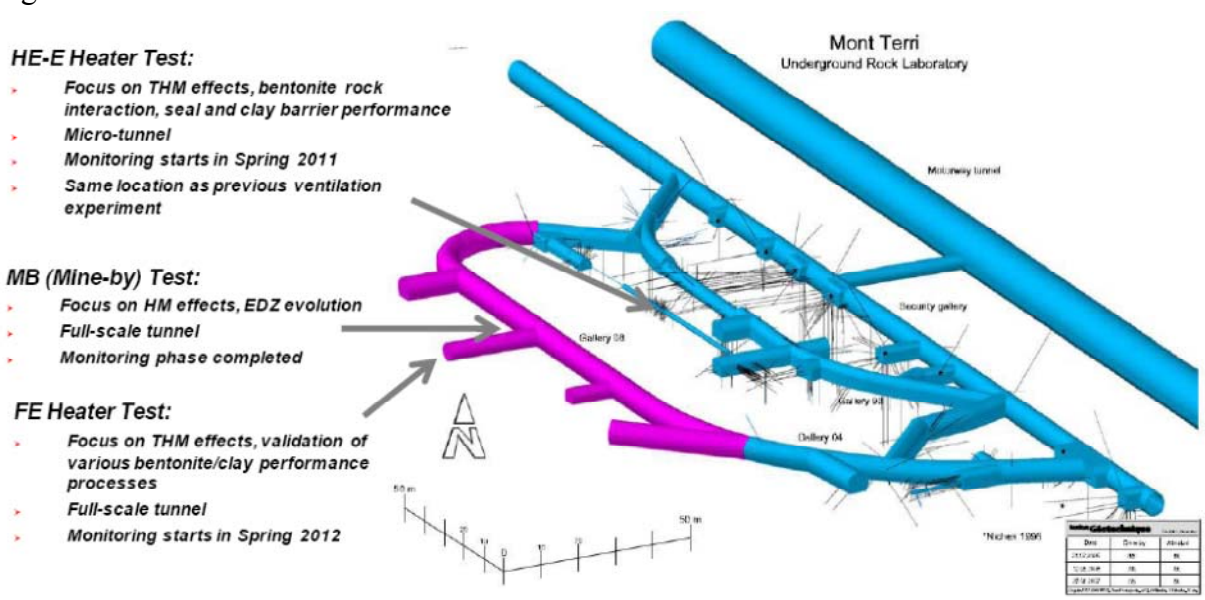

Figure 4-1. Summary schematic of the Mont Terri URL with side galleries and drifts for testing. Three specific experiments of relevance to UFDC are highlighted (based on Garitte, 2010).

Heating from emplaced waste will be simulated by three heat-producing canisters of 1500 W maximum power. A sophisticated monitoring program is planned, including dense pre-instrumentation of the site for *in situ* characterization, dense instrumentation of bentonite buffer and host rock, and extensive geophysical monitoring (seismic and electric tomography). A THM modeling program will be conducted in parallel with the testing and monitoring activities.

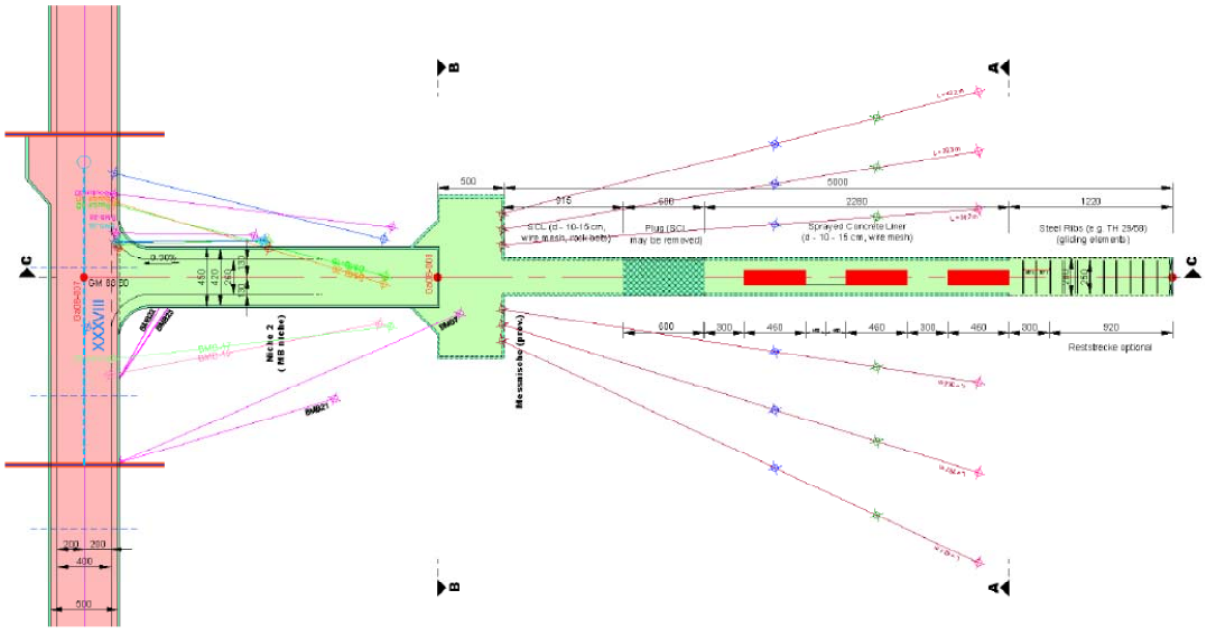

Figure 4-2. Plan view of experiment setup and borehole layout (from Garitte, 2010).

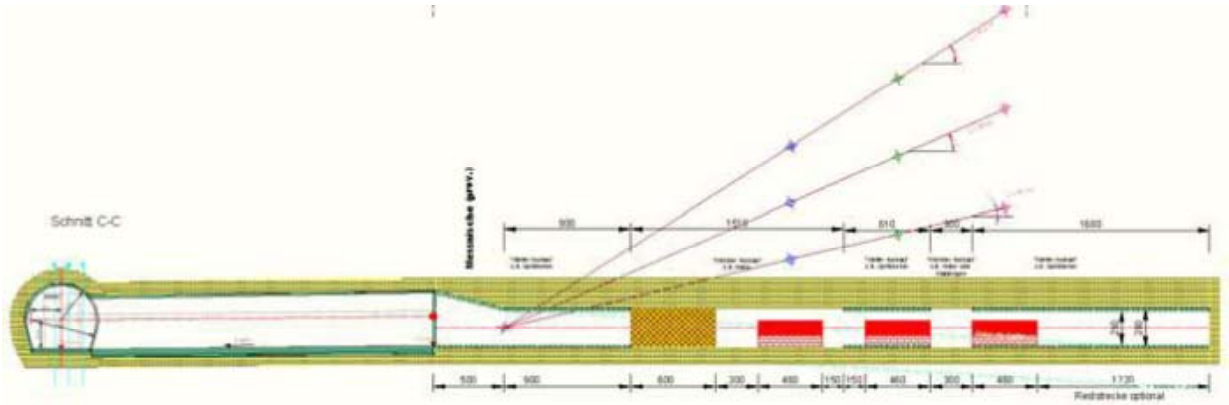

Figure 4-3. Side view of experiment setup and borehole layout (from Garitte, 2010).

Figure 4-4 shows the FE experiment time frame (Vietor, 2012). A niche in front of the FE tunnel was constructed in 2011, followed by a first phase of instrumentation of the rock mass

surrounding the tunnel using boreholes from the niche. The FE tunnel is currently being excavated by road-header, and this activity will be followed by another phase of instrumentation. After tunnel excavation, the tunnel will stay open for about 1 year under ventilation. This is followed by the emplacement of the heaters, bentonite buffer, and a concrete plug, after which the heating is expected to start at the end of 2014. The heating is then expected to go on for at least 15 years, with continuous monitoring of THM processes in both the bentonite buffer and surrounding rock.

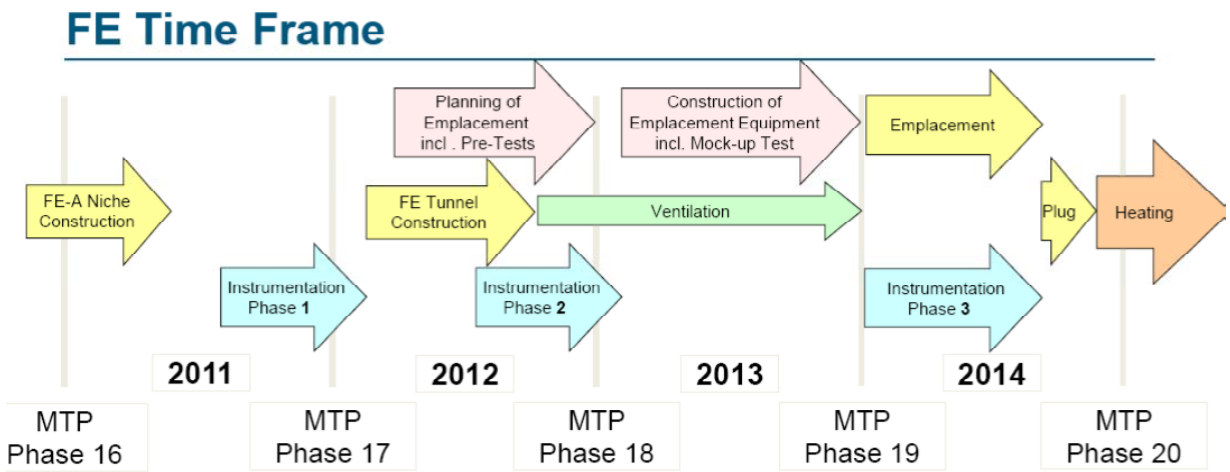

Figure 4-4. FE experiment time frame. Phases 16 to 20 refer to Mont Terri project phases (Vietor, 2012).

DOE is one of the experimental partners of the FE heater experiment, and LBNL is one of the modeling teams. A modeling kick-off meeting was held at Mont Terri on February 9, 2012, and a telecom webinar between NAGRA and FE modeling teams was held on May 24, 2012, to determine the plans for the THM modeling program. The plan is to start with calculation of the FE heater test, in which each modeling team develops their conceptual models and material properties using available literature (papers and reports) on lab experiments and previous Mont Terri *in situ* tests, etc. Later, this will be complemented with a restricted benchmark test for code comparison, in which properties and model geometry are set by NAGRA. Currently, LBNL is working on the preliminary modeling of the FE experiment, using the TOUGH-FLAC software; the results are to be presented at the next FE modeling group meeting to be held in Germany in November 2012.

4.2 Modeling approach

LBNL's model simulations of the FE experiment are carried out using the TOUGH-FLAC software (Rutqvist et al. 2002; 2011), which is based on linking the TOUGH2 multiphase flow and heat transport simulator (Pruess et al. 2011) with the FLAC3D geomechanical simulator (Itasca, 2009). The TOUGH-FLAC simulator has in recent years been extended and applied to

issues related to nuclear waste disposal in clay host rocks in bentonite backfilled tunnels (Rutqvist et al., 2011; 2012). This includes implementation of the Barcelona Basic model (BBM), for the mechanical behavior of unsaturated soils and applied for modeling of bentonite back fill behavior (Alonso et al. 1990). For the modeling of the FE experiment, we are developing the initial conceptual model and modeling approach, based on experiences from recent design scoping calculations conducted by teams contracted by the NAGRA, to help with the experimental design:

1) Pöyry (Engineering and Consulting): Modeling for excavation design using FLAC3D with ubiquitous joint model (anisotropic plasticity with different shear strength along bedding planes). This modeling approach was used to analyze the ground-support design (Nater, 2012).
2) CINEMAT and UPC of Spain conducted scoping calculations for thermal and monitoring design using the CODE-Bright FEM code; they used the BBM for modeling bentonite mechanical behavior (Garitte and Gens, 2012).
3) The Intera Swiss Branch performed 3D TOUGH2 model simulations with anisotropic properties and inclined mesh. Their modeling was limited to thermal-hydrological processes (no mechanics) and done for thermal and monitoring design (Ewing and Senger, 2011).

Our modeling approach will contain important components from these three models. The host rock will be modeled using TOUGH-FLAC, with anisotropic properties related to the beddings of the Opalinus clay. The beddings across the FE tunnel can be seen in Figure 4-5. The beddings are oriented with their strike along the tunnel axis and dipping about 45°. To accurately model anisotropic thermal and hydrological behavior, we will create an inclined TOUGH2 mesh, using the same procedure as the INTERA team. Anisotropic mechanical material behavior will be simulated using the FLAC3D ubiquitous joint model, with initial properties of those derived from the excavation design analysis by the Pöyry team (Nater, 2012). For the bentonite, we will start with the BBM model as applied by the CINEMAT and UPC (Garitte and Gens, 2012), and derive specific input material parameters for the MX-80 bentonite pellets that will be used when emplacing bentonite buffer around the heaters. With this modeling approach, we will be able to simulate THM processes in both the bentonite and host rock, and their interactions.

Figure 4-5. View of FE tunnel face from the FE niche showing beddings dipping 45° (Vietor, 2012).

4.3 FE Model Setup

Figure 4-6 presents numerical grids that are used for a model inception, using a relatively coarse mesh that will be refined in future simulations. With this model inception, we will test two different, alternative model meshes, and explore the model-size requirements over the course of the FE experiments, which are expected to run for up to 20 years. We first made an initial scoping calculation using the TOUGH2 code without geomechanics to study the thermal and hydrological behavior. The initial conditions for the model simulation are 2 MPa in pore fluid pressure and 15°C in temperature for the host rock. The 2 MPa of pore pressure is not under hydrostatic conditions, and the process is affected by the existing tunnel system at the site. In our simulations, we first ran a simulation with an open tunnel at the atmospheric pressure for 1 year, creating a pressure drop and hydraulic gradient around the tunnel. Potential desaturation caused by ventilation effects will be considered in future simulations. Thereafter, we assume instantaneous emplacement of the heater and buffer and start our heating simulation.

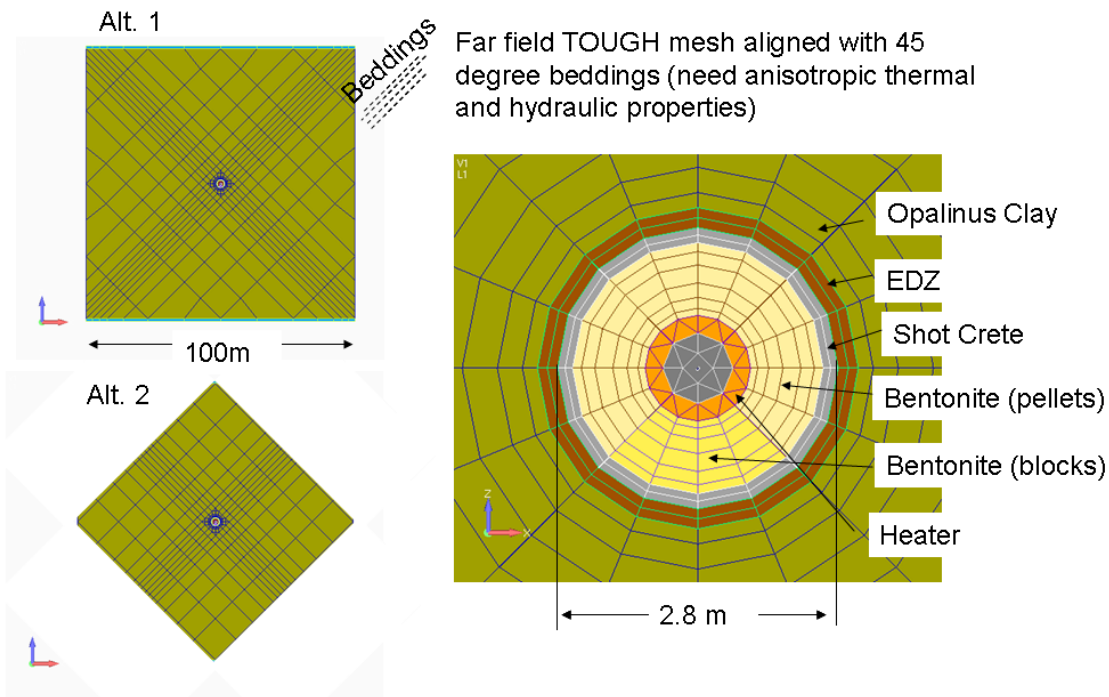

Figure 4-6. TOUGH-FLAC numerical grids for model inception.

The output from each of the heaters will be approximately 1500 W according to the specifications set by NAGRA. In our simulation, we assumed a constant heat output of 1500 W per canister and calculated an average line thermal load of 197 W/m. However, the heater power may be regulated to achieve a desired temperature evolution. For example, the targeted maximum temperature at the heater/bentonite interface is 125 to 135°C. On the other hand, a preliminary model simulation by the UPC team indicates that the temperature might not exceed 110°C, if the initial bentonite saturation is about 20 to 25%. A much higher peak temperature was calculated by the INTERA when assuming an initial saturation of 1%. Since buffer thermal conductivity depends on water saturation, the 1% initial saturation leads to a lower thermal conductivity in the buffer, which in turn results in a relatively high temperature at the heater/bentonite interface. A 1% saturation is reasonable for the pellets being deposited into the tunnel during buffer emplacement. However, experience from the ongoing HE-E heater test at Mont Terri shows that the bentonite pellets quickly draw moisture from the air and equilibrate with air relative humidity. Therefore, the initial buffer saturation of 18% is a reasonable value for the modeling.

The basic material properties used for the base-case TH model are contained in Table 4-1.

Table 4-1. Parameters for the Opalinus and Bentonite clay

Properties	Parameters	Symbol	Opalinus clay	Bentonite	Unit
Physical	Grain density	ρ_g	2.7×10^3	2.7×10^3	kg/m^3
	Porosity	$\varnothing$	0.15	0.389	-
	Pore compressibility	β	1.0×10^{-9}	5.0×10^{-8}	Pa^{-1}
Hydraulic	Intrinsic permeability	k	5.0×10^{-20}	2.0×10^{-21}	m^2
	Liquid relative permeability	n	-	3	-
	Capillary curve	P_0	1.47×10^7	2.00×10^7	Pa
	Capillary curve	λ	0.595	0.51	-
	Capillary curve	S_{ls}	1.0	1.0	-
	Capillary curve	S_{lr}	0.01	0.00	-
Thermal	Thermal conductivity (wet)	λ_{sat}	2.0	1.3	W/m/K
	Thermal conductivity (dry)	λ_{dry}	2.0	0.3	W/m/K
	Grain specific heat	C	900	800	J/kg/K
Mechanical	Bulk modulus	K	4170	20	MPa
	Shear modulus	G	1920	6.67	MPa
	Cohesion	C	5	-	MPa
	Friction angle	ϕ	25	-	°
	Thermal exp. coeff.	α_T	1.0×10^{-5}	$1.5\cdot10^{-4}$	1/°C
	Dilation angle	d	10	-	°
	Tensile strength	T	1.0	-	MPa
	Joint cohesion	C_J	2.2	-	MPa
	Joint friction	ϕ_J	23	-	°
	Joint tensile strength	T_J	0.5	-	MPa
	Joint dilation angle	d_J	10	-	°

We started with bentonite properties, including the thermal and hydraulic properties, derived from laboratory experiments and *in situ* tests related to the FEBEX experiment at Grimsel, Switzerland (Rutqvist et al., 2011). We then modified some of the properties to represent a bentonite buffer composed of MX-80 pellets. In our initial modeling, we also consider the water retention curves for the bentonite and Opalinus clay as important parameters for behavior. The capillary curves used in the model are shown in Figure 4-7. We use the van Genuchten formulation to describe the water-retention characteristic curves (van Genuchten, 1980):

$$P_c = -P_0\left[\left(\frac{S_l - S_{lr}}{S_{ls} - S_{lr}}\right)^{-1/\lambda} - 1\right]^{1-\lambda}$$

where P_0 is the air entry pressure, S_l is water saturation, the subscripts ls and lr refer to the fully saturated and residual conditions, respectively, and λ is a curve fitting parameter. These values are presented in Table 4-1. Those for the Opalinus clay are taken from the previous simulation and fit against a series of laboratory and *in situ* measurements (Garitte et al., 2012), and those for

bentonite clay are adjusted to match an *in situ* measurement of the initial state at the Mont Terri site (approximately 100 MPa at water saturation of 20%).

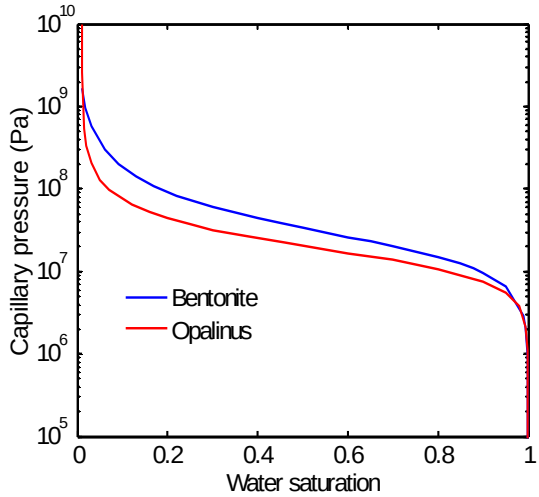

Figure 4-7. Capillary curves for bentonite and Opalinus clays.

4.4 Base-Case TH Simulation

The TH model simulation shows that the canister surface temperature peaks at approximately 94.5 °C after 4.8 years (Figure 4-8 (a)), and the temperature at the buffer and concrete interface reaches the maximum of 69 °C after 20 years. This peak temperature is lower than that obtained by Garitte and Gens (2012). The reason might be that (1) we used a 2D geometry with average thermal line load,(2) our bentonite properties are not yet firmly determined for pellets and might be different, or (3) we had a faster resaturation of the buffer, since we have not yet considered the drying of the rock mass during ventilation of the open drift.

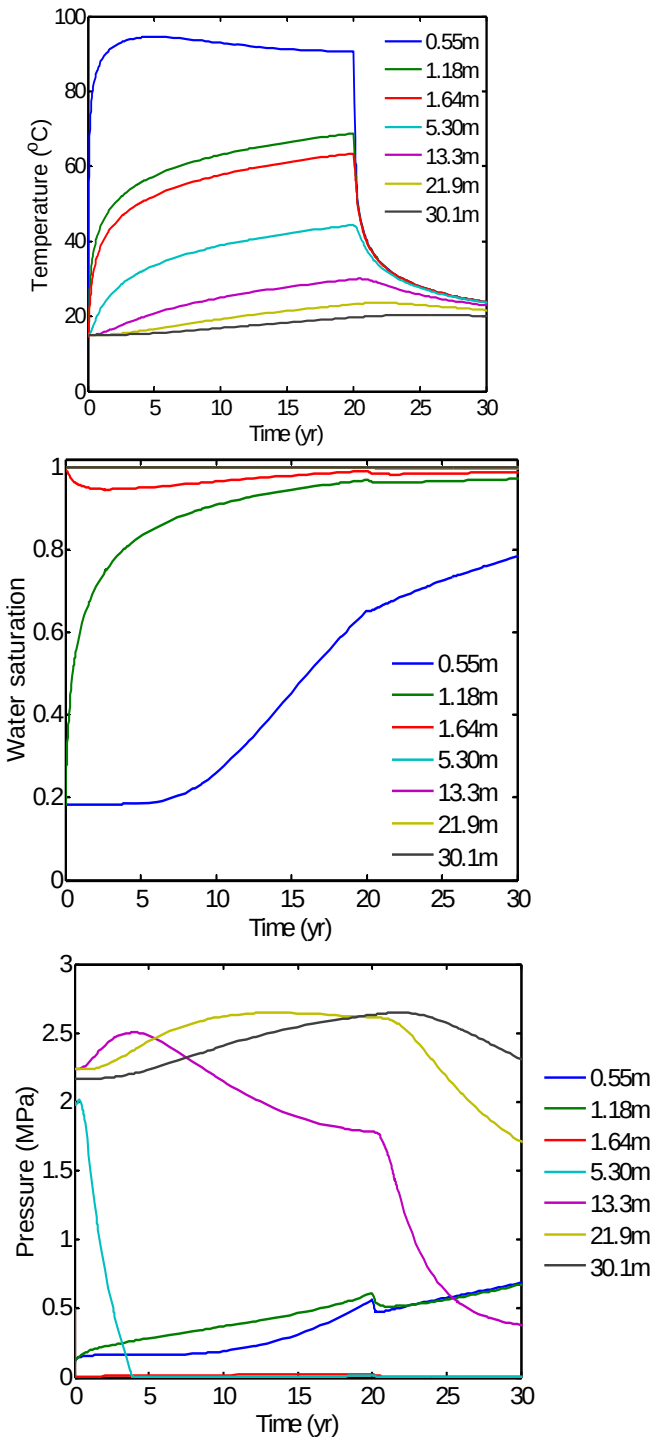

Figure 4-8. Simulated evolution of TH processes in the buffer and host rock: (a) temperature, (b) liquid saturation, (c) fluid pressure.

When the bentonite buffer is installed, liquid water is pulled from the host rock due to the strong capillary pressure at an initial saturation of 18%. The water saturation near the bentonite buffer/Opalinus rock interface (Figure 4-8 (b)) increases immediately after the installation; correspondingly, a slight desaturation is observed in the host rock. The increased water

saturation in the buffer helps to dissipate the heat from the canister and keep the temperature near the canister below 100°C, because of the increased thermal conductivity under a wetter condition. The resaturation process is quite slow because of the low permeability of the host rock and bentonite buffer. The water saturation near the canister is approximately 78% after 30 years.

Pore pressure increases gradually in the bentonite buffer. Even though the temperature increment is high, thermal expansion plays a minimal role in the pore-pressure increment, because the buffer remains unsaturated due to the slow resaturation process during the 20 years of heating. The host rock near the concrete/Opalinus interface experiences a depressurization process after the installation of the bentonite buffer. Its pressure drops by up to 3 orders of magnitude, owing to the suction by the capillary force of the bentonite buffer. Because the rock is unsaturated, the pore pressure remains low during the 20 years of heating. However, the deep host rock (>13.3 m away from canister) is pressurized due to the increase in temperature. Maximum increment of pressure is ~0.5 MPa.

4.5 Sensitivity Analysis

A sensitivity analysis was conducted, varying the parameters for capillary pressure (specifically, P_0) of the bentonite buffer and the permeabilities of the concrete liner and EDZ.

4.5.1 Capillary pressure

Three capillary pressure curves (Figure 4-8) with different air entry pressure (1.0×10^7 Pa–4.5×10^7 Pa) are tested for bentonite buffer. The simulation results are shown in Figures 4-9–4-11. With a higher capillary pressure, a lower maximum temperature is achieved in the buffer, but also a higher water saturation and a higher pore pressure; the host rock, especially those near the bentonite/Opalinus interface, tends to experience a larger desaturation. Capillary pressure has little effect on the temperature in the host rock.

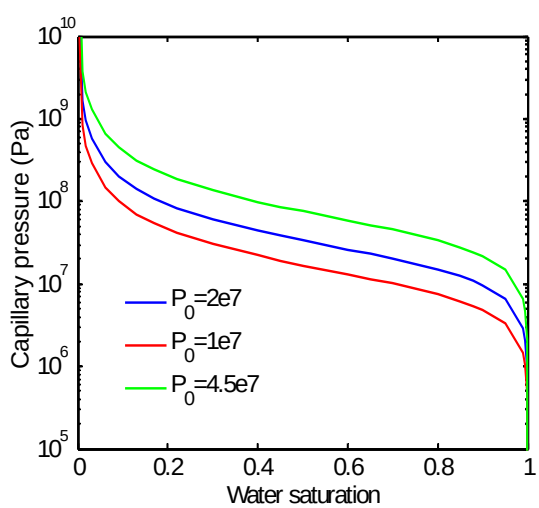

Figure 4-9. Capillary curves for bentonite in sensitivity analysis.

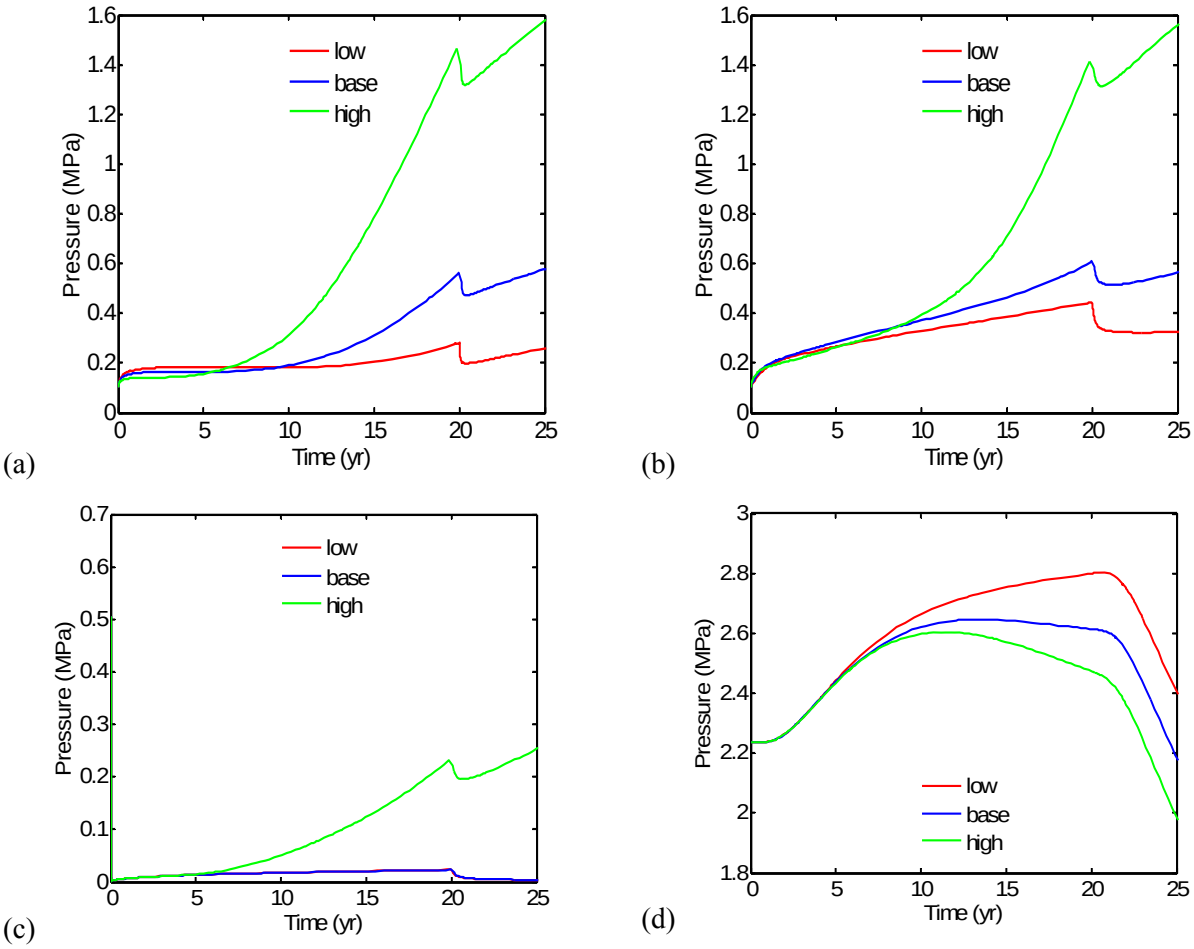

Figure 4-10. Simulated effect of capillary pressure curves on pore pressure evolution in: (a) 0.55, (b)1.18, (c)1.64, and (d) 21.9 m.

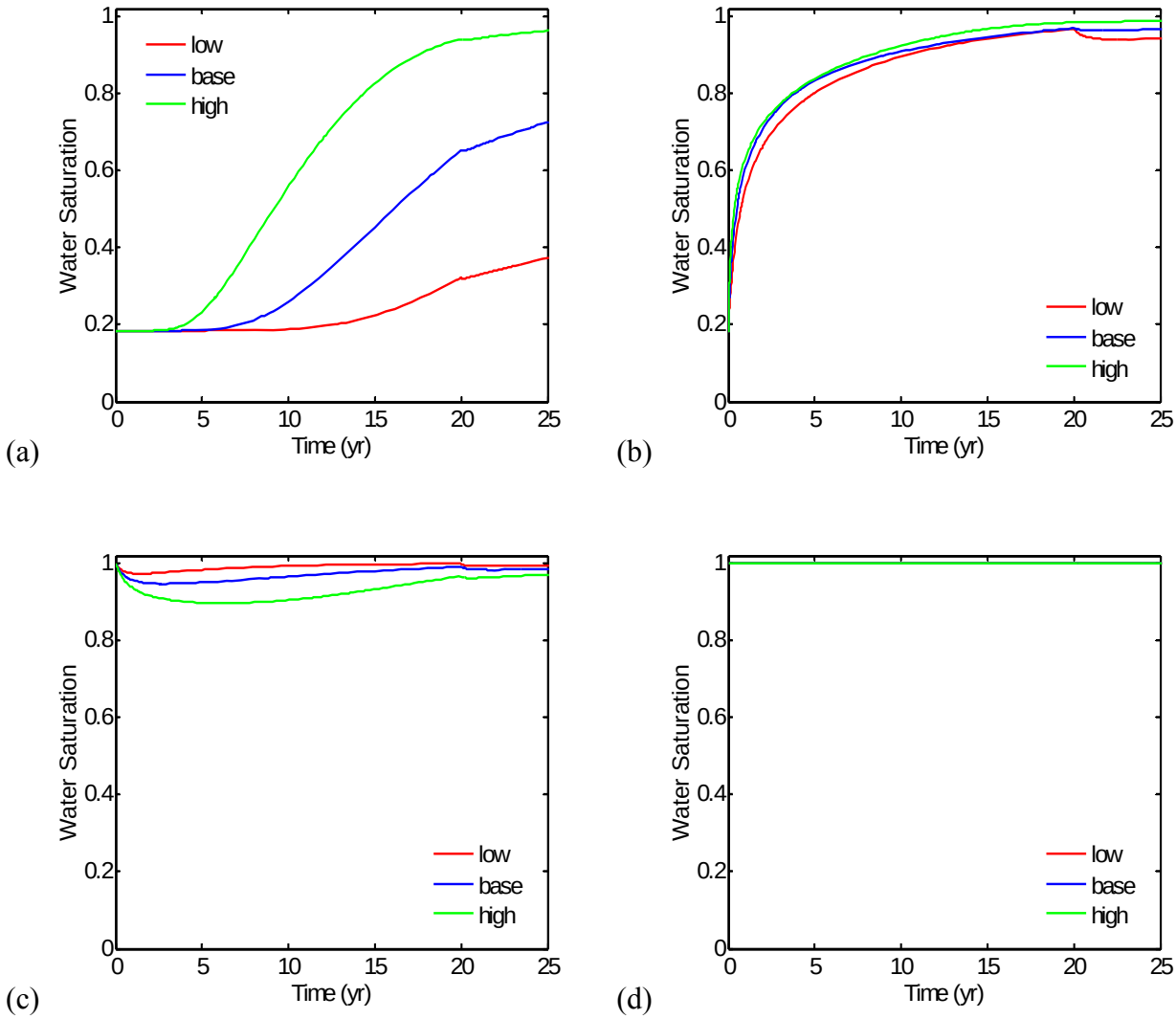

Figure 4-11. Simulated effect of capillary pressure curves on water saturation evolution in: (a) 0.55, (b)1.18, (c)1.64, and (d)21.9m.

4.5.2 Permeability of the concrete liner

The concrete liner is built between the bentonite buffer and the Opalinus clay to provide structural support for the tunnel construction. Its permeability affects the hydraulic interaction of the buffer and host rock. Permeability values from 4.5×10^{-21} m^2 to 4.5×10^{-19} m^2 were tested; the simulation results are shown in Figures 4-13–4-15. When the concrete has a lower permeability than the host rock, it acts as a barrier to hinder the water from entering the buffer. As a consequence, the temperature in the buffer tends to be higher and the water saturation tends to be lower, and the less pore pressure is increased. When the concrete permeability is higher than the host rock, its effect is minimal, due to the very limited pore volume of the liner.

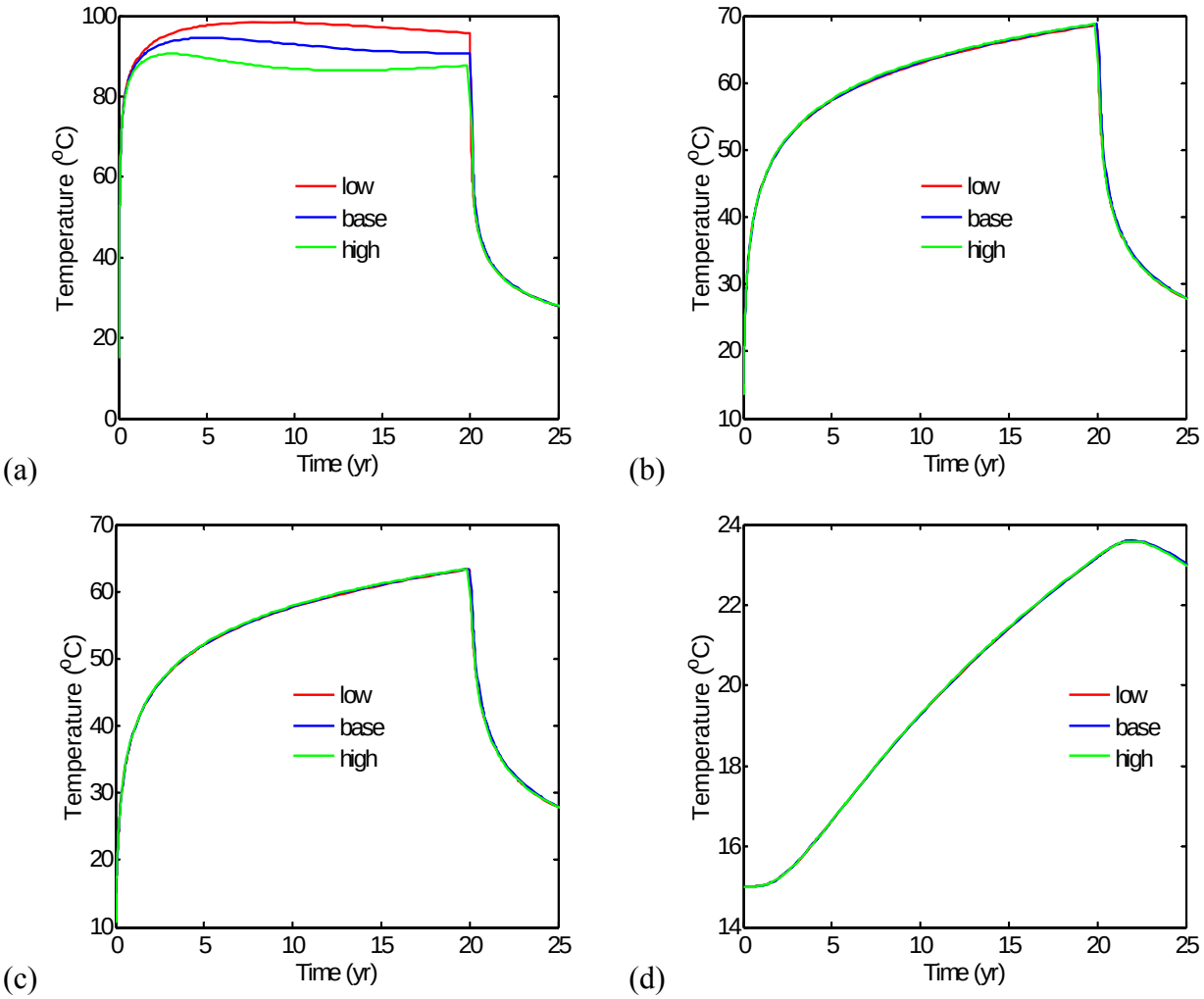

Figure 4-12. Simulated effects of capillary pressure curves on temperature evolution in: (a) 0.55, (b) 1.18, (c) 1.64, and (d) 21.9 m.

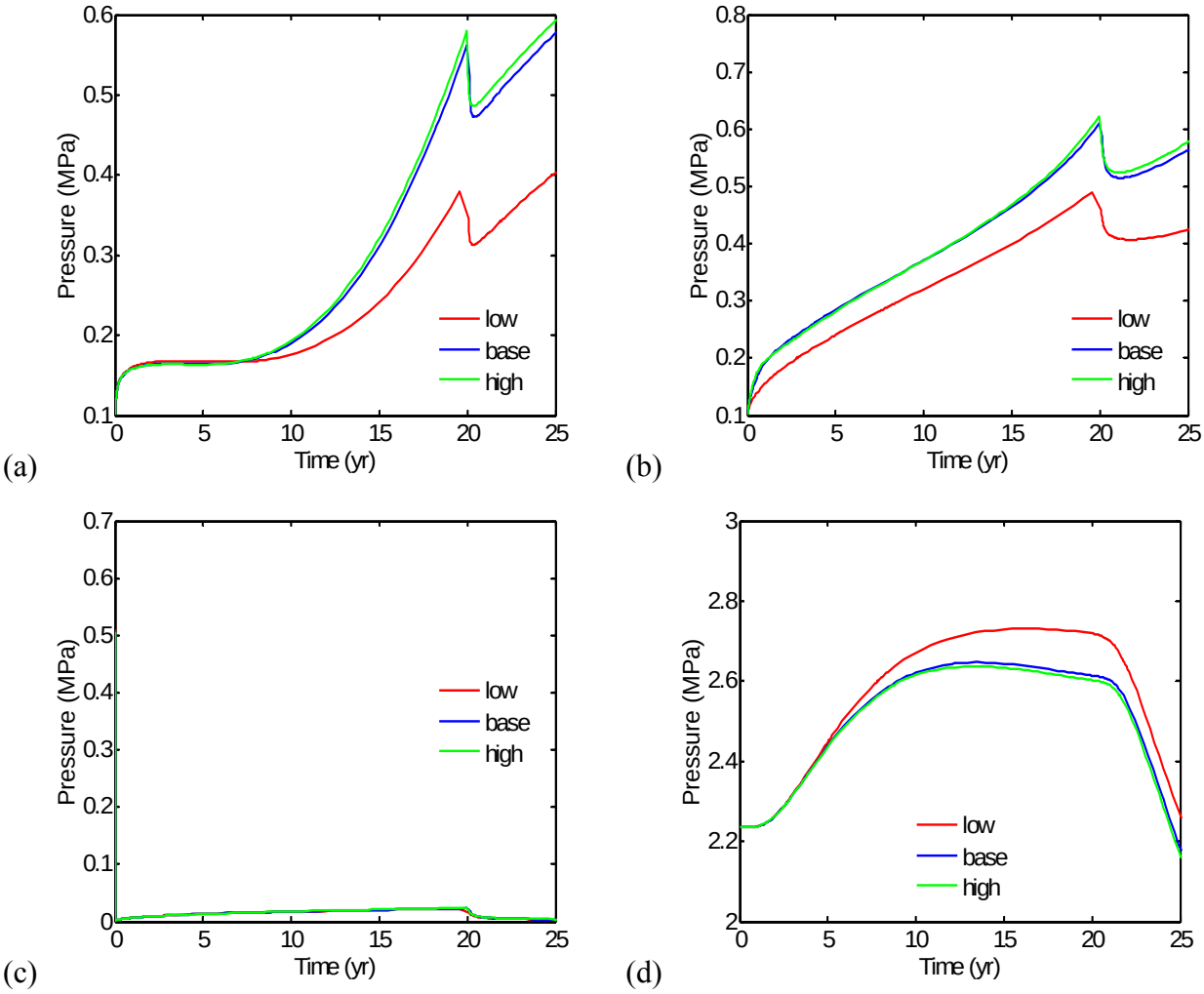

Figure 4-13. Simulated effects of concrete permeability on the pore pressure evolution in: (a) 0.55, (b) 1.18, (c) 1.64, and (d) 21.9 m.

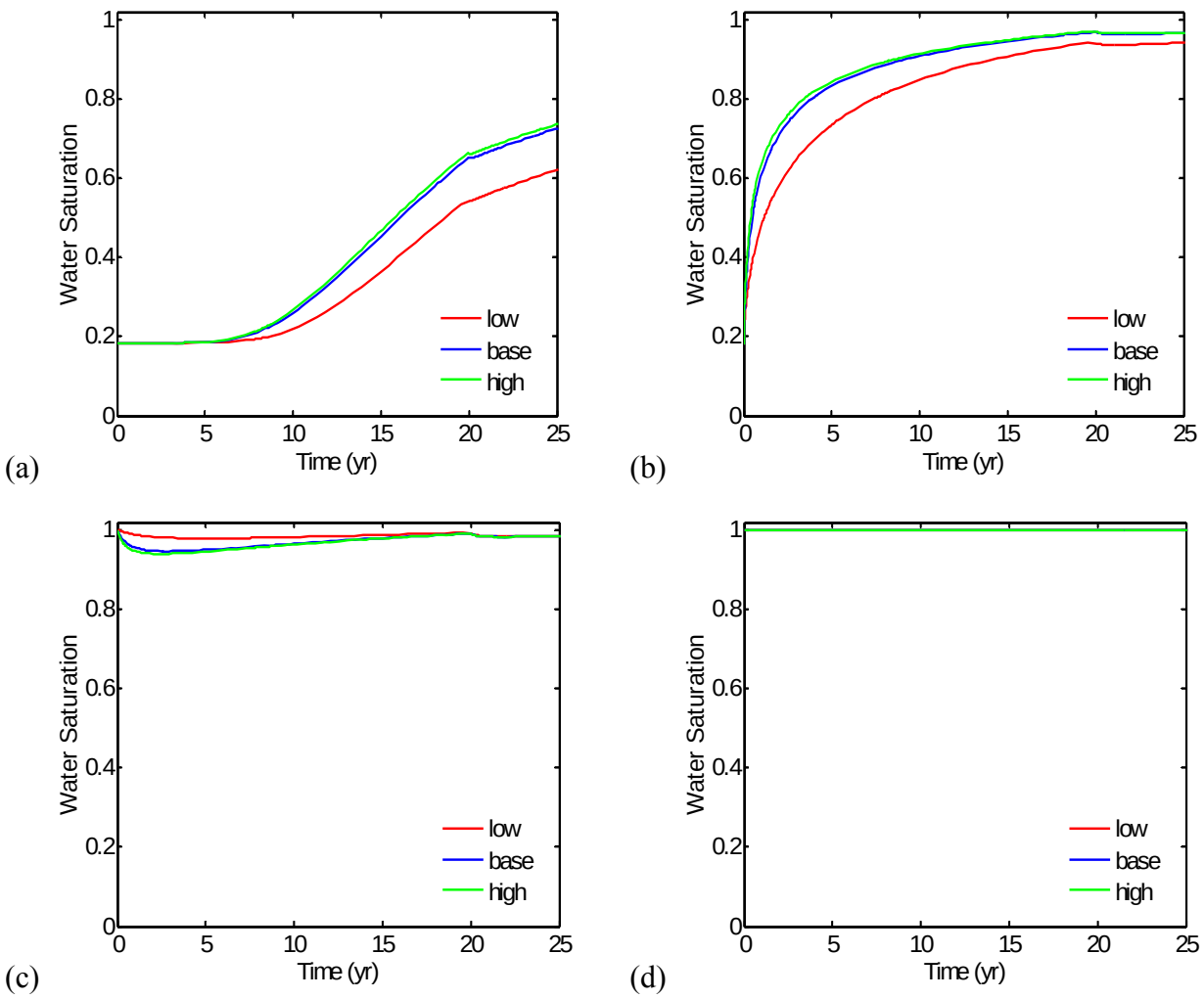

Figure 4-14. Simulated effects of concrete permeability on the water saturation evolution in: (a) 0.55, (b) 1.18, (c) 1.64, and (d) 21.9 m.

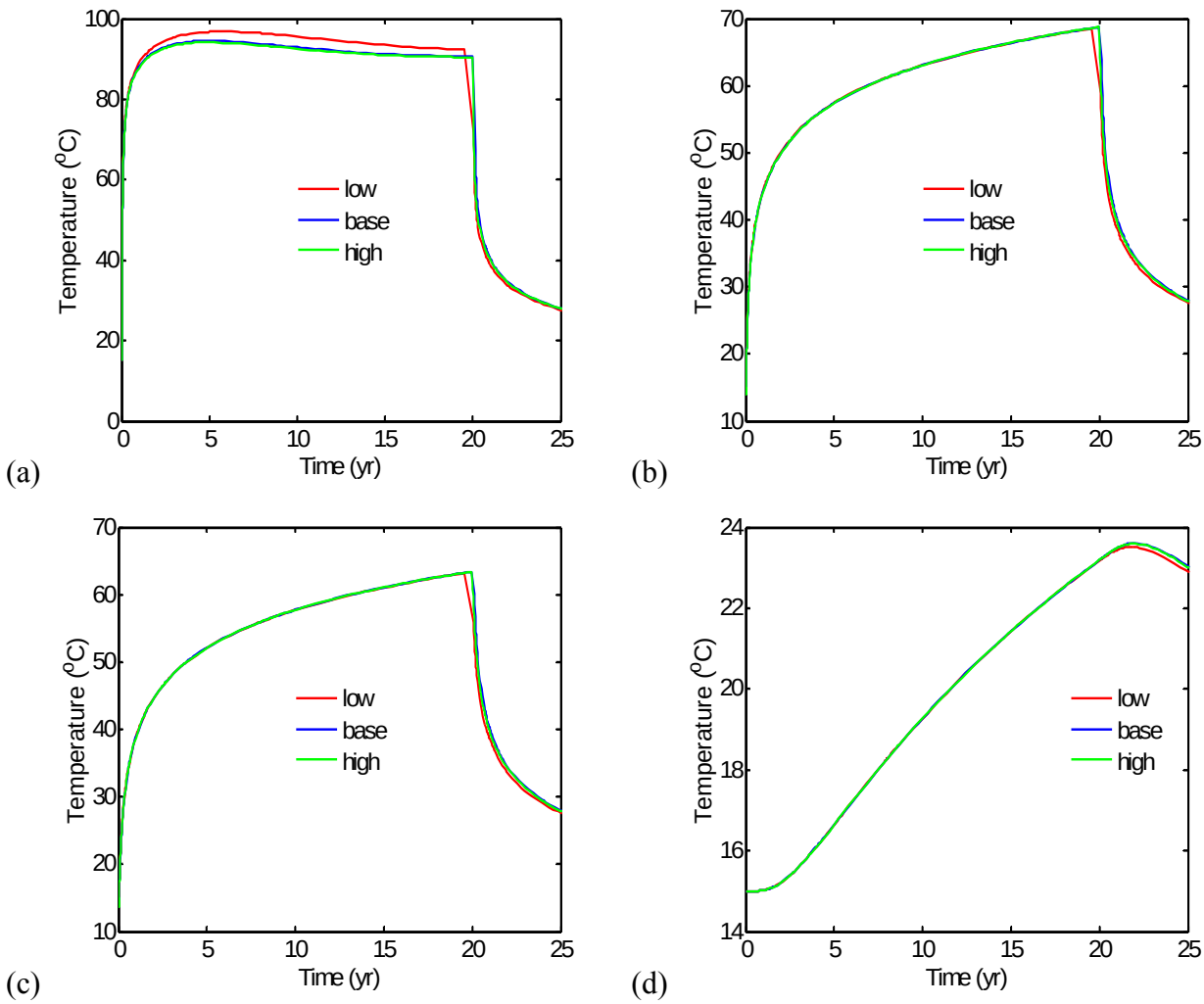

Figure 4-15. Simulated effects of concrete permeability on the temperature evolution in: (a) 0.55, (b) 1.18, (c) 1.64, and (d) 21.9 m.

4.5.3 Permeability of the EDZ

Construction of a tunnel might cause a damage zone that could have significantly higher permeability. We tested the EDZ permeability values ranging from 5×10^{-20} m^2 to 8×10^{-18} m^2. The simulation results (Figure 4-16 –Figure 4-18) show that the occurrence of EDZ has a limited effect on the evolution of temperature, pressure, and water saturation in both the buffer and host rock.

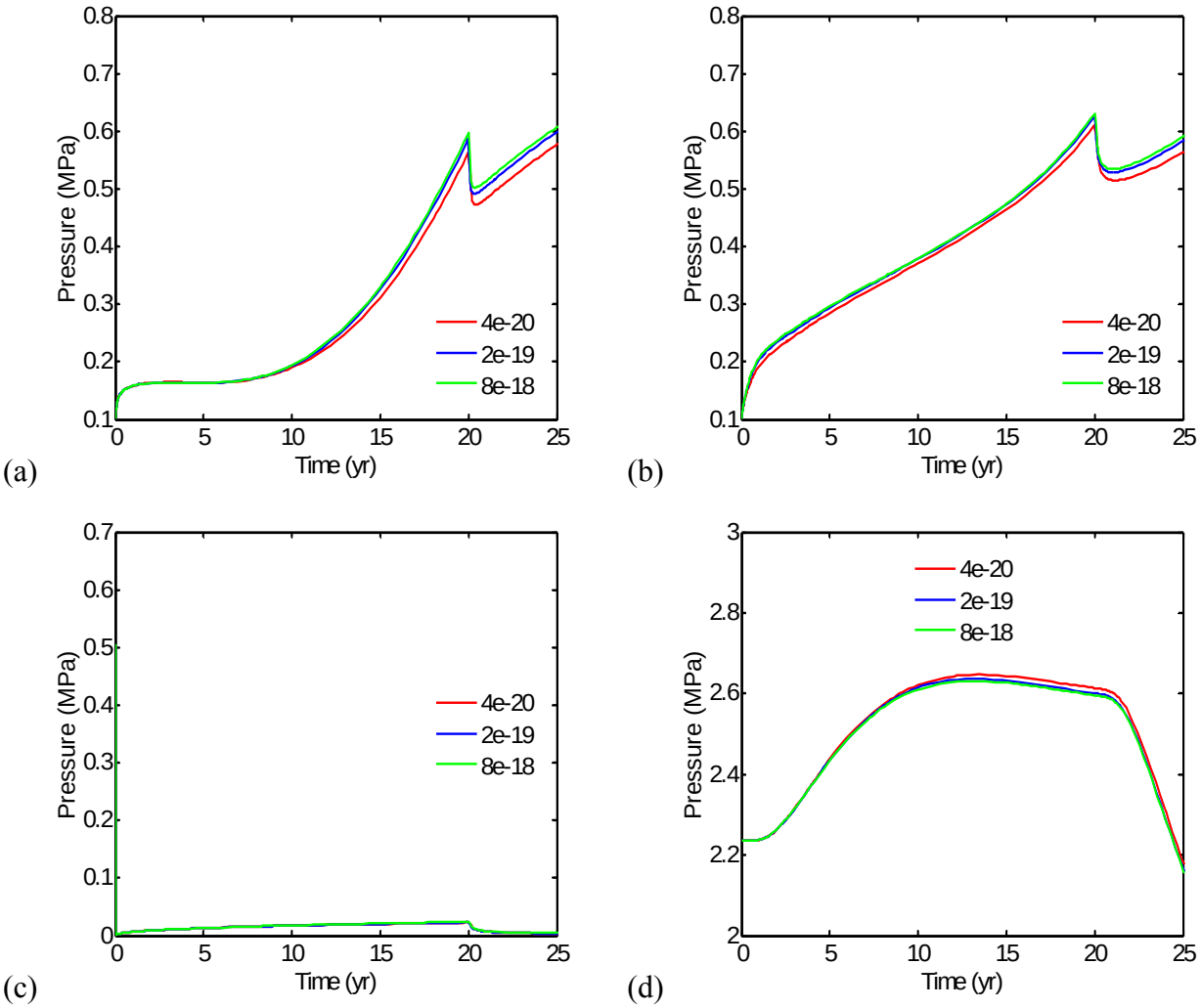

Figure 4-16. Simulated effects of EDZ on the pressure evolution in: (a) 0.55, (b) 1.18, (c) 1.64, and (d) 21.9 m.

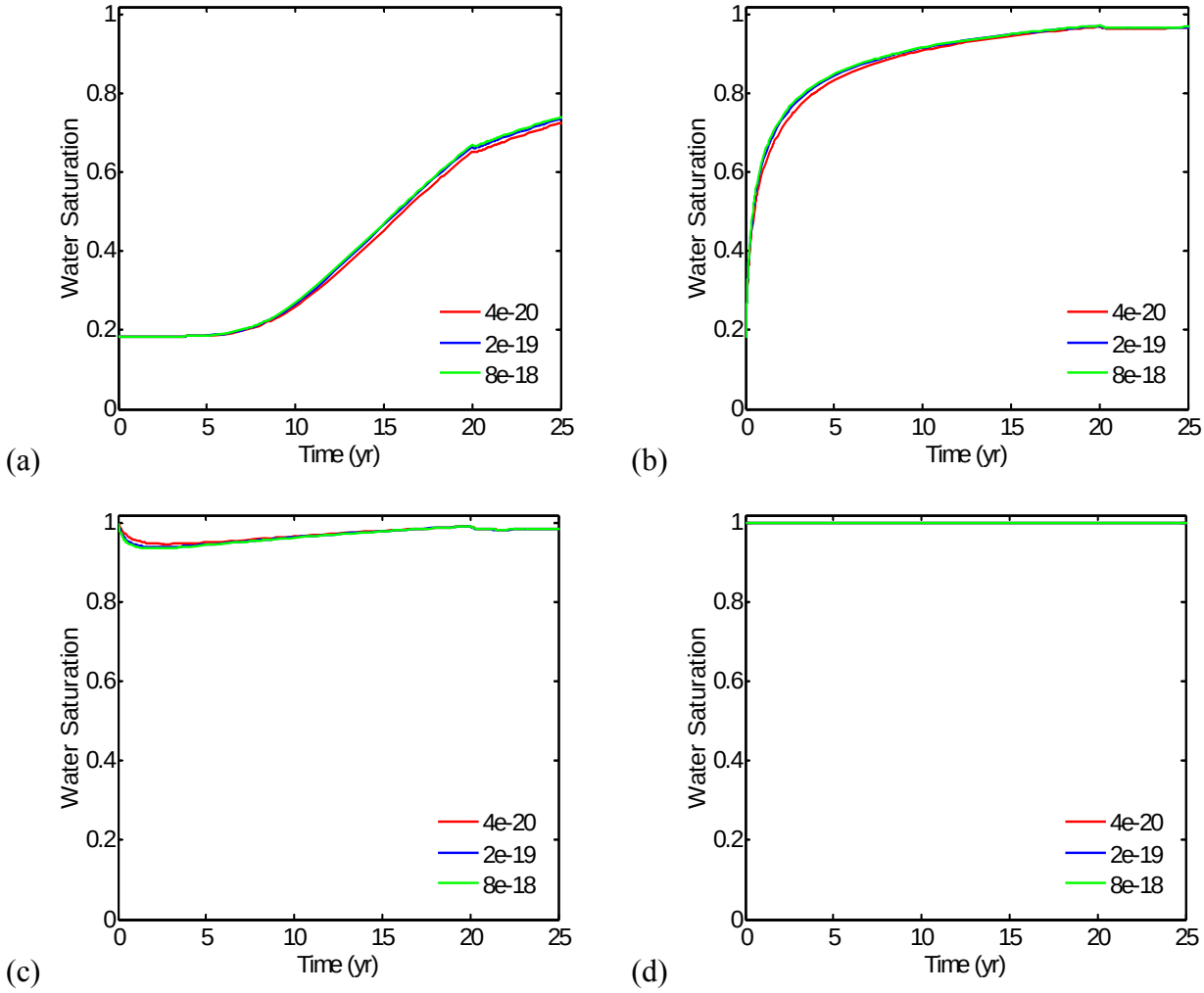

Figure 4-17. Simulated effects of EDZ on the water saturation evolution in: (a) 0.55, (b) 1.18, (c) 1.64, and (d) 21.9 m.

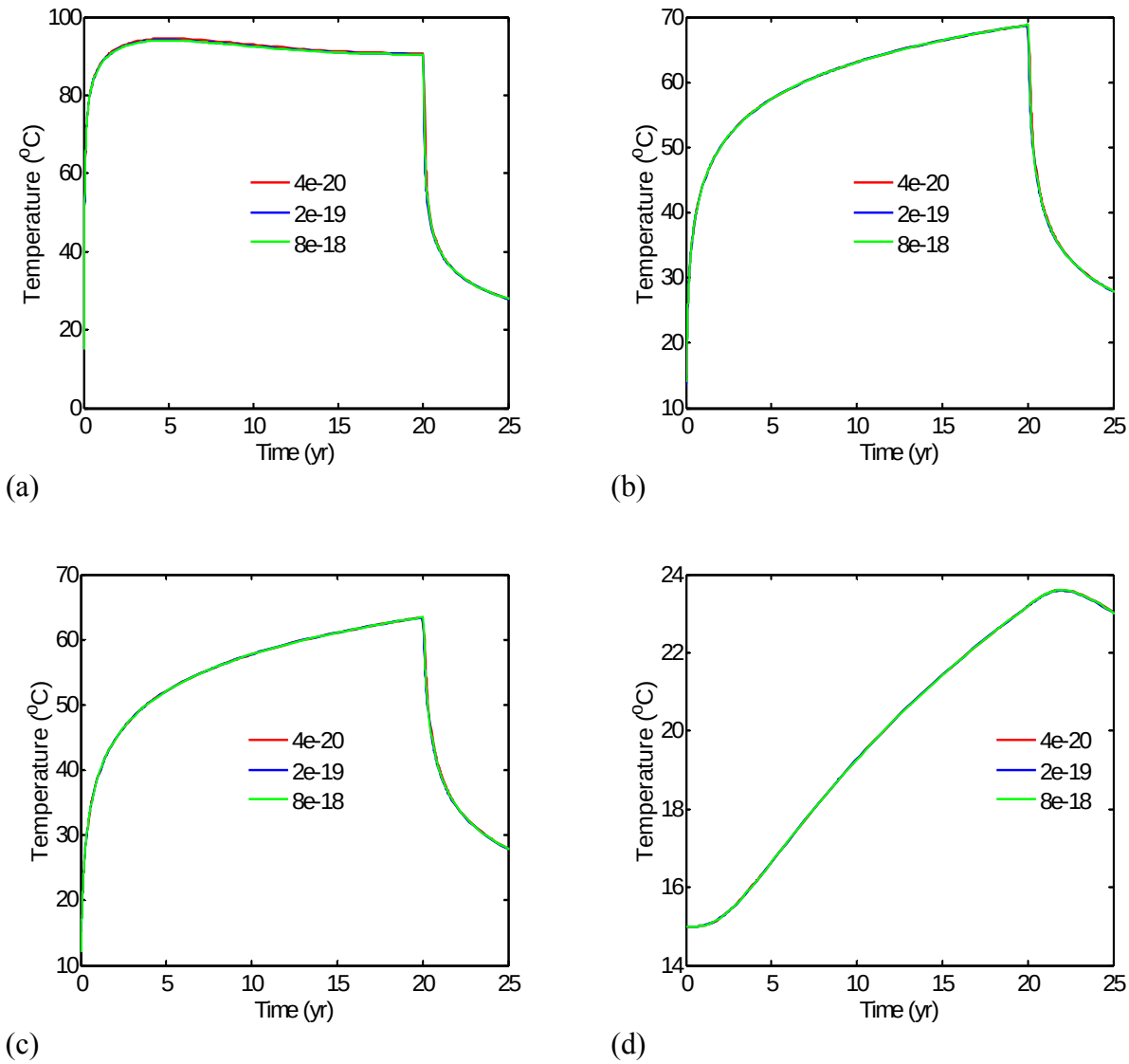

Figure 4-18. Simulated effects of EDZ on the temperature evolution in: (a) 0.55, (b) 1.18, (c) 1.64, and (d) 21.9 m.

4.6 THM Simulation

In this model inception, we used a simplified mechanical modeling of the bentonite swelling according to Rutqvist et al. (2011), adopting a linear swelling model. For the rock-mass behavior, we used a ubiquitous joint model (anisotropic plasticity with different shear strength along bedding planes) consistent with the previous ground support design analysis (Nater, 2012). The rock mechanical properties for the Opalinus clay were taken from Corkum and Martin (2007).

A significant number of measurements using different procedures (borehole slotter, undercoring, and hydraulic fracturing) of the *in situ* stress have been made at Mont Terri. A synthesis of these is given in Garitte et al. (2012):

- Major principal stress is subvertical and corresponds approximately with overburden weight (about 7MPa).
- The magnitude of the intermediate principal stress obtained from the undercoring technique is consistent with the results from hydraulic fracture tests (about 5 MPa).
- The value of the minor principal stress is quite low and probably controlled by the presence of a deep valley to the southwest of the laboratory. A low value of the minor principal stress is consistent with the small number of breakouts observed in vertical boreholes (about 2 MPa).

In our modeling, we then set the vertical stress to 7 MPa, whereas the maximum horizontal stress perpendicular to the tunnel is set to 5 MPa.

In the linear elastic swelling model, the bentonite is assumed to behave elastically, with a volumetric swelling and a swelling stress that depends on the changes in water saturation, ΔS_l, according to:

$$\Delta\sigma'_{sw} = 3K\Delta\varepsilon_{sw} = K\Delta S_l \beta_{sw}$$

where $\Delta\sigma'_{sw}$ is the induced swelling stress (an effective stress), K is the bulk modulus, and β_{sw} is a moisture swelling coefficient. In our simulation, we arbitrarily assigned a moisture swelling coefficient of 0.2, which at full saturation will lead to a swelling stress of about 10 MPa. This might be a relatively high swelling stress, and the appropriate swelling stress will in the future be determined from modeling of laboratory experiments on MX-80 bentonite pellets.

Figure 4-19 shows the stress evolution in the buffer. The compressive stress increases along with the resaturation of the buffer, which first takes place at the tunnel wall. The maximum stress at the end the heating (20 years) is about -9 MPa and is the tangential stress at the tunnel wall. After 20 years, there is a sudden drop in compressive stress, as a result of the temperature drop once the heater is turned off. The radial compressive stress increases to about -8 MPa, and this is the compressive stress that is applied on the concrete lining and supports the rock wall.

The rock-stress evolution is shown in Figure 4-20. The initial stress is quite anisotropic at the tunnel wall with a relatively high tangential stress, while the radial stress is small as a result of the free rock surface. However, the concrete lining provides some support, so the radial stress is not zero, but rather a few MPa. During the heating of the rock, and as a result of the buffer

swelling, the stress becomes more isotropic with time. At 20 years, the stress at the tunnel wall is about -9 MPa, which is very similar to the swelling stress in the buffer.

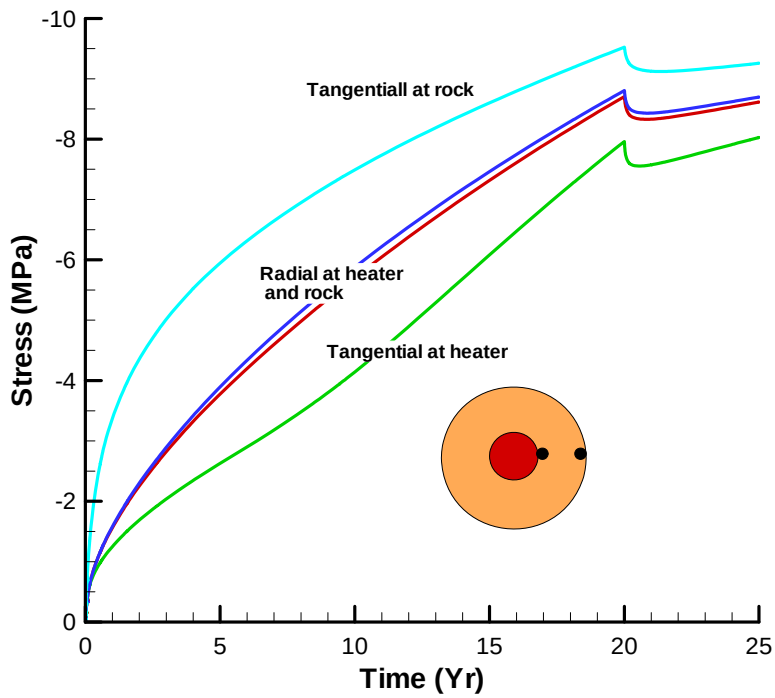

Figure 4-19. Simulated stress evolution within the bentonite buffer.

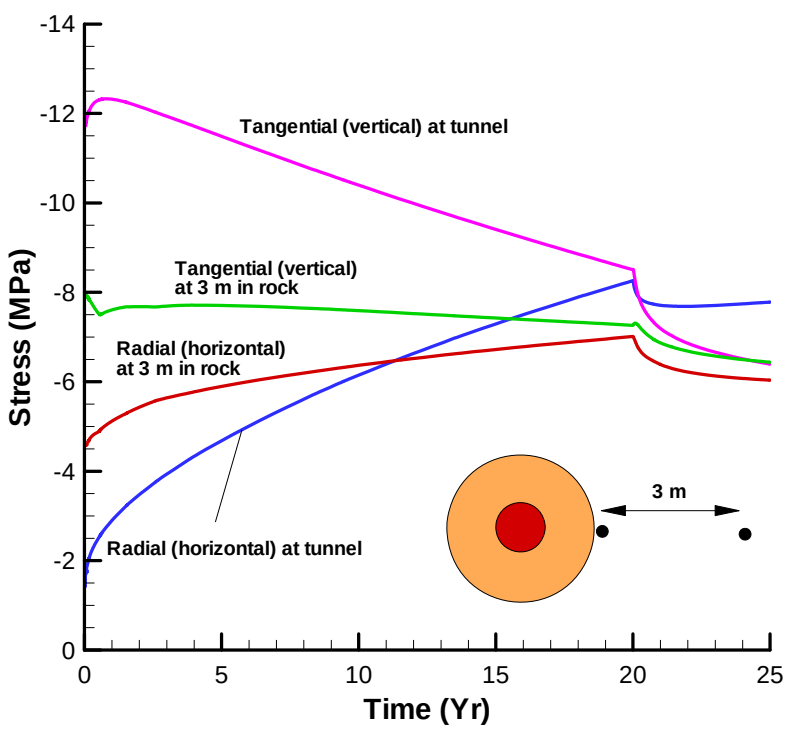

Figure 4-20. Simulated stress evolution within the Opalinus clay.

4.7 Conclusions

We conducted a preliminary TH and THM model simulation of the FE test at Mont Terri. The parameters used in the model are primarily adopted from the previous laboratory and *in situ* tests. Our TH modeling shows that the canister surface reaches the maximum temperature of 94.5°C after 4.8 years. After the installation of a bentonite buffer, water is pulled from the host rock, and the resaturation of the bentonite buffer is slow because of the low permeability of the host rock. The buffer is still unsaturated after 30 years. Pore-pressure increase due to thermal expansion is limited.

A sensitivity analysis is conducted over the capillary pressure and permeabilities of the concrete liner and EDZ. Within the investigated range in this study, we find that the temperature, water saturation, and pore pressure in the bentonite buffer are largely affected by the bentonite capillary pressure curves. Compared to the other factors (concrete liner and EDZ), it serves as the dominant role in the process.

Our THM model simulation was conducted with a simplified buffer mechanical model, whereas a ubiquitous joint model was used for modeling the anisotropic mechanical strength properties of the Opalinus clay. The analysis showed that some minor failure occurred near the tunnel wall behind the concrete lining after excavation. This failure did not expand much further during the 20-year heating cycle, meaning that the rock mass remained in an elastic mechanical state.

Overall, our model inception showed that our adopted modeling approach is adequate for modeling the coupled THM processes at the FE heater, including all components of bentonite, concrete lining, and Opalinus clay. We managed to discretize the model using the inclined mesh discretization in both TOUGH2 and FLAC3D, and the modeling results are reasonable. Our model inception indicates that the model is sufficiently large for modeling the experiment for up to about 10 years; if we take it further, toward 20 years, it would be desirable to expand the model somewhat.

Our next step will be to (1) use the BBM with current properties adopted from the FEBEX bentonite, (2) expand and test the model in 3D, (3) implement and test anisotropic thermal and hydraulic properties for Opalinus clay, (4) model laboratory experiments for detailed calibration of bentonite THM properties for MX-80 pellets.

5. Summary and Future Work

This report has addressed the following items: (1) Implementation and validation of constitutive relationships (Chapter 2); (2) Development of a DFN model for investigating coupled processes in EDZ (Chapter 3); and (3) Development of a THM model for FE tests at Mont Terri, Switzerland, for the purpose of model validation (Chapter 4). The results of these efforts are summarized here:

(1) Implementation and validation of constitutive relationships(Chapter 2)

Coupled THM processes are critical for EDZ formation and evolution in a clay repository. The constitutive relationships are the key elements for modeling these coupled processes. Considerable progress has been made during FY12 in implementing and validating the new constitutive relationships (TPHM). Specific accomplishments include:

- The TPHM and associated formulations regarding rock hydraulic/mechanical properties were implemented into TOUGH-FLAC3D code. This provides a capability to model the coupled processes with newly developed constitutive relationships.
- The usefulness and validity of the TPHM and associated formulations are demonstrated by the consistence between simulation results and field observations from the mining-by tests at Mont Terri site.
- A fine-grid numerical approach, together with an explicit incorporation of small-scale heterogeneity of mechanical properties, is able to capture the overall behavior of EDZ, as demonstrated by the consistency between simulated and observed EDZ sizes. The approach is used for investigating EDZ formation and evolution.

Future work for the remaining months of FY12 and FY13 includes:

- Development of constitutive relationships to include the impact of fracture formation on hydraulic properties within the context of continuum mechanics. The TPHM has been developed for the elastic process, but the consideration of damage impacts is preliminary and limited to fine-grid simulations in the current study. This development likely requires a dual-continuum approach to capture fracture effects.

- Further validation of the constitutive relationships with mining-by test data collected from Mont Terri site. The mining-by tests have generated rich data related to mechanical and hydraulic processes during the EDZ formation. The data set provides an important opportunity to validate THM models, including constitutive relationships. As a first step, in FY12, we developed a 2D model for the tests, but note that many important data (such as pore-pressure changes ahead of the mining face of the tunnel) have not yet been used for validation purposes, because they are highly relevant to three-dimensional processes. In FY13, we are planning to develop a three-dimensional model to further validate the

constitutive relationships, using more mining-by test data.

(2) Development of a DFN model for investigating coupled processes in EDZ (Chapter 3)

A three-dimensional computational method capable of addressing fracture initiation and propagation as a THM coupled process has been developed and tested. The hydrogeologic model follows a discrete fracture approach implemented using TOUGH2. Geomechanics and fracture damage are computed using the RBSN modeling method. Specific accomplishments include:

- A Voronoi gridding method was developed here for use both in geomechanical/fracture-damage models and in hydrogeologic flow and transport models. Voronoi grids are used to represent the rock mass (matrix) and fractures are inserted into the grid along Voronoi grid interfaces. This strategy eliminates many problems regarding incorporating new fractures into a numerical grid, minimizes computational aspects associated with regridding, and allows for a more practical incorporation of fracture initiation and propagation for THM processes.
- The discrete fracture hydrogeological model was compared with an analytical flow and transport model for cases involving a single straight fracture and rock matrix. Close agreement was found between the numerical and analytical models.
- Flow and transport in an irregular fracture based on a random Voronoi grid was also analyzed, in which the average matrix flow is parallel to the average fracture direction. The results indicate that matrix cross flow causes an enhancement in transport rates for the irregular fracture as compared with a straight fracture. Scaling rules were developed for flow and transport to account for the main effects of increased fracture path length associated with a network of irregular fractures (as compared with a network of straight fractures).
- A geomechanical and fracture-damage model was developed here using the Rigid-Body-Spring-Network (RBSN) numerical method. This model was coupled with TOUGH2 and used to compute hydrological and elastic geomechanical responses when subjected to saturation-induced hydro-mechanical strain and thermal-mechanical strain. The model results are found to be in good agreement with independent numerical and analytical solution methods for the two validation cases investigated. Fracture development and propagation were also examined with the TOUGH-RBSN model for conditions of dessication cracking. Qualitative agreement was found with results from other investigators and observations of dessication cracking in clay materials**.**

Future work for the remaining months of FY12 and FY13 includes:

- Evaluating the DFN model for more complex fracture networks in two and three dimensions.

- Extending hydromechanical coupling to include the effects of geomechanical strain on permeability and porosity.
- Investigating fracture initiation and propagation induced by excavation as well as natural processes such as fluid overpressure.
- Investigating the conditions under which fractures can self-seal, including factors that influence the rate of fracture self-sealing.

(3) Development of a THM model for FE tests at Mont Terri, Switzerland, for the purpose of model validation (Chapter 4)

Preliminary TH and THM model simulations of the FE test at Mont Terri have been performed. The parameters used in the model are primarily, adopted from previous laboratory and *in situ* tests. Specific accomplishments include:

- TH modeling shows that the canister surface reaches the maximum temperature of 94.5°C after 4.8 years. After the installation of the bentonite buffer, water is pulled from the host rock, and the resaturation of the bentonite buffer is slow because of the low permeability of the host rock. The buffer is still unsaturated after 30 years. Pore-pressure increase due to thermal expansion is limited.
- Within the investigated range in this study, we find that the temperature, water saturation, and pore pressure in the bentonite buffer are largely affected by the bentonite capillary pressure curve. Compared to the other factors (concrete liner and EDZ), it serves as the dominant role in the process.
- The THM analysis showed that some minor failure occurred near the tunnel wall behind the concrete lining after excavation. This failure did not expand much further during the 20-year heating period, meaning that the rock mass remained in an elastic mechanical state.
- The adopted modeling approach is adequate for modeling the coupled THM processes at the FE heater, including all components of bentonite, concrete lining, and Opalinus clay. The inclined mesh discretizations for both TOUGH2 and FLAC3D were found to give reasonable modeling results, and the model domain is sufficiently large for modeling the experiment for up to about 10 years. Going forward toward 20 years, it would be desirable to expand the model domain somewhat.

Future work for the remaining months of FY12 and FY13 includes:

- Use the BBM with current properties adopted from the FEBEX bentonite.
- Expand and test the model in 3D.
- Implement and test anisotropic thermal and hydraulic properties for Opalinus clay.
- Model laboratory experiments for detailed calibration of bentonite THM properties for MX-80 pellets.

Acknowledgments

Funding for this work was provided by the Used Fuel Disposition Campaign, Office of Nuclear Energy, of the U.S. Department of Energy under Contract Number DE-AC02-05CH11231 with Berkeley Lab.

6. References

Alonso E. E., Gens A., and Josa A. (1990) A constitutive model for partially saturated soils. Géotechnique, 40(3): 405-430.

Asahina, D. and Bolander, J.E. (2011) Voronoi-based discretizations for fracture analysis of particulate materials, *Powder Technology*, *213*, 92–99.

Asahina, D., Landis, E.N., and Bolander, J.E. (2011) Modeling of phase interfaces during pre-critical crack growth in concrete, *Cement & Concrete Composites*, 33, 966-977.

Barenblatt, G.I., Zheltov, Iu.P., and Kochina, I.N. (1960) Basic concepts in the theory of seepage of homogeneous liquids in fissured rocks, *J. Appl. Math. Mech*., v. 24, no. 5, 1286-1303.

Barnichon J.D. and Volckaert G. (2003) Observations and Predictions of Hydromechanical Coupling Effects in the Boom Clay, Mol Underground Research Laboratory, Belgium, *Hydrogeology Journal* 11 (1), 193-202.

Barton N.R., Bandis S.C., Bakhtar K. (1985) Strength, deformation, and conductivity coupling of rock joint deformation. Int J Rock Mech Min Sci 22, 121–40.

Bastiaens W., Bernier, F., and Li, X.L. (2007) SELFRAC: Experiments and conclusions on fracturing, self-healing and self-sealing processes in clays, *Physics and Chemistry of the Earth* 32, 600–615.

Berton, S. (2003) Numerical simulation of the durability mechanics of cement-based materials. PhD thesis, University of California, Davis.

Berton, S. and Bolander, J. (2006) Crack band model of fracture in irregular lattices," *Computational Methods in Applied Mechanics and Engineering*, 195, pp. 7172-7181, 2006.

Biot M.A. (1941) General theory of three dimensional consolidation. Journal of Applied Physics 12, 155–64.

Blair S.C., Cook N.G.W. (1998) Analysis of compressive fracture in rock statistical techniques: Part I: a non-linear rule-based model. International Journal of Rock Mechanics and Mining Sciences 35, 837–848.

Bock H., Dehandschutter B., Martin CD. (2010) Self-sealing of fractures in argillaceous formations in the context of geological disposal of radioactive waste, Review and Synthesis. Nuclear Energy Agency, ISBN 978-92-64-99095-1.

Bock H. (2001) RA experiment: rock mechanics analysis and synthesis: conceptual model of the Opalinus Clay. Technical report Nagra, Internal report TN01-03, Q+S Consult, Germany.

Bolander, J.E. and Saito, S., (1998) Fracture analyses using spring networks with random geometry. *Eng Fract Mech*, 61, 569–91.

Bolander, J.E., Li, Z., and Yip, M. (2007) Restraint and cracking during non-uniform drying of cement composites, *Proceedings of the Transport Properties and Concrete Quality Workshop - Materials Science of Concrete*, American Ceramic Society, 123-140.

Bossart P, Meier P.M, Moeri A, Trick T, Mayor J-C. (2002) Geological and hydraulic characterization of the excavation disturbed zone in the Opalinus Clay of the Mont Terri Rock Laboratory. Eng Geol 66, 19–38.

Bossart P. and Thury M. (2008) Mont Terri Rock Laboratory – Project, Programme 1996 to 2007 and Results. Swiss Geological Survey, Wabern.

Bossart, P., Trick, T., Meier, P.M., and Mayor, J.-C. (2004) Structural and hydrogeological characterisation of the excavation-disturbed zone in the Opalinus Clay (Mont Terri Project, Switzerland), *Applied Clay Science*, 26, 429– 448.

Brady B.T. (1969) The nonlinear mechanical behavior of brittle rock Part I—Stress–strain behavior during regions I and II. Int J Rock Mech Min Sci 6, 211–225

Brown, E.T., Bray, J.W. and Santarelli, F.J. (1989) Influence of stress-dependent elastic moduli on stresses and strains around axisymmetric boreholes. Rock Mechanics and Rock Engineering 22, 189–203.

Cazacu O. (1999) On the choice of stress-dependent elastic moduli for transversely isotropic solids. Mech Res Commun 26, 45–54

Chiaramonte, L., Zoback, M.D., Friedmann, J., and Stamp, V. (2008) Seal integrity and feasibility of CO2 sequestration in the Teapot Dome EOR pilot: geomechanical site characterization, *Environ Geol*, 54:1667–1675.

Chen Y.F., Zhou C.B., Sheng Y.Q. (2007) Formulation of strain-dependent hydraulic conductivity for a fractured rock mass. Int. J. Rock Mech. Min. Sci. 44, 981–996

Chinaia B., Vervuurt A., Van Mier J.G.M. (1997) Lattice model evaluation of progress failure in disordered particle composites. Engineering Fracture Mechanics 57 (2/3), 301–318.

Colina, H. and Roux, S. (2000) Experimental model of cracking induced by drying shrinkage *Eur. Phys. J. E* 1, 189-194.

Corkum A.G., Martin CD. (2007a) Modeling a mine-by test at the Mont Terri rock laboratory, Switzerland. International Journal of Rock Mechanics & Mining Sciences 44, 846–859.

Corkum A.G., Martin CD. (2007b) The mechanical behaviour of weak mudstone (Opalinus Clay) at low stresses. International Journal of Rock Mechanics & Mining Sciences 44, 196–209.

Cosgrove, J.W. (2001) Hydraulic Fracturing during the Formation and Deformation of a Basin: A Factor in the Dewatering of Low-Permeability Sediments, *AAPG Bulletin*, v. 85, no. 4, pp. 737–748.

Duguid, J.O., and Lee, P.C.Y. (1977) Flow in Fractured Porous Media, *Water Resources Research*, v. 13, no. 3.

Ewing J. and Senger R. (2011) Evolution of Temperature, Pressure, and Saturation in the Bentonite Buffer: Scoping Calculations in Support of the Design of the Full-Scale Emplacement Experiment at the Mont Terri URL. NAGRA NAB 10-38, September 2011.

Fairhurst C. (1964) On the validity of the Brazilian test for brittle materials. Int. J. Rock Mech. Min. Sci. 1: 535–546.

Fang Z., Harrison J.P. (2002) Development of a local degradation approach to the modelling of brittle fracture in heterogeneous rocks. International Journal of Rock Mechanics & Mining Sciences 39, 443–457.

Fierz T. (1999) ED-B Experiment: deformation measurements during Phase 4. Inclinometer and sliding micrometer measurements in BED-B6, BED-B7 and BED-B8. Technical Report Nagra, Internal Report TN99-25, Solexperts, AG.

Fouche O., Wright H., Cleach J. L., and Pellenard P. (2004) Fabric Control on Strain and Rupture of Heterogeneous Shale Samples by Using a Non-Conventional Mechanical Test, *Applied Clay Science* 26, 367-387.

Garitte B. and Gens A. (2012) TH and THM Scoping computations for the definition of an optimal instrumentation layout in the Full-scale Emplacement (FE) experiment NAGRA NIB 10-34, March 2012.

Garitte B., Bond A., Millard A., Zhang C., English M., Nakama A., and Gens A. (2012) Analysis of hydro-mechanical processes in a ventilated tunnel in an argillaceous rock on the basis of different modelling approaches. *Journal of Rock Mechanics and Geotechnical Engineering* (submitted May 2012).

Germanovich L.N., Dyskin A.V. (2000) Fracture mechanisms and instability of opening in compression. International Journal of Rock Mechanics and Mining Science 37, 263–284.

Gonçalvès, J., Violette, S., and Wendling, J. (2004) Analytical and Numerical Solutions for Alternative Overpressuring Processes: Application to the Callovo-Oxfordian Sedimentary Sequence in the Paris Basin, France, *Journal of Geophysical Research*, v. 109, 14 pp.

Gonzales S. and Johnson K. S. (1984) *Shale and other argillaceous strata in the United States*. Oak Ridge National Laboratory. ORNL/Sub/84-64794/1.

Goodman R.E. (1976) Methods of geological engineering in discontinuous rocks. NewYork: West Publishing.

Hazzard J.F., Young R.P. (2000) Micromechanical modelling of cracking and failure in brittle rocks. Journal of Geophysical Research 105 (B7), 16683–16697.

Hajiabdolmajid, V., Kaiser, P.K., Martin, C.D. (2002) Modelling brittle failure of rock. International Journal of Rock Mechanics and Mining Sciences 39, 731–741.

Houseworth, J.E. (2006) An analytical model for solute transport in unsaturated flow through a single fracture and porous rock matrix. *Water Resources Research*, 42.

Itasca Consulting Group. (2005) FLAC3D: Fast Lagrangian Analysis of Continua in 3Dimensions. Itasca Consulting Group, Minneapolis ‹http://www.itascacg.com/flac3d/index.php›.

ITASCA, 2009. FLAC3D V4.0, Fast Lagrangian Analysis of Continua in 3 Dimensions, User's Guide. Itasca Consulting Group, Minneapolis, Minnesota.

Jaeger J.C., Cook N.G.W., Zimmerman R.W. (2007) Fundamentals of rock mechanics. 4th ed. Oxford: Blackwell.

Jobmann M., Wilsnack Th., Voigt H.D. (2010) Investigation of damage-induced permeability of Opalinus clay. International Journal of Rock Mechanics & Mining Sciences 47, 279–285.

Johnson P.A., Rasolofosaon P.N.J. (1996) Nonlinear elasticity and stress-induced anisotropy in rock. J Geophys Res 101, 3113–3124

Kawai, T. (1978) New Discrete Models and their Application to Seismic Response Analysis of Structures, *Nuclear Engineering and Design* 48, 207-229.

Kruschwitz S, Yaramanci U. (2004) Detection and characterization of the disturbed rock zone in claystone with the complex resistivity method. J Appl Geophys 57(1), 63–79.

Li, L., Tang, C., Wang, S. (2012) A coupled thermo-hydrologic-mechanical damage model and associated application in a stability analysis on a rock pillar. *Tunneling and Underground Space Technology*, in review.

Lichtner, P. (2000) Critique of Dual Continuum Formulations of Multicomponent Reactive Transport in Fractured Porous Media, Dynamics of Fluids in Fractured Rock, Geophysical Monograph 122, American Geophysical Union.

Lionco A., Assis A. (2000) Behaviour of Deep Shafts in Rock Considering Nonlinear Elastic Models. Tunneling and Underground Space Technology 15(4), 445-451.

Liu H.H., Rutqvist J., Berryman J.C. (2009) On the relationship between stress and elastic strain for porous and fractured rock. International Journal of Rock Mechanics & Mining Sciences 46, 289–296.

Liu, H.Y., Roquete, M., Kou, S.Q., Lindqvist, P.A. (2004) Characterization of rock heterogeneity and numerical verification. Eng. Geol. 72, 89-119.

Louis C. (1974) Rock hydraulics. In: Muller L (ed) Rock mechanics. Springer, Vienna.

Maloszewski, P., and Zuber, A. (1985) On the theory of tracer experiments in fissured rocks with a porous matrix, *J. Hydrol*., 79, 333– 358.

Martin C.D. Lanyon G.W. (2004) Excavation Disturbed Zone (EDZ) in Clay Shale: Mont Terri, TECHNICAL REPORT 2001-01(Mont Terri TR 2001-01).

Ma G.W., Wang X.J., Ren F. (2011) Numerical simulation of compressive failure of heterogeneous rock-like materials using SPH method. International Journal of Rock Mechanics & Mining Sciences 48, 353–363.

Mavko G.M., Nur A. (1978) The effect of nonelliptical cracks on the compressibility of rocks. J Geophys Res 83, 4459–4468.

Mayer G., Klubertanz G., Croise J. (2007) Modeling of an in situ ventilation experiment in the Opalinus Clay. Physics and Chemistry of the Earth 32, 629–638.

Mayor J.C., Velasco M., García-Siñeriz J.L. (2007) Ventilation experiment in the Mont Terri underground laboratory. Physics and Chemistry of the Earth 32, 616–628.

Mazurek, M., Pearson, F.J., Volckaert, G., and Bock, H. (2003) Features, Events and Processes Evaluation Catalogue for Argillaceous Media. ISBN 92-64-02148-5. Nuclear Energy Agency.

McClintock, F.A., Argon, A.S. (1966) Mechanical Behavior of Materials. Addison-Wesley, Reading, MA, p.770.

Meier P., Trick T., Blumling P., and Volckaert G. (2000) Self-Healing of Fractures within the EDZ at the Mont Terri Rock Laboratory: Results after One Year of Experimental Work. In: *Proceedings of the International Workshop on Geomechanics, hydromechanical and Thermomechanical Behavior of deep argillaceous Rocks: Theory and Experiments*, Paris, October11-12, 2000.

Moinfar, A., Narr, W., Hui, M.-H., Mallison, B. and Lee, S.H. (2011) Comparison of Discrete-Fracture and Dual-Permeability Models for Multiphase Flow in Naturally Fractured Reservoirs, 142295-MS, SPE Reservoir Simulation Symposium, 21-23 February 2011, The Woodlands, Texas, USA.

Nater P. (2012) Mont Terri / FE-Experiment Geomechanische Modellierung des Vortriebs. NAGRA AN 12-184.

National Research Council, Committee on Fracture Characterization and Fluid Flow (1996) Rock Fractures and Fluid Flow: Contemporary Understanding and Applications, National Research Council, National Academies Press.

Nawrocki P.A., Dusseault M.B., Bratli R.K. and Xu G. (1998) Assessment of some semi-analytical models for non-linear modelling of borehole stresses. International Journal of Rock Mechanics and Mining Sciences & Geomechanic Abstract 35, Paper No. 34.

Neretnieks, I. (1980) Diffusion in the rock matrix: An important factor in radionuclide retardation, *J. Geophys. Res.*, 85(B8), 4379– 4397.

Neuzil, C.E. (2003) Hydromechanical coupling in geologic processes, *Hydrogeology Journal*, 11:41–83.

Nur, A. (1971) Effects of stress on velocity anisotropy in rocks with cracks. Journal of Geophysical Research 76, 2022–2034.

Nutt M. (2011) *Used Fuel Disposition Campaign Disposal Research and Development Roadmap* (FCR&D-USED-2011-000065 REV0), U.S. DOE Used Fuel Disposition Campaign.

Olalla C, Martin M, Saez J. (1999) ED-B experiment: geotechnical laboratory test on Opalinus Clay rock samples. Technical report TN98-57, Mont Terri Project.

Oldenburg, C.M. and Pruess, K. (1995) EOS7R: Radionuclide Transport for TOUGH2, Lawrence Berkeley National Laboratory, LBL-34868.

Otto Schulze, Till Popp, Hartmut Kern. (2001) Development of damage and permeability in deforming rock salt. Eng. Geol. 61, 163–180.

Patriarche D., Ledoux E., Simon-Coincon R., Michelot J., and Cabrera J. (2004) Characterization and Modeling of Diffusive Process for Mass Transport through the Tournemire Argillites Aveyron, France, *Applied Clay Science* 26: 109-122, 2004.

Pearce C.J., Thavalingam A., Liao Z., Bicanic N. (2000) Computational aspects of the discontinuous deformation analysis framework for modeling concrete fracture. Eng Fract Mech 65, 283–298.

Pietruszczak S, Xu G. (1995) Brittle response of concrete as a localization problem. Int. J. Solid. Struct. 32, 1517–1533.

Popp T., Salzer K., Minkley W. (2008) Influence of bedding planes to EDZ-evolution and the coupled HM properties of Opalinus Clay. Physics and Chemistry of the Earth 33, 374–387.

Potyondy D.O., Cundall P.A., Lee C.A. (1996) Modelling rock using bonded assemblies of circular particles. In: Proceedings of the 1996 2nd North American Rock Mechanics Symposium, NARMS'96, pp. 19–37.

Poulos H.G., Davis E.H. (1974) Elastic solutions for soil and rock mechanics. John Wiley and Sons, New York.

Pruess K., Oldenburg C., Moridis G. (1999) TOUGH2 USER'S GUIDE, VERSION 2.0, Earth Sciences Division, Lawrence Berkeley National Laboratory, University of California, Berkeley, California.

Pruess K., Oldenburg C. M., Moridis G. (2011) TOUGH2 User's Guide, Version 2.1, LBNL-43134(revised), Lawrence Berkeley National Laboratory, Berkeley, California.

Reichenberger, V., Jakobs, H., Bastian, P., Helmig, R. (2006) A mixed-dimensional finite volume method for two-phase flow in fractured porous media, Advances in Water Resources 29 (2006) 1020–1036.

Rutqvist, J., Ijiri, Y., and Yamamoto, H. (2011) Implementation of the Barcelona Basic Model into TOUGH–FLAC for simulations of the geomechanical behavior of unsaturated soils, *Computers & Geosciences* 37, 751–762.

Rutqvist, J., Wu, Y.-S., Tsang, C.-F., and Bodvarsson, G. (2002) A modeling approach for analysis of coupled multiphase fluid flow, heat transfer, and deformation in fractured porous rock, *Int. J. of Rock Mechanics & Mining Sciences*, 39, 429–442.

Rutqvist J., Zheng L., Chen F.,, Liu H.-H. and Jens Birkholzer J. Modeling of Coupled Geomechanical and Geochemical Processes Associated with Bentonite-Backfilled Repository Tunnels in Clay Formations. (Submitted, April 2012).

Schuster K., Alheid H.J., Boddener D. (2001) Seismic investigation of the excavation damaged zone in Opalinus Clay. Eng Geol 61, 189–197.

Shao J.F., Zhou H., Chau K. T. (2005) Coupling between anisotropic damage and permeability variation in brittle rocks. Int. J. Numer. Anal. Meth. Geomech. 29, 1231–1247.

Shao H., Schuster K., Sönnke J., Bräuer V. (2008) EDZ development in indurated clay formations – In situ borehole measurements and coupled HM modeling. Physics and Chemistry of the Earth 33, 388–395.

Sheldon H.A. (2009) Simulation of magmatic and metamorphic fluid production coupled with deformation, fluid flow and heat transport. Computers & Geosciences 35, 2275–2281.

Sloan, S. W. (1987) A fast algorithm for constructing Delaunay triangulations in the plan. Advances in Engineering Software 9(1), 34-55.

Stormont J.C., Daemen J.J.K. (1992) Laboratory study of gas permeability changes in rock salt during deformation. Int J Rock Mech Min Sci & Geomech Abstr. 29, 325–42.

Stormont J.C. (1997) In situ gas permeability measurements to delineate damage in rock salt. Int J Rock Mech Min Sci 34(7), 1055–64.

Sudicky, E.A. and Frind, E. O. (1982) Contaminant transport in fractured porous media: Analytical solutions for a system of parallel fractures, *Water Resour. Res.*, 18(6), 1634–1642.

Susan E, Minkoff C, Mike Stone & Steve Bryant. (2003) Coupled fluid flow and geomechanical deformation modeling. J Pet. Sci. Eng. 38, 37–56.

Tang C.A., Hudson J.A. (2010) Rock Failure Mechanisms: Illustrated and Explained. United Kingdom, CRC PRESS-Taylor & Francis Ltd, ISBN: 0415498511.

Tang C.A., Liu H., Lee P.K.K., Tsui Y, Tham L.G. (2000) Numerical studies of the influence of microstructure on rock failure in uniaxial compression—Part I: effect of heterogeneity. Int J Rock Mech Min Sci 37, 555–569

Tang C.A., Tham L.G., Lee P.K.K., Yang T.H., Li L.C. (2002) Coupled analysis of flow, stress and damage (FSD) in rock failure. Int. J. Rock Mech. Min. Sci. 39(4), 477–89.

Tang, D.H., Frind, E.O. and Sudicky, E.A. (1981), Contaminant transport in fractured porous media: Analytical solution for a single fracture, *Water Resour. Res.*, 17(3), 555– 564.

Taniguchi, T., Yamashita, Y., and Moriwaki, K. (2002) Generation of arbitrary 3-dimensional domain from nodes on its surface. 8th Conference on Numerical Grid Generation, Hawaii, U.S.A.

Thomure, J. L., Bolander, J. E., and Kunieda, M. (2001) Reducing mesh bias on fracture within rigid-body-spring networks. *Journal of Structural Mechanics and Earthquake Engineering*, 18, 2, 95-103.

Tsang C.-F., Bernier F., and Davies C. (2005) Geohydromechanical processes in the Excavation Damaged Zone in crystalline rock, rock salt, and indurated and plastic clays—in the context of radioactive waste disposal. *International Journal of Rock Mechanics & Mining Sciences*, 42, 109-125.

Tsang, C.F., Birkholzer, J., Liu, H.H. (2010) "A Review of Key Processes and Outstanding Issues Related to Radioactive Waste Repositories in Clay Formations", DOE Used Fuel Disposition Campaign, Lawrence Berkeley National Laboratory.

Tsang C-F, Jing L, Stephansson O, Kautskz F. (2005) The DECOVALEX III project: a summary of activities and lessons learned. Int J Rock Mech Min Sci 42, 593–610.

Tsang C.F. Barnichon J.D., Birkholzer J., Li X.L., Liu H.H., Sillen X. (2012) Coupled thermo-hydro-mechanical processes in the near field of a high-level radioactive waste repository in clay formations. International Journal of Rock Mechanics & Mining Sciences 49, 31–44.

van Genuchten, M.T., (1980). A closed-form equation for predicting the hydraulic conductivity of unsaturated soils. *Soil Science Society of America Journal*, 44, 892-898.

Vermeer P.A., and deBorst R. (1984) Non-Associated Plasticity for Soils, Concrete and Rock. Heron, 29(3), 3–64.

Vietor T. (2011) Mine-by test in Mont Terri rock laboratory-MB Experiment. Report- MB Experiment: Data base for the predictive model. Nagra, Switzerland.

Vietor T. (2012).Mont Terri Project - FE Experiment Modelling Kick-off Meeting. February 9, 2012, Mont Terri, Switzerland. NAGRA Technical Discussion TD-217.

Walsh, J.B. (1965) The effect of cracks on the compressibility of rock. Journal of Geophysical Research 70, 381–9.

Wang Y. (2011) Research & Development (R&D) *Plan for Used Fuel Disposition Campaign (UFDC) Natural System Evaluation and Tool Development*, U.S. DOE Used Fuel Disposition Campaign.

Weibull W. (1951) A statistical distribution function of wide applicability. Journal of Applied Mechanics 18, 293–297.

Weng M.C., Jeng F.S., Hsieh Y.M., Huang T.H. (2008) A simple model for stress-induced anisotropic softening of weak sandstones. International Journal of Rock Mechanics & Mining Sciences 45, 155–166.

Wong TF, Wong RHC, Chau KT, Tang CA (2006) Microcrack statistics, Weibull distribution and micromechanical modeling of compressive failure in rock. Mech Mater 38, 664–681.

Yang Y.L., Aplin A.C. (2010) A permeability-porosity relationship for mudstones. Marine and Petroleum Geology 27, 1692–1697.

Yip, M., Mohle, J., and Bolander, J. (2005) Automated modeling of three-dimensional structural components using irregular lattices, *Computer-Aided Civil and Infrastructure Engineering*, v. 20, pp. 393-407.

Yuan S.C., Harrison J.P. (2005) Development of a hydro-mechanical local degradation approach and its application to modelling fluid flow during progressive fracturing of heterogeneous rocks, Int. J. Rock Mech. Min. Sci. 42, 961-984.

Zhang C.L., Rothfuchs T., Dittrich J., Muller J. (2008) Investigations on self-sealing of indurated clay. –GRS Report, GRS-230: 1-67, ISBN 978-3-939355-04-5.

Zhu W.C., Liu J., Tang C.A., Zhao X.D., Brady B.H. (2005) Simulation of progressive fracturing processes around underground excavations under biaxial compression. Tunnelling and Underground Space Technology 20, 231–247.

Zhu WC, Tang CA (2004) Micromechanical model for simulating the fracture process of rock. Rock Mech. Rock Eng. 37, 25–56.

Zhu WL, Wong TF. (1997) The transition from brittle faulting to cataclastic flow: permeability evolution. J Geophys Res 102(B2), 3027–3041.

Zhao Y, Liu H.H. (2012) An elastic strain-stress relationship for porous rock under anisotropic stress conditions. Rock Mechanics & Rock Engineering 45(3), 389–399.